

Generalized dynamical mean-field theory in the physics of strongly correlated systems

E Z Kuchinskii, I A Nekrasov, M V Sadovskii

DOI: 10.3367/UFNe.0182.201204a.0345

Contents

1. Introduction	325
2. Strongly correlated systems and dynamical mean-field theory (DMFT)	326
2.1 The Hubbard model and the basics of DMFT; 2.2 Generalized DMFT + Σ approach; 2.3 Some other generalizations of DMFT	
3. Application of generalized DMFT + Σ approach to model problems	330
3.1 Strongly correlated systems in the pseudogap state; 3.2 Mott–Anderson transition in disordered systems; 3.3 Singularities of electron dispersion in strongly correlated systems in DMFT and DMFT + Σ approaches	
4. Electronic structure of real strongly correlated systems: LDA + DMFT and LDA + DMFT + Σ	345
4.1 Density functional theory (DFT). Local density approximation (LDA); 4.2 LDA + DMFT computational scheme; 4.3 Examples of LDA + DMFT calculations; 4.4 Electronic structure of copper oxides in the pseudogap state: LDA + DMFT + Σ	
5. Conclusions	353
References	353

Abstract. This review discusses the generalization of dynamical mean-field theory (DMFT) for strongly correlated electronic systems to include additional interactions necessary for the correct description of physical effects in such systems. Specifically, the additional interactions include: (1) the interaction of electrons with antiferromagnetic (or charge) order-parameter fluctuations in high-temperature superconductors leading to the formation of a pseudogap state; (2) scattering on static disorder and its role in the general picture of the Anderson–Hubbard metal–insulator transition, and (3) electron–phonon interaction and the features of electronic spectra in strongly correlated systems. The proposed DMFT + Σ approach incorporates the above interactions by introducing into the general DMFT model an additional (generally momentum-dependent) self-energy Σ which is calculated in a self-consistent way without violating the general structure of the DMFT iteration cycle. The paper formulates a general calculational scheme for both one-parti-

cle (spectral functions and densities of states) and two-particle (optical conductivity) properties. The problem of pseudogap formation is examined, including Fermi arc formation and partial destruction of the Fermi surface, as are the metal–insulator transition in the disordered Anderson–Hubbard model, and the general picture of kink formation in the electronic spectra of strongly correlated systems. A generalization of the DMFT + Σ approach to realistic materials with strong electron–electron correlations is presented based on the LDA + DMFT method. The general model of the LDA + DMFT method is reviewed, as are some of its applications to real systems. The generalized LDA + DMFT + Σ approach is employed to calculate pseudogap states in electron- and hole-doped HTSC cuprates. Comparisons with angle-resolved photoemission spectroscopy (ARPES) results are presented.

1. Introduction

Strongly correlated electronic systems (SCSs), which are mainly realized in a number of compounds of transition or rare-earth elements with partially filled 3d, 4f, and 5f shells, have for more than half a century been attracting great interest of scientists because of their unusual physical properties and difficulties in their theoretical description. The question of metal–insulator phase transition observed in many transition metal oxides, heavy fermions systems with a great variety of different phase transitions and related phenomena, manganites with giant magnetoresistance — all these systems have become the focus for both experimentalists and theorists. Perhaps the most significant development in this area was the discovery of high-temperature superconductivity in copper oxides, which provoked a new wave of interest in the synthesis and description of such systems.

E Z Kuchinskii, I A Nekrasov Institute for Electrophysics, Ural Branch of the Russian Academy of Sciences, ul. Amundsena 106, 620016 Ekaterinburg, Russian Federation
E-mail: kuchinsk@iep.uran.ru, nekrasov@iep.uran.ru
M V Sadovskii Institute for Electrophysics, Ural Branch of the Russian Academy of Sciences, ul. Amundsena 106, 620016 Ekaterinburg, Russian Federation
E-mail: sadovski@iep.uran.ru
Institute for Metal Physics, Ural Branch of the Russian Academy of Sciences, ul. S Kovalevskoi 18, 620219 Ekaterinburg, Russian Federation

Received 20 June 2011

Uspekhi Fizicheskikh Nauk **182** (4) 345–378 (2012)

DOI: 10.3367/UFNr.0182.201204a.0345

Translated by M V Sadovskii and I A Nekrasov; edited by A Radzig

As already stressed above, the diversity of physical phenomena in all these compounds is due to partially filled 3d, 4f, and 5f electron shells. The strong interaction of electrons emerged from narrow bands belonging to these orbitals with each other or with itinerant electrons of outer shells is basically responsible for the unique properties of these systems. The early qualitative ideas formulated by Mott [1] have been further developed in many theoretical studies to follow, forming a new area of the modern theory of condensed matter. There are now thousands of such papers and many new reviews and monographs are regularly published [2].

Of course, nowadays, a single review cannot cover all this area of research and the aim of the authors is rather modest. The subject of this work concerns a description of a number of theoretical approaches formulated during recent years to account for some additional interactions which are important for the consistent description of strongly correlated systems. Here, we are speaking not only about ‘external’ perturbations due to the interaction of correlated electrons with bosonic excitations, such as phonons, spin fluctuations, or scattering of electrons by disorder, but also about attempts to improve the most developed and widely used theoretical approaches, such as dynamical mean-field theory (DMFT) [3–6].

These tasks are closely related to a variety of topical problems under active study at present, such as the nature of the pseudogap state of high- T_c cuprates, the evolution of their Fermi surfaces upon doping, with the formation of so-called ‘Fermi arcs’ observed in ARPES experiments, the problem of the formation of kinks in the electronic spectrum, and the general problem of metal–insulator transition in disordered systems due to the mutual interference of strong correlations and Anderson localization. In this review, we deal to some extent with all of these problems.

During recent years, the general theory of strongly correlated systems based on DMFT has practically merged with the so-called *ab initio* approaches to calculating electronic spectra of real solids (LDA + DMFT approach), with a significant success already achieved [2, 7]. To this end, we devote some attention in our review to the first attempts to generalize these approaches in an effort of accounting for the above-mentioned physical effects.

2. Strongly correlated systems and dynamical mean-field theory (DMFT)

2.1 The Hubbard model and the basics of DMFT

Starting with the pioneering works of Hubbard [8–13] in the early 1960s, the simplest model permitting the description of strongly correlated systems is the so-called Hubbard model. The one-band Hubbard model Hamiltonian is written down as

$$H = -t \sum_{\langle ij \rangle \sigma} c_{i\sigma}^\dagger c_{j\sigma} + U \sum_i n_{i\uparrow} n_{i\downarrow}, \quad (1)$$

where $t > 0$ is the nearest neighbors hopping amplitude, U is the single-site repulsion, $n_{i\sigma} = c_{i\sigma}^\dagger c_{i\sigma}$ is the particle number operator at the site, and $c_{i\sigma}$ ($c_{i\sigma}^\dagger$) is the annihilation (creation) electron operator for spin σ . The model has only two competing energy parameters: parameter t defines the kinetic energy of an electron and facilitates intersite hoppings (delocalization), while parameter U defines potential energy

and favors electron localization at a lattice site. Energy bands formed by 3d, 4f, and 5f orbitals are rather narrow; thus, quite often kinetic and potential energy are of the same order of magnitude ($t \sim U$). In this case, there is no small parameter in the model and it is impossible to build any kind of perturbation theory. This fact alone leads to all the difficulties in describing SCSs, even for such an oversimplified model.

Almost for 30 years there were no satisfactory approaches to analyzing SCSs. It seemed that the theory of these systems would forever remain fragmentary and semiquantitative. The breakthrough came in 1989 in the work by Metzner and Vollhardt [14], who suggested formal consideration of the system of interacting electrons in the space of large dimension $d \rightarrow \infty$ (or in a lattice with large coordination number $z \rightarrow \infty$).¹

Employing this limit, it is possible to neglect spatial fluctuations in the systems, while the full local dynamics are preserved. In Ref. [14], it was shown that in the limit of infinite spatial dimensions (or more precisely of infinite coordination number) the main role is played only by local contributions to the self-energy part of the full interacting Green function. All nonlocal contributions are proportional to $1/\sqrt{z} \sim 1/\sqrt{d}$ and can be dropped. In this limit, therefore, electron self-energy does not depend on momentum \mathbf{k} , and is a function of frequency only [real (ω) or Matsubara (ω_n , $n = 0, \pm 1, \dots$)]:²

$$\Sigma_\sigma(\mathbf{k}, \omega) = \Sigma_\sigma(\omega). \quad (2)$$

This statement represents the main simplification appearing in the limit of $d \rightarrow \infty$ [3, 5–7].

In Fig. 1, we show the ‘skeleton’ diagrams of DMFT self-energy Σ . Wavy lines indicate local (Hubbard) Coulomb interaction U , whereas full lines fit local Green functions G_{ii} . Strictly speaking, not only is the self-energy local in the limit of $d \rightarrow \infty$, but also in each vertex of the ‘skeleton’ diagram only one particular site enters, e.g. the i -th one, as shown in Fig. 1. Thus, this self-energy is a functional of interacting local Green function $G_{ii, \sigma}$: $\Sigma_{ii, \sigma} = F[G_{ii, \sigma}]$. Generally, it is not yet sufficient for our problem to become fully local, since interacting Green function $G_{ij, \sigma}$ is still nonlocal. A question then arises of whether it is possible to choose a purely local noninteracting ($U = 0$) problem (even with complex dynamics) yielding completely equivalent self-energy. Surely, it can be done! Let $\mathcal{G}_\sigma(\omega)$ be the ‘bare’ dynamical Green function of such a local problem without Coulomb interaction U , while $G_{d\sigma}(\omega)$ and $\Sigma_{d\sigma}(\omega)$ are corresponding interacting Green function and self-energy. If one can ensure

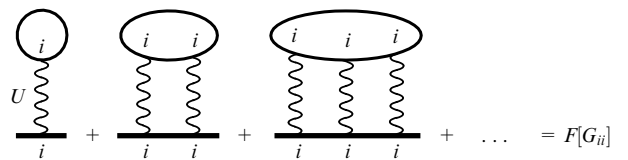


Figure 1. ‘Skeleton’ diagrams of local self-energy Σ in DMFT.

¹ For a hypercubic lattice $z = 2d$, and these two limits practically coincide. However, z could be quite large even for three-dimensional lattices, for example, in a body-centered lattice with $z = 8$, and for a face-centered lattice with $z = 12$. To this end, it is more correct to speak about the limit of large z .

² Large coordination numbers allow one to apply this approximation rather successfully even for rather small d .

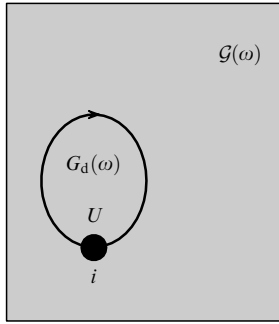


Figure 2. Within the DMFT, the Hubbard lattice model maps onto interacting electrons at a single site (‘impurity’) surrounded by the fermionic bath, which defines, in turn, dynamical (Weiss) mean field $\mathcal{G}(\omega)$.

the equality $G_{d\sigma}(\omega) = G_{ii,\sigma}(\omega)$, then corresponding self-energies are also equivalent, because the structure of diagrams for the weak-coupling (low U) perturbation theory is totally preserved, which means that the self-energy of the local problem is defined by the same functional $\Sigma_{d\sigma} = F[G_{d\sigma}]$. But \mathcal{G}_σ , $G_{d\sigma}$, and $\Sigma_{d\sigma}$ are connected through the Dyson equation which immediately gives us the bare dynamical Green function of the local problem:

$$\mathcal{G}_\sigma^{-1}(\omega) = \Sigma_\sigma(\omega) + G_{ii,\sigma}^{-1}(\omega). \quad (3)$$

Thus, the lattice Hubbard model in the limit of $d \rightarrow \infty$ exactly maps onto the purely local dynamical problem. Physically, it corresponds (as shown in Fig. 2) to the problem of interacting electrons on a single ‘Anderson impurity’ in a ‘bath’, and interaction with the bath is contained in dynamical mean-field $\mathcal{G}(\omega)$. Quite often, in analogy with the internal magnetic field of molecular field theory in magnetism, this field is called the ‘Weiss field’. This explains the name of such an approach — dynamical mean-field theory

Such a purely dynamical problem is still quite complicated. However, the problem is equivalent to a single-impurity Anderson model (SIAM) [15]. The latter model can be studied in detail by a number of different methods, and its physical nature is now well understood. For this model there are well-developed approximate analytical methods such as the iterative perturbation theory (IPT) [5] and noncrossing approximation (NCA) [16, 17], but most remarkable is the possibility of solving this model by exact numerical methods like quantum Monte Carlo (QMC) [18–22] or numerical renormalization group (NRG) [23, 24]. The solution to an effective SIAM employing any of these methods, usually called an ‘impurity solver’ (IS), completes the general outline of the DMFT approach.

Apparently, today DMFT is the most elaborate and reliable theoretical method for describing SCSs. In its framework, the so-called three-peak structure of the density of states (DOS) in SCSs was obtained for the first time [5], consisting of the narrow central (quasiparticle) peak on the Fermi level, and two wide maxima corresponding to upper and lower Hubbard bands. Also, the reliable theoretical description of Mott–Hubbard metal–insulator transition was obtained. In Fig. 3, we display DMFT (NRG) densities of states for the half-filled Hubbard model with a semielliptic bare density of states with bandwidth $2D$. As correlation strength U grows, the density of states demonstrates the

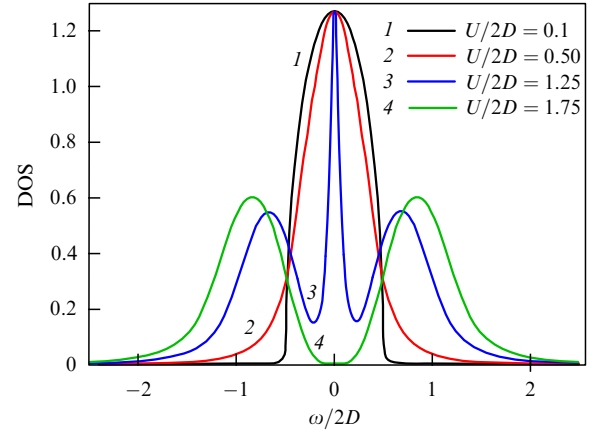


Figure 3. DMFT (NRG) densities of states at half-filling obtained for a semielliptic ‘bare’ density of states for different values of U .

formation of a characteristic three-peak structure, and a further increase in U leads to a collapse of the quasiparticle peak at $U/2D \approx 1.5$, leading to metal–insulator transition.

It turned out that within DMFT it is also possible to investigate some two-particle properties. In particular, it is quite easy to obtain dynamic optical conductivity [4, 5]. During recent years, the DMFT approach has been generalized to describe realistic SCSs by merging it with *ab initio* one-electron density functional theory in a local density approximation (DFT/LDA), leading to the combined computational LDA + DMFT scheme [25–31], which will be described later.

Despite all the obvious advantages of LDA + DMFT, this approach has a number of shortcomings. Namely, as we stressed above, all nonlocal correlations are completely neglected. A number of cluster generalizations of DMFT [32, 33] were proposed recently to overcome this drawback. However, all these methods require significant computing resources and are rather restricted in cluster size and with respect to their generalization to the multiorbital case. Also, in these approaches it is quite difficult to investigate two-particle properties. To overcome these difficulties, we have proposed recently [35–37] a new generalization of the conventional DMFT, allowing the consideration of nonlocal correlations or additional (with respect to the Hubbard) interactions (in principle, of any kind), remaining within a single-impurity DMFT picture and preserving a self-consistent set of DMFT equations.

2.2 Generalized DMFT + Σ approach

The main idea of the new approach consists in using the DMFT solution exact in the limit of $d \rightarrow \infty$ as a ‘high-energy’ zeroth order approximation describing electronic spectra on a sufficiently large energy scale on the order of the bandwidth or U value, while low-energy scale details caused by nonlocal effects or by effects of interaction of correlated electrons with different collective modes (e.g. phonons or spin fluctuations) are to be taken into account within some kind of perturbation theory, conserving, as far as possible, the general structure of DMFT equations. Actually, such a scenario can be realized in a rather simple way [35–37].

To be more specific, we shall consider in the following the standard one-band Hubbard model. Its generalizations for the multiorbital or multiband case are also possible. The main assumption of our approach is that the Matsubara lattice

one-particle Green function is chosen as

$$G_{\mathbf{k}}(i\omega) = \frac{1}{i\omega + \mu - \varepsilon(\mathbf{k}) - \Sigma(i\omega) - \Sigma_{\mathbf{k}}(i\omega)}, \quad (4)$$

$$\omega = \pi T(2n + 1),$$

where μ is the chemical potential, $\Sigma(i\omega)$ is the *local* DMFT type self-energy due to Hubbard interaction, $\Sigma_{\mathbf{k}}(i\omega)$ is some ‘external’ (generally nonlocal, momentum-dependent) self-energy, T is the temperature, and $n = 0, \pm 1, \dots$. This last contribution can arise from the interaction of correlated electrons with some ‘additional’ collective modes or order parameter fluctuations appearing in the Hubbard model itself, or from any other interactions (fluctuations) external with respect to the standard Hubbard model. For example, these can be phonons or scattering by impurities, when it is actually local (momentum-independent).

It should be emphasized that $\Sigma_{\mathbf{k}}(i\omega)$ can contain a local (momentum-independent) contribution, even if the self-energy is considered in the framework of the Hubbard model itself. However, this contribution *disappears* in the limit of infinite spatial dimensions $d \rightarrow \infty$ and is not accounted for within the conventional DMFT, so that within our approach we do not encounter any double counting problem, even in this case. This question does not arise at all for self-energy $\Sigma_{\mathbf{k}}(i\omega)$ caused by external interactions.

More important is that our assumption about the additive form of self-energy $\Sigma(i\omega) + \Sigma_{\mathbf{k}}(i\omega)$ implicitly corresponds to the neglect of interference between the local (DMFT) and nonlocal contributions. In Fig. 4, typical skeleton diagrams for the self-energy of the DMFT + Σ approach are given. The first two terms (1, 2) are local DMFT self-energy diagrams; the two diagrams (3, 4) in the middle stand for contributions to the nonlocal part of self-energy from additional interactions with collective modes or order parameter fluctuations, and the last diagram (5) is an example with the interference between the local and nonlocal parts neglected. Indeed, once we neglect such interference (i.e., diagram 5), the total self-energy is defined as a simple sum of these two contributions (1–4) shown in Fig. 4. Two diagrams (3, 4) in Fig. 4 provide an example of skeleton diagrams for nonlocal self-energy, where the solid line is the Green function $G_{\mathbf{k}}$ (4), and the dashed lines correspond to an additional interaction with collective modes or order parameter fluctuations.

As a consequence, the diagrammatic structure of the local self-energy remains identical to that of the standard DMFT, and we arrive at the following self-consistent set of equations of the generalized DMFT + Σ approach [35–37], which is solved applying the following iterative procedure:

(1) Start from some initial guess for the local self-energy $\Sigma(i\omega)$, for instance, $\Sigma(i\omega) = 0$.

(2) Calculate nonlocal self-energy $\Sigma_{\mathbf{k}}(i\omega)$ in the framework of some (approximate) scheme taking into account the interaction of correlated electrons with collective modes or

order parameter fluctuations, which, in general, can depend on $\Sigma(i\omega)$ and μ .

(3) Calculate the local Green function

$$G_{ii}(i\omega) = \frac{1}{N} \sum_{\mathbf{k}} \frac{1}{i\omega + \mu - \varepsilon(\mathbf{k}) - \Sigma(i\omega) - \Sigma_{\mathbf{k}}(i\omega)}. \quad (5)$$

(4) Define the ‘Weiss field’ as

$$\mathcal{G}_0^{-1}(i\omega) = \Sigma(i\omega) + G_{ii}^{-1}(i\omega). \quad (6)$$

(5) Using some ‘impurity solver’, calculate the single-particle Green function of an effective single-impurity Anderson model, i.e. compute the following integral over Grassmann variables $c_{i\sigma}^{\dagger}$ and $c_{i\sigma}$:

$$G_d(\tau - \tau') = \frac{1}{Z_{\text{eff}}} \int Dc_{i\sigma}^{\dagger} Dc_{i\sigma} c_{i\sigma}(\tau) c_{i\sigma}^{\dagger}(\tau') \exp(-S_{\text{eff}}), \quad (7)$$

where an effective action for the fixed site (‘Anderson impurity’) i has the form

$$S_{\text{eff}} = - \int_0^{\beta} d\tau_1 \int_0^{\beta} d\tau_2 c_{i\sigma}(\tau_1) \mathcal{G}_0^{-1}(\tau_1 - \tau_2) c_{i\sigma}^{\dagger}(\tau_2) + \int_0^{\beta} d\tau U n_{i\uparrow}(\tau) n_{i\downarrow}(\tau), \quad (8)$$

with the ‘partition function’ $Z_{\text{eff}} = \int Dc_{i\sigma}^{\dagger} Dc_{i\sigma} \times \exp(-S_{\text{eff}})$, and the upper limit of integration $\beta = T^{-1}$.

(6) Define *new* local self-energy as

$$\Sigma(i\omega) = \mathcal{G}_0^{-1}(i\omega) - G_d^{-1}(i\omega). \quad (9)$$

(7) Using last self-energy as an initial one in step 1, continue the loop procedure until it converges to

$$G_{ii}(i\omega) = G_d(i\omega) \quad (10)$$

with a given accuracy.

At the end, we obtain the final Green function in the form of Eqn (4), where $\Sigma(i\omega)$ and $\Sigma_{\mathbf{k}}(i\omega)$ are self-energies coming out of our iterative procedure.

The success of such an approach (as well as its main drawback) is connected with an additive form of total self-energy (neglect of the interference between different contributions) in Eqn (4). This allows one to preserve the self-consistent set of equations derived in the standard DMFT. However, there are two significant distinctions from the conventional DMFT. First of all, the local Green function of an effective single-impurity problem takes the form of Eqn (5) at each step of the DMFT procedure. Second, during each DMFT iteration, external self-energy $\Sigma_{\mathbf{k}}(i\omega)$ is recalculated within some (approximate) framework, taking into account, for instance, the interaction with collective modes (phonons, magnons, etc.) or with fluctuations of some order

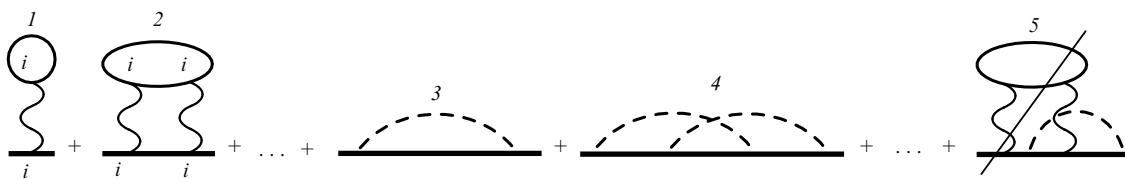


Figure 4. Typical skeleton self-energy diagrams of the DMFT + Σ approach.

parameter. To define nonlocal contribution $\Sigma_{\mathbf{k}}(i\omega)$, it is convenient to introduce the function

$$\mathcal{G}_{0\mathbf{k}}(i\omega) = \frac{1}{G_{\mathbf{k}}^{-1}(i\omega) + \Sigma_{\mathbf{k}}(i\omega)} = \frac{1}{i\omega + \mu - \varepsilon(\mathbf{k}) - \Sigma(i\omega)} \quad (11)$$

which plays the role of the bare Green function in building the perturbation theory with an external interaction as an expansion parameter. The choice of the bare Green function in the form of Eqn (11) guarantees that Green function ‘dressed’ by such an interaction, $G_{\mathbf{k}}^{-1}(i\omega) = \mathcal{G}_{0\mathbf{k}}^{-1}(i\omega) - \Sigma_{\mathbf{k}}(i\omega)$, entering the skeleton diagrams for $\Sigma_{\mathbf{k}}(i\omega)$, coincides exactly with the full Green function $G_{\mathbf{k}}(i\omega)$.

A remarkable feature of our approach is the possibility of its generalization to evaluate some two-particle properties, e.g. optical conductivity [38, 39]. The conductivity of a system is expressed via retarded density–density response function $\chi^R(\omega, \mathbf{q})$ [40–42]:

$$\sigma(\omega) = -\lim_{q \rightarrow 0} \frac{ie^2\omega}{q^2} \chi^R(\omega, \mathbf{q}), \quad (12)$$

where e is electron charge. This response function is defined by analytical continuation to real frequencies of the full polarization loop in Matsubara representation [40, 41]. Note that conductivity is completely defined by the first derivative of this response function with respect to q^2 in the limit of $q \rightarrow 0$. This circumstance, as well as the neglect of interference between the local Hubbard and external interactions in the DMFT + Σ approach and the locality of irreducible vertices of the Hubbard interaction, allow one to perform a partial resummation of diagrams relevant for finding conductivity, making use of an exact (in the limit of $q \rightarrow 0$) Ward identity. In the end, the real part of optical conductivity in the DMFT + Σ approach has the form [38, 39]

$$\begin{aligned} \text{Re } \sigma(\omega) = & \frac{e^2\omega}{2\pi} \int_{-\infty}^{\infty} d\varepsilon [f(\varepsilon_-) - f(\varepsilon_+)] \\ & \times \text{Re} \left\{ \phi_{\varepsilon}^{0\text{RA}}(\omega) \left[1 - \frac{\Sigma^R(\varepsilon_+) - \Sigma^A(\varepsilon_-)}{\omega} \right]^2 \right. \\ & \left. - \phi_{\varepsilon}^{0\text{RR}}(\omega) \left[1 - \frac{\Sigma^R(\varepsilon_+) - \Sigma^R(\varepsilon_-)}{\omega} \right]^2 \right\}, \quad (13) \end{aligned}$$

where

$$\phi_{\varepsilon}^{0\text{RR(RA)}}(\omega) = \lim_{q \rightarrow 0} \frac{\Phi_{\varepsilon}^{0\text{RR(RA)}}(\omega, \mathbf{q}) - \Phi_{\varepsilon}^{0\text{RR(RA)}}(\omega, 0)}{q^2} \quad (14)$$

and we introduced two-particle Green functions in the following form

$$\begin{aligned} \Phi_{\varepsilon}^{0\text{RR(RA)}}(\omega, \mathbf{q}) = & \sum_{\mathbf{k}} G^R(\varepsilon_+, \mathbf{k}_+) G^{R(A)}(\varepsilon_-, \mathbf{k}_-) \\ & \times \Gamma^{\text{RR(RA)}}(\varepsilon_-, \mathbf{k}_-; \varepsilon_+, \mathbf{k}_+), \quad (15) \end{aligned}$$

which are diagrammatically represented in Fig. 5 ($\mathbf{k}_{\pm} = \mathbf{k} \pm \mathbf{q}/2$, and $\varepsilon_{\pm} = \varepsilon \pm \omega/2$). Vertices $\Gamma^{\text{RR(RA)}}(\varepsilon_-, \mathbf{k}_-; \varepsilon_+, \mathbf{k}_+)$ contain all vertex corrections from external interactions (order parameter fluctuations, impurities, phonons, etc.) but *do not contain* vertex corrections from the Hubbard interaction.

Thus, one achieves a significant simplification of the problem. To calculate optical conductivity within the DMFT + Σ approach, we have only to solve the single-particle problem of obtaining the local self-energy $\Sigma(\varepsilon_{\pm})$ with the help of the DMFT + Σ procedure described above,

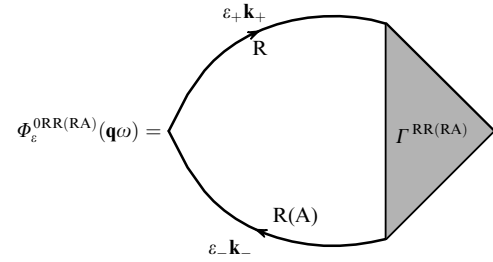


Figure 5. Diagrammatic representation of $\Phi_{\varepsilon}^{0\text{RA}}(\omega, \mathbf{q})$ and $\Phi_{\varepsilon}^{0\text{RR}}(\omega, \mathbf{q})$.

while a nontrivial contribution from nonlocal correlations or external perturbations enters via ‘blocks’ (14) which can be calculated in a suitable approximation accounting only for external interaction, with bare Green functions (11) containing the local self-energy from the DMFT + Σ procedure. In fact, Eqn (13) also provides an effective algorithm to compute optical conductivity in the framework of the conventional DMFT (neglecting all external nonlocal correlations). In this case, functions (14) could be easily found from the simple loop diagram defined by two Green functions and free *scalar* vertices. To get optical conductivity, there is actually no need to calculate vertex corrections in the framework of DMFT itself, as was first demonstrated for the loop with *vector* vertices in Refs [4, 5].

In what follows (see Sections 3 and 4), we shall discuss in detail some applications of the generalized DMFT + Σ approach to the solution of concrete physical problems.

2.3 Some other generalizations of DMFT

To date, a number of different theoretical approaches have been suggested to account for nonlocal effects within generalizations of DMFT. Here, we restrict ourselves to a brief review of some of these approaches.

First of all, we shall refer to the cluster methods already mentioned in Section 2.1. Instead of an isolated Anderson impurity, one can consider some cluster containing several such impurities, treating single-site correlations within DMFT, while considering intersite correlations with the aid of some other methods. This is the basic idea of the so-called cluster DMFT methods [5, 43–45].

A drawback of such approaches lies in the various treatment of nonlocal correlations inside a cluster and between clusters, though from the physical point of view (for example, because of translational invariance) they should be identical. To overcome this difficulty, it was proposed to average self-consistent ‘cluster’ self-energy over pairs of sites connected by translation vectors [43, 44]. Unfortunately, such an averaging procedure does not work well within the self-consistent DMFT cycle, since it breaks down the analytical properties of the Green function.

In some sense, the alternative approach referred to as the dynamical cluster approximation (DCA) was proposed in Refs [45–50]. This approach conserves translational invariance and ensures the physical behavior of the Green function. Within DCA, the Brillouin zone is divided into several cells with their centers defined by appropriate \mathbf{K} vectors. At the same time, self-energy is assumed to be constant in each cell, $\Sigma_{\mathbf{k}}(\omega) = \Sigma_{\mathbf{K}}(\omega)$, but these constants differ for different \mathbf{K} . On going over to a direct space, a difference between DCA and cluster DMFT lies in the fact that a DMFT-cluster in DCA satisfies periodic boundary

conditions, instead of open boundary conditions, as in the cluster DMFT.

The choice of a particular cluster method is dictated by the physical problem under consideration. Naturally, the common drawback of cluster approaches deals with essentially more computational resources than in the standard DMFT, which is connected with the solution of the appropriate cluster problem. Nevertheless, a number of successes have been achieved in this path. Cluster DMFT generalizations were applied to different models, as well as to studies of some realistic systems. A detailed review of this work can be found in Ref. [32].

Recently, a number of diagrammatic DMFT generalizations have been proposed, shooting for a more or less consistent construction of the perturbation theory with the inverse powers of spatial dimensionality as an expansion parameter, and with the standard DMFT used as the zero-order approximation. We mention in this connection Ref. [51] and the so-called dynamical vertex approximation (D Γ A) developed in Ref. [52]. Most promising in this respect seems to be the dual fermion approach formulated in Refs [53, 54], which puts in a claim on a consistent realization of such perturbation theory. Unfortunately, thus far only some simple model problems have been solved by applying these methods, while realistic systems have not yet been considered at all.

3. Application of generalized DMFT + Σ approach to model problems

3.1 Strongly correlated systems in the pseudogap state

3.1.1 Pseudogap fluctuations. A striking example of strongly correlated systems is provided by high- T_c cuprates. Parent stoichiometric cuprate compounds are antiferromagnetic (AFM) insulators with a well-developed optical gap and antiferromagnetism due to spin ordering on copper ions with a Néel temperature on the order of hundreds of kelvins. This insulating state is rapidly destroyed by the introduction of rather few doping impurities. Thus, these systems can be classified as doped Mott insulators with strong electronic correlations.

Among the many anomalies of the normal phase of high-temperature superconductors, observations of a pseudogap in the electronic spectra of underdoped cuprates are especially noteworthy [55, 56]. Despite continuing discussions about the physical nature of the pseudogap, the most preferable scenario of pseudogap formation from our point of view is that due to strong scattering of charge carriers on antiferromagnetic spin density wave (SDW) short-range order fluctuations [56, 57]. In the momentum representation, this scattering is characterized by momentum transfer on the order of $\mathbf{Q} = (\pi/a, \pi/a)$ (a is the two-dimensional lattice constant). This leads to the formation of certain features in the single-particle spectrum, which are precursors of changes in the spectra due to the appearance of AFM long-range order (period doubling). As a result, we end up with a non-Fermi liquid behavior (dielectrization) of the spectral density in the vicinity of so-called ‘hot-spots’ on the Fermi surface, appearing at intersections of the Fermi surface with the borders of the AFM Brillouin zone [56].

In the framework of this spin-fluctuation scenario, a simplified model of the pseudogap state was studied in Refs [56, 58–60]. This model is based on the assumption that, for high enough temperatures, the dynamics of spin

fluctuations can be neglected, and one can consider instead the scattering of charge carriers by a static Gaussian random field (quenched disorder) of pseudogap fluctuations (AFM short-range order fluctuations). Scattering intensity on fluctuations is characterized by a narrow peak near scattering vectors on the order of \mathbf{Q} with a width defined by inverse correlation length $\kappa = \xi^{-1}$ and corresponding energy scale Δ (on the order of pseudogap crossover temperature T^*).

For momentum-dependent self-energy, therefore, we shall concentrate on the case of electron scattering by such (SDW-like) antiferromagnetic spin fluctuations [a similar consideration also works fine for charge density wave (CDW-like) fluctuations] with short-range order. To calculate $\Sigma_{\mathbf{k}}(i\omega)$ for the case of electrons propagating in a quenched random field of Gaussian spin (or charge) fluctuations with a dominating scattering momentum in proximity to characteristic vector \mathbf{Q} (‘hot-spot’ model [56]), we shall apply the generalized version of the recurrent procedure proposed in Refs [58–61], allowing us to take into account *all* Feynman diagrams describing the scattering of electrons by this random field. This becomes possible because of a remarkable property of the simplified hot-spot model: *the contribution from an arbitrary diagram with crossing interaction lines is equal to the contribution of some diagram of the same order without crossing those lines* [61]. Thereby, we can restrict ourselves to the consideration of noncrossing diagrams only and take into account other diagrams by combinatorial prefactors attributed to interaction lines [60, 61]. Eventually, we arrive at the following recurrent relation for the self-energy (continuous fraction representation [60, 61]):

$$\Sigma_n(i\omega, \mathbf{k}) = \Delta^2 \frac{s(n)}{i\omega + \mu - \Sigma(i\omega) - \varepsilon_n(\mathbf{k}) + in v_n \kappa - \Sigma_{n+1}(i\omega, \mathbf{k})}. \quad (16)$$

Here, the term $\Sigma_n(i\omega, \mathbf{k})$ of the recurrent procedure contains all diagrammatic contributions with the number of interaction lines $\geq n$. The recurrent procedure for $\Sigma_n(i\omega, \mathbf{k})$ converges rather fast: we can put $\Sigma_n(i\omega, \mathbf{k})$ equal to zero for large enough n and, performing straightforward computations, obtain the desired physical self-energy at $n = 1$ [60], which can be subsequently used in the DMFT + Σ computational scheme:

$$\Sigma_{\mathbf{k}}(i\omega) = \Sigma_{n=1}(i\omega, \mathbf{k}). \quad (17)$$

Parameter Δ entering formula (16) characterizes the energy scale (width) of the pseudogap, $\kappa = \xi^{-1}$ is the inverse correlation length of SDW (CDW) fluctuations, $\varepsilon_n(\mathbf{k}) = \varepsilon(\mathbf{k} + \mathbf{Q})$ and $v_n = |v_{\mathbf{k}+\mathbf{Q}}^x| + |v_{\mathbf{k}+\mathbf{Q}}^y|$ for odd n , and $\varepsilon_n(\mathbf{k}) = \varepsilon(\mathbf{k})$ and $v_n = |v_{\mathbf{k}}^x| + |v_{\mathbf{k}}^y|$ for even n , where velocity projections $v_{\mathbf{k}}^x$ and $v_{\mathbf{k}}^y$ are defined by the usual derivatives of the bare electron dispersion $\varepsilon(\mathbf{k})$ with respect to corresponding momentum components. Finally, $s(n)$ are combinatorial prefactors defining the number of coinciding diagrams:

$$s(n) = n, \quad (18)$$

for the case of commensurate charge (CDW type) fluctuations with $\mathbf{Q} = (\pi/a, \pi/a)$ [61]. For incommensurate CDW fluctuations [61] (when \mathbf{Q} is not related to the lattice period), we get

$$s(n) = \begin{cases} \frac{n+1}{2} & \text{for odd } n, \\ \frac{n}{2} & \text{for even } n. \end{cases} \quad (19)$$

If we want to take into account the spin (Heisenberg) structure of interaction with spin fluctuations for a nearly antiferromagnetic Fermi liquid (spin-fermion model [58, 59]), the diagram combinatorics become more complicated. Scattering processes preserving spin projection are controlled by commensurate combinatorics, while spin flip scattering is described by incommensurate diagrams ('charged' random field, according to Refs [58, 59]). In this model, the recurrent procedure (16) for a single-particle Green function remains the same, but with other combinatorial prefactors $s(n)$ [58, 59]:

$$s(n) = \begin{cases} \frac{n+2}{3} & \text{for odd } n, \\ \frac{n}{3} & \text{for even } n. \end{cases} \quad (20)$$

Obviously, this procedure introduces an important length scale ξ , missed in standard DMFT. Physically, this length scale reflects the influence of short-range order fluctuations (SDW or CDW) on an electronic bath surrounding the effective Anderson impurity in DMFT.

After obtaining the self-consistent solution of DMFT + Σ set of equations (5)–(10) allowing also for nonlocal fluctuations, one can calculate the spectral density $A(\omega, \mathbf{k})$:

$$A(\omega, \mathbf{k}) = -\frac{1}{\pi} \text{Im} \frac{1}{\omega + \mu - \varepsilon(\mathbf{k}) - \Sigma(\omega) - \Sigma_{\mathbf{k}}(\omega)}, \quad (21)$$

where $\Sigma(\omega)$, $\Sigma_{\mathbf{k}}(\omega)$, and chemical potential μ have already been computed in a self-consistent way. The density of states can be found by integration of formula (21) over the Brillouin zone.

An analogous approach can also be developed to determine two-particle vertices. The basic idea employed here is the possibility of obtaining an arbitrary vertex diagram by introducing the 'external field' line into the corresponding self-energy diagram [62–64]. In the model under consideration, we can again restrict ourselves to non-crossing diagrams, while the contribution from all other diagrams can be accounted for by combinatorial prefactors $s(n)$ attributed to interaction lines [58–61]. Thus, all vertex diagrams are generated by the simple ladder diagrams with additional $s(n)$ prefactors linked to corresponding interaction lines [63, 64] (see also monograph [42]). Then, we obtain the following system of recurrent relations for the vertex $\Gamma_n^{\text{RA}}(\varepsilon_-, \mathbf{k}_-; \varepsilon_+, \mathbf{k}_+)$ [64], where the contribution of local DMFT self-energy (obtained within the DMFT + Σ procedure) is already included:

$$\begin{aligned} \Gamma_{n-1}^{\text{RA}}(\varepsilon_-, \mathbf{k}_-; \varepsilon_+, \mathbf{k}_+) &= 1 + \Delta^2 s(n) G_n^{\text{A}}(\varepsilon_-, \mathbf{k}_-) G_n^{\text{R}}(\varepsilon_+, \mathbf{k}_+) \\ &\times \left\{ 1 + 2iv_n \kappa k [\omega - \varepsilon_n(\mathbf{k}_+) + \varepsilon_n(\mathbf{k}_-) - \Sigma^{\text{R}}(\varepsilon_+) \right. \\ &+ \Sigma^{\text{A}}(\varepsilon_-) - \Sigma_{n+1}^{\text{R}}(\varepsilon_+, \mathbf{k}_+) + \Sigma_{n+1}^{\text{A}}(\varepsilon_-, \mathbf{k}_-)]^{-1} \left. \right\} \\ &\times \Gamma_n^{\text{RA}}(\varepsilon_-, \mathbf{k}_-; \varepsilon_+, \mathbf{k}_+), \end{aligned} \quad (22)$$

where

$$G_n^{\text{R,A}}(\varepsilon_{\pm}, \mathbf{k}_{\pm}) = \frac{1}{\varepsilon_{\pm} - \varepsilon_n(\mathbf{k}_{\pm}) \pm inv_n \kappa - \Sigma_n^{\text{R,A}}(\varepsilon_{\pm}) - \Sigma_{n+1}^{\text{R,A}}(\varepsilon_{\pm}, \mathbf{k}_{\pm})}. \quad (23)$$

'Physical' vertex $\Gamma_n^{\text{RA}}(\varepsilon_-, \mathbf{k}_-; \varepsilon_+, \mathbf{k}_+)$ is defined as $\Gamma_{n=0}^{\text{RA}}(\varepsilon_-, \mathbf{k}_-; \varepsilon_+, \mathbf{k}_+)$. Recurrent procedure (22) accounts for all diagrams of perturbation theory for the vertex part. In the limit of $\kappa \rightarrow 0$ ($\xi \rightarrow \infty$), formula (22) can be reduced to a series investigated in Ref. [62] (see also Refs [58, 59]), which can be exactly summed in analytical form. The standard ladder approximation is reproduced if all combinatorial factors $s(n)$ in formula (22) are made equal to unity for all n [63]. The recurrent procedure for $\Gamma_n^{\text{RR}}(\varepsilon_-, \mathbf{k}_-; \varepsilon_+, \mathbf{k}_+)$ differs from that in formula (22) by the evident change of $A \rightarrow R$ and by replacing the whole expression in curly brackets on the r.h.s. of Eqn (22) by unity.

Equations (4), (16), and (22), along with (13) and (14), describe the complete self-consistent procedure of calculating optical conductivity in our model within the framework of the DMFT + Σ approach.

An important aspect of our theory is the possibility of the microscopic calculation of both effective parameters Δ and ξ . For example, applying the two-particle self-consistent theory of Ref. [65], together with approximations introduced in Refs [58–60] for the two-dimensional Hubbard model, we derived a microscopic expression for Δ [35], which can be calculated within the standard DMFT. It can be shown, in particular, that for a wide range of hole doping the pseudogap amplitude Δ varies in the interval from t to $2t$ (t is the nearest neighbor hopping integral).

3.1.2 Basic electronic properties in the pseudogap state. Let us discuss results for the standard single-band Hubbard model on a square lattice with electron dispersion

$$\varepsilon(\mathbf{k}) = -2t(\cos k_x a + \cos k_y a) - 4t' \cos k_x a \cos k_y a, \quad (24)$$

where t and t' stand for the nearest and next-to-nearest hopping integrals.

The energy scale in the following is defined by the nearest neighbor hopping integral t , and the length scale by the lattice constant a . The numerical renormalization group (NRG) was used as the impurity solver [23, 24]. Detailed computational results on the single-particle properties demonstrating pseudogap anomalies can be found in Refs [35–37], and on optical conductivity in Ref. [38]. Here, we only discuss the most typical results corresponding mostly to the case of $t'/t = -0.4$ (characteristic for cuprates) and band filling $n = 0.8$ (hole doping).

Density of states and spectral function. Let us start with results obtained within the generalized DMFT + Σ approach for the densities of states (DOSs) corresponding to rather weak (compared with bandwidth) Coulomb interaction $U = 4t$. A characteristic feature of the strongly correlated metallic state is the coexistence of lower and upper Hubbard subbands split by Coulomb interaction U with the quasiparticle peak at the Fermi level [4, 5]. Because the unperturbed DOS for the square lattice has Van Hove singularity near the Fermi level, in general the peak on the Fermi level cannot be treated simply as a quasiparticle one. Actually, there are two contributions to this peak: (i) from a quasiparticle peak appearing in strongly correlated metals due to many-body effects, and (ii) from the smoothed Van Hove singularity of unperturbed DOS.³

³ With an increase in Coulomb repulsion, the Van Hove singularity gradually transforms into a quasiparticle peak at $U = (6-8)t$.

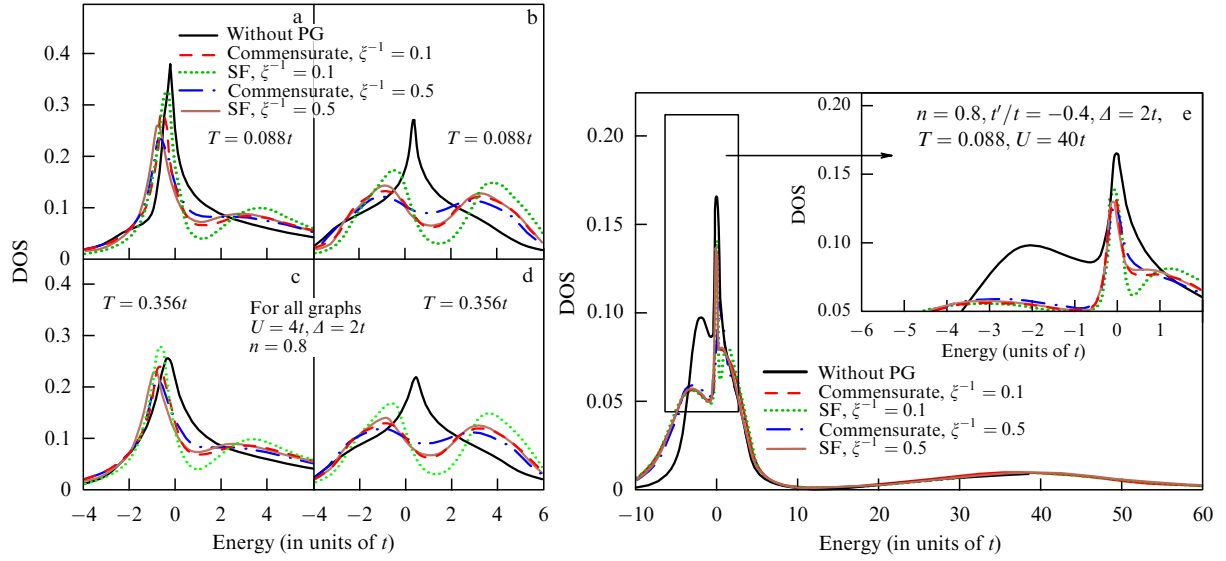


Figure 6. Comparison of DMFT(NRG)+ Σ DOSs calculated in Ref. [35] for different combinatorial prefactors (SF — spin-fermion model, commensurate fluctuations), inverse correlation lengths ξ^{-1} (in units of the lattice constant), pseudogap amplitude $\Delta = 2t$, and band filling $n = 0.8$: (a–d) $U = 4t$, at $t'/t = -0.4$ (figures a, c) and $t' = 0$ (figures b, d), two temperatures $T = 0.088t$ (upper part) and $T = 0.356t$ (lower part); (e) $U = 40t$, $T = 0.088t$. The Fermi level corresponds to zero energy.

On the left side of Fig. 6, we show DMFT + Σ DOSs with $n = 0.8$ for the case of $t'/t = -0.4$ (left panel) and $t' = 0$ (right panel) for two different temperatures $T = 0.356t$ (lower panel) and $T = 0.088t$ (upper panel). Black solid curves were obtained in the absence of fluctuations. The other curves in Fig. 6 present results for DOSs with nonlocal fluctuations with amplitude $\Delta = 2t$. For all parameter sets, we see that the introduction of nonlocal fluctuations leads to pseudogap formation on a quasiparticle peak. The width of the pseudogap (energy interval between corresponding peaks in the DOSs) is on the order of 2Δ . A decrease in the value of Δ from $2t$ to t gives a pseudogap width that is half the size and makes it less deep. A more pronounced pseudogap is found for spin-fermion-model combinatorial prefactors [see formula (20)], as compared with the case of commensurate charge fluctuations [combinatorial prefactors (19)]. The influence of the correlation length value corresponds to general expectations. A decrease in correlation length, or an increase from $\xi^{-1} = 0.1$ to $\xi^{-1} = 0.5$ for inverse correlation length, slightly smears the pseudogap. The rise in temperature from $T = 0.088t$ to $T = 0.356t$ leads to general broadening of DOS structures. One should note that DMFT + Σ results at $U = 4t$ (which is less than the bandwidth W) are qualitatively similar to the results obtained earlier in the absence of the Hubbard interaction [58–60].

Let us consider now the case of a doped Mott insulator with a Hubbard interaction value of $U = 40t$, $t'/t = -0.4$ and band filling $n = 0.8$ (right side of Fig. 6e). A characteristic feature of the DOSs for such strongly correlated metals is the strong splitting of the lower and upper Hubbard bands, with the Fermi level falling within the lower Hubbard band (the case of hole doping). In the absence of nonlocal fluctuations, the quasiparticle peak is again formed on the Fermi level. However, the upper Hubbard band resides now quite far away to the right and does not touch the quasiparticle peak (as it does for weak Coulomb interaction).

For strong enough nonlocal fluctuations with $\Delta = 2t$, the pseudogap appears in the middle of the quasiparticle peak,

and the lower Hubbard band is slightly broadened by fluctuation effects. Qualitatively, pseudogap anomaly behavior reminds us of that described above for the case of $U = 4t$ —a decrease in ξ smears the pseudogap and makes it less pronounced, and a decrease in Δ from $\Delta = 2t$ to $\Delta = t$ narrows the pseudogap and makes it more shallow (see Ref. [35]). Let us also notice that, for the doped Mott insulator, pseudogap is more evident for spin SDW-like fluctuations than for charge CDW-like ones.

Nevertheless, there are quite appreciable distinctions in contrast to the $U = 4t$ case. For example, the width of the pseudogap in the DOS is found to be essentially smaller than 2Δ , which is connected, in our opinion, with noticeable narrowing of the quasiparticle peak itself caused by local correlations.

In Fig. 7, we show spectral densities $A(\omega, \mathbf{k})$, calculated within the DMFT + Σ approach, along high-symmetry directions of the first Brillouin zone: $\Gamma(0, 0) - X(\pi, 0) - M(\pi, \pi) - \Gamma(0, 0)$. In fact, this figure displays the quasiparticle band of a many-body system—positions of maxima of spectral densities specify quasiparticle dispersion, while their width defines quasiparticle damping. Also, we clearly observe the partial reconstruction (‘destruction’) of this band by pseudogap fluctuations. One can see a characteristic double-peak pseudogap structure in proximity to the X-point of the Brillouin zone. In the middle of the M– Γ direction (the so-called ‘nodal’ point), one can observe the emergence of the pseudogap, i.e. the presence of ‘memory’ of the AFM gap, which has a maximum here in the case of AFM long-range order. Generally speaking, changing the filling leads to a common shift of spectral functions with respect to the Fermi level.

Fermi surface ‘destruction’. Within conventional DMFT, the Fermi surface is not renormalized by interaction, i.e. it remains the same as for bare quasiparticles [3]. However, in the case of nontrivial momentum dependence of self-energy, substantial renormalization of the Fermi surface may occur due to pseudogap formation [58, 59]. There are several ways

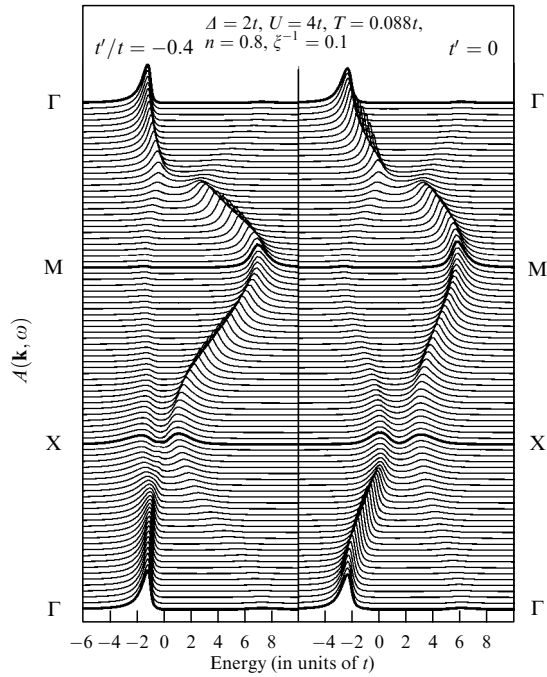


Figure 7. DMFT(NRG)+ Σ spectral densities $A(\mathbf{k}, \omega)$ [35] along high-symmetry directions of the first Brillouin zone $\Gamma(0,0)$ – $X(\pi,0)$ – $M(\pi,\pi)$ – $\Gamma(0,0)$, for spin-fermion diagram combinatorics (SF). The Fermi level is at zero energy.

to define the Fermi surface for strongly correlated systems. Below, we shall exploit the intensity map of the spectral function (spectral density) (21) at $\omega = 0$, which is often called the Fermi surface map. Such a map is directly measured in ARPES experiments, and positions of its intensity maxima specify the Fermi surface in the sense of the usual Fermi-liquid theory, where quasiparticle damping becomes negligibly small.

On the left side of Fig. 8, these maps are displayed for strongly correlated metal with $U = 4t$. This contour plot of the spectral function clearly demonstrates the ‘destruction’ of the Fermi surface in the ‘hot-spots’, attended with the

formation of the ‘Fermi arcs’ upon Δ growth, similar to that observed in the pioneer work of Ding et al. [66], which was later confirmed in a large number of other studies. One should note that qualitatively analogous behavior is also evidenced in the absence of local electron correlations ($U = 0$) [36, 67]. The role of finite U values adds up to a decrease in spectral function intensity when compared with the case of $U = 0$ and leads to additional ‘smearing’, making hot-spots less visible. Destruction of the Fermi surface starts in the vicinity of hot spots for small Δ , but practically simultaneously it disappears in the whole antinodal region [near points $X(\pi,0)$, $Y(0,\pi)$] of the Brillouin zone, while only ‘Fermi arcs’ in the nodal region remain, with the shape close to the bare Fermi surface. Those results naturally explain why in ARPES experiments the clear hot spots behavior is rather rarely observed [68]. The question of the possibility of observing hot spots will be elucidated in more detail in Section 4.4 below, devoted to the LDA + DMFT + Σ description of realistic cuprates.

In the case of a doped Mott insulator with $U = 40t$, shown in Fig. 8b, we see that the Fermi surface is rather ill-defined for all values of Δ . The profile of the spectral function is significantly more smeared for the smaller values of U , reflecting the important role of local correlations.

For comparison, we also show in Fig. 8 the renormalized Fermi surfaces obtained in this model by formal solution of equation (25)⁴

$$\omega - \varepsilon(\mathbf{k}) + \mu - \text{Re} \Sigma(\omega) - \text{Re} \Sigma_{\mathbf{k}}(\omega) = 0 \quad (25)$$

at $\omega = 0$, used, for example, in the studies [58, 59]. Obviously, this definition gives a Fermi surface close to the one obtained from the intensity map for small Δ , but does not account for its significant damping essential for large Δ . For large

⁴ This definition is used in the standard Fermi-liquid theory. In fact, in our particular case the influence of nonlocal pseudogap fluctuations leads to qualitative changes in the simple Fermi-liquid picture. Herewith, we leave aside the question of whether the Fermi-liquid theory is applicable on such a defined Fermi surface or not, as well in the limit $T \rightarrow 0$, since the static approximation used is by construction the high-temperature one — short-range order AFM fluctuations can be considered as quasistatic only if $T \gg \omega_{\text{SF}}$, where ω_{SF} is the characteristic frequency of spin fluctuations [58–60].

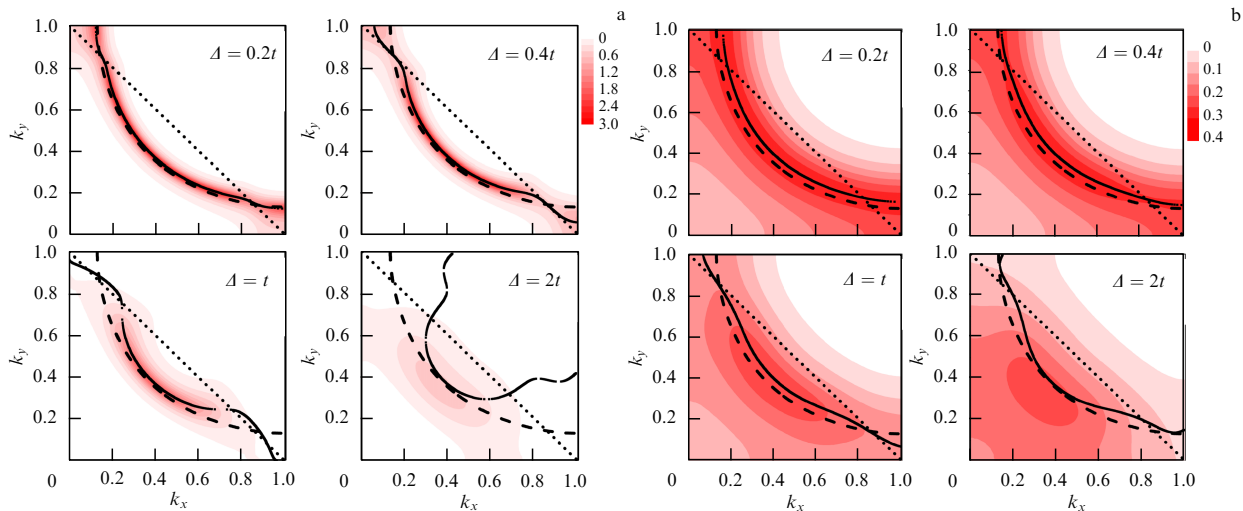


Figure 8. DMFT(NRG)+ Σ picture of Fermi surface ‘destruction’ taken from Ref. [36]. On the left for $U = 4t$, and on the right for $U = 40t$ at various values of Δ specified in the figures. Band filling is $n = 0.8$. Dashed lines — ‘bare’ Fermi surface, dotted lines — boundaries of a Brillouin magnetic zone, and solid lines — solutions of equation (25).

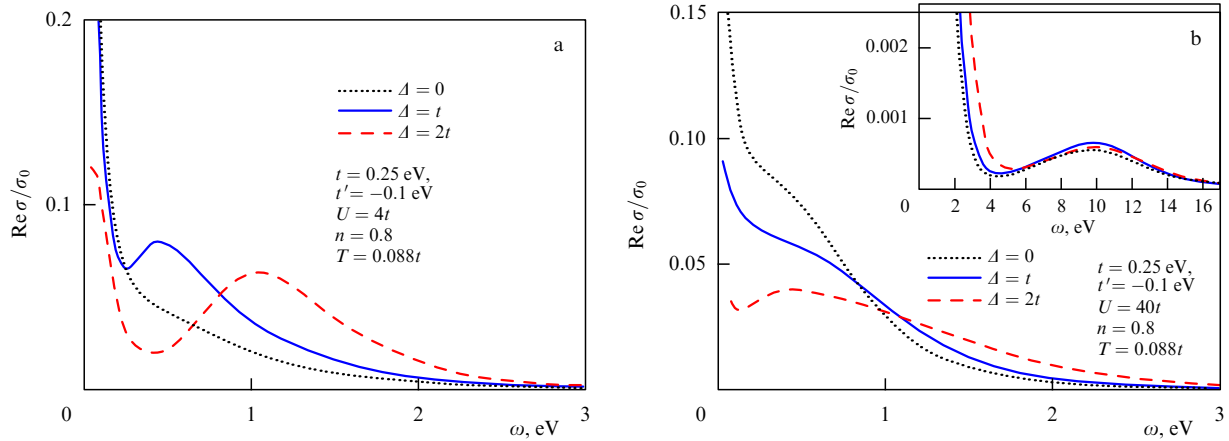


Figure 9. Real part of DMFT + Σ optical conductivity ($t' = -0.4t$, $t = 0.25$ eV) evaluated in Ref. [38] for various values of the pseudogap amplitude: $\Delta = 0$, $\Delta = t$, $\Delta = 2t$. Temperature is $T = 0.088t$, band filling $n = 0.8$ and correlation length $\xi = 10a$. (a) Strongly correlated metal with $U = 4t$. (b) Doped Mott insulator with $U = 40t$. Inset displays conductivity in a wide frequency range which includes transitions to the upper Hubbard band.

pseudogap amplitudes, this definition of the Fermi surface is qualitatively adequate for the true behavior, resulting from spectral function analysis, only in the nodal region. It is the contour plot of the spectral function (at $\omega = 0$) that gives the most complete and natural representation of the Fermi surface for systems with strong correlations and nonlocal fluctuations of some order parameter, which are present in a wide region of the phase diagram of high- T_c cuprate type systems because of their lessened dimensionality. Results obtained in a such an approach directly correspond to ARPES experiments, where exactly this definition of the Fermi surface is most conventional.

Optical conductivity. Let us set about discussing DMFT + Σ results for optical conductivity in the pseudogap state. In the left panel of Fig. 9, we give DMFT + Σ results for the real part of optical conductivity in the case of strongly correlated metal ($U = 4t$) for different pseudogap amplitudes. We clearly observe the formation of a typical pseudogap anomaly on the ‘shoulder’ of the Drude peak, and, as would be expected, it grows as Δ increases. This behavior is rather similar to the ‘mid-infrared feature’ which is evidenced in the optical conductivity of cuprate superconductors [69, 70]. The rise in temperature and decrease in fluctuation correlation length smear the pseudogap, making this anomaly less pronounced [38].

The right panel of Fig. 9 demonstrates DMFT + Σ optical conductivity of a doped Mott insulator ($U = 40t$) for several values of the pseudogap amplitude. We see that the frequency range, where the pseudogap anomaly manifests itself, gets narrower with the growth in local correlation strength, and for large U values pseudogap anomalies are strongly suppressed. Pseudogap fluctuations lead to noticeable changes in optical conductivity only for relatively low frequencies of order Δ . For higher frequencies (e.g. on the order of U , where transitions to the upper Hubbard band take place), pseudogap effects do not show themselves (see also inset to the right panel of Fig. 9). For low frequencies, we observe suppression of the Drude peak with a rather weak anomaly near $\omega \sim \Delta$, which disappears for small Δ or for short correlation lengths.

3.2 Mott–Anderson transition in disordered systems

The importance of accounting for both electron interactions and disorder effects in condensed matter research is well

known [71, 7]. Coulomb interactions and disorder are two driving forces leading to metal–insulator transitions, connected with localization and delocalization of charge carriers. In particular, the Mott–Hubbard transition is caused by electron repulsion [1, 73], while the Anderson metal–insulator transition is related to the scattering of noninteracting particles by impurities [74]. It is well known that a subtle competition between disorder and interaction effects has many manifestations [71, 72, 75, 76]. This problem is most relevant in the case of strong disorder and strong electron correlations, determining the physical mechanisms of the Mott–Anderson metal–insulator transition [71, 72].

One of the main models allowing for the account of both electronic correlations (leading to the Mott metal–insulator transition [1, 73]) and strong disorder effects (leading to the Anderson metal–insulator transition) is the Anderson–Hubbard model [39, 77–82].

In Refs [77–79], the three-dimensional Anderson–Hubbard model was investigated in the framework of dynamical mean-field theory [3–5, 14]. The influence of local disorder was taken into account through averaged densities of states [83, 84] within the well-known coherent potential approximation (CPA) which does not describe Anderson localization. To overcome this difficulty, Dobrosavljević and Kotliar [77] have proposed a version of DMFT where the self-consistent solution of stochastic DMFT equations for an ensemble of systems with given realizations of disorder was used to calculate the averaged logarithmic (geometric mean) density of states, which gives information on critical disorder for the Anderson transition. This approach was further developed in Refs [78, 89], where a highly nontrivial phase diagram of the three-dimensional paramagnetic Anderson–Hubbard model [79] was obtained, containing a correlated metal phase, a Mott insulating phase, and a correlated Anderson insulator phase. The main problem of the approach worked out in Refs [77–79] is the impossibility of direct computation of measurable physical properties, such as conductivity which actually defines the metal–insulator transition.

At the same time, there exists the well-developed self-consistent theory of Anderson localization, based on the solution of equations for the generalized diffusion coefficient. The efficiency of this approach in the absence of interactions has been known for a long time [40–42, 56, 85–87]; certain attempts to include interaction effects in this

approach were undertaken with some promising results in Refs [86, 88, 89]. However, up to now this approach has not been extended to the modern theory of strongly correlated systems. Such an investigation was performed for the first time in Ref. [39] for three-dimensional systems, and later for the two-dimensional case [90].

Let us consider the disordered paramagnetic Anderson–Hubbard model at (mostly) half-filling for arbitrary interaction strength and disorder. Obviously, this model contains both Mott–Hubbard and Anderson metal–insulator transitions. The Hamiltonian of the model is given by

$$H = -t \sum_{\langle ij \rangle \sigma} a_{i\sigma}^\dagger a_{j\sigma} + \sum_{i\sigma} \epsilon_i n_{i\sigma} + U \sum_i n_{i\uparrow} n_{i\downarrow}, \quad (26)$$

where $t > 0$ is the nearest neighbor hopping amplitude, while U is on-site Hubbard repulsion, $n_{i\sigma} = a_{i\sigma}^\dagger a_{i\sigma}$ is the particle number operator on site, and $a_{i\sigma}$ ($a_{i\sigma}^\dagger$) is the annihilation (creation) operator of electrons on site i with spin σ . Local energies ϵ_i are assumed to be random and independent on different lattice sites. To simplify the diagram technique hereinafter, we assume the Gaussian distribution for ϵ_i :

$$\mathcal{P}(\epsilon_i) = \frac{1}{\sqrt{2\pi\Delta}} \exp\left(-\frac{\epsilon_i^2}{2\Delta^2}\right). \quad (27)$$

Parameter Δ here is the measure of disorder. Such a Gaussian random field (‘white noise’) of energy levels ϵ_i at different lattice sites is equivalent to impurity scattering and can be described by the standard diagram technique for the averaged Green functions [42].

Self-energy $\Sigma_{\mathbf{p}}(i\epsilon)$ brought about by scattering on disorder may be evaluated in the simple one-loop approximation neglecting ‘crossing’ diagrams (i.e. in the self-consistent Born approximation) [42], which gives for Gaussian disorder (27) the following result

$$\Sigma_{\mathbf{p}}(i\epsilon) = \Delta^2 \sum_{\mathbf{p}} G(i\epsilon, \mathbf{p}) \equiv \Sigma_{\text{imp}}(i\epsilon), \quad (28)$$

so that our ‘external’ self-energy turns out to be independent of \mathbf{p} momentum (i.e., local).

To analyze optical conductivity, we shall apply the general DMFT + Σ expression (13). The most important block $\Phi_{\epsilon}^{\text{ORA}}(\omega, \mathbf{q})$ can be evaluated using the ideology of self-consistent theory of localization [40–42, 56, 85–87], with some generalizations accounting for the role of Hubbard interaction via the DMFT + Σ approach [39, 90]. The main distinction from the standard derivation of the equations of self-consistent theory of localization is the use of Green functions (4) containing a local contribution to self-energy from the Hubbard interaction.

Following the standard derivation [40–42, 56, 85–87], we obtain a diffusion-like (for small ω and q) contribution to $\Phi_{\epsilon}^{\text{ORA}}(\omega, \mathbf{q})$, which takes the form

$$\Phi_{\epsilon}^{\text{ORA}}(\tilde{\omega}, \mathbf{q}) = \frac{2\pi N(\epsilon)}{\tilde{\omega} + iD(\omega)q^2}, \quad (29)$$

where $D(\omega)$ is the generalized diffusion coefficient, and an important difference from the single-particle case is contained in the term

$$\begin{aligned} \tilde{\omega} &= \epsilon_+ - \epsilon_- - \Sigma^{\text{R}}(\epsilon_+) + \Sigma^{\text{A}}(\epsilon_-) \\ &= \omega - \Sigma^{\text{R}}(\epsilon_+) + \Sigma^{\text{A}}(\epsilon_-) \equiv \omega - \Delta\Sigma^{\text{RA}}(\omega), \end{aligned} \quad (30)$$

which substitutes for the usual ω term in the denominator of the standard expression for $\Phi_{\epsilon}^{\text{ORA}}(\omega, \mathbf{q})$. From general considerations, it is clear that in the metallic phase as $\omega \rightarrow 0$ we have $\Delta\Sigma^{\text{RA}}(\omega = 0) = 2i \text{Im}\Sigma(\epsilon) \sim \max\{T^2, \epsilon^2\}$, which reflects the Fermi-liquid behavior in DMFT (which is not violated by elastic impurity scattering). For finite T , it leads to the usual phase decoherence caused by (inelastic) electron–electron scattering [71, 72, 75, 76].

Equation (13) then takes the form

$$\begin{aligned} \text{Re } \sigma(\omega) &= \frac{e^2 \omega}{2\pi} \int_{-\infty}^{\infty} d\epsilon (f(\epsilon_-) - f(\epsilon_+)) \\ &\times \text{Re} \left[\frac{2\pi N(\epsilon) D(\omega)}{\omega^2} - \phi_{\epsilon}^{\text{ORR}}(\omega) \left(1 - \frac{\Delta\Sigma^{\text{RR}}(\omega)}{\omega} \right)^2 \right], \end{aligned} \quad (31)$$

where the second term in square brackets can, in fact, be neglected for small ω , while, if needed to describe a wide frequency range, it can be calculated using formula (14) with $\Phi_{\epsilon}^{\text{ORR}}(\omega, \mathbf{q})$ taken in the usual ladder approximation.

Next, following the standard framework of the self-consistent theory of localization [40–42, 56, 85–87], we get the closed self-consistent equation for the generalized diffusion coefficient

$$\begin{aligned} D(\omega) &= i \frac{\langle v \rangle^2}{d} \left(\tilde{\omega} - \Delta\Sigma_{\text{imp}}^{\text{RA}}(\omega) \right. \\ &\left. + \Delta^4 \sum_{\mathbf{p}} (\Delta G_{\mathbf{p}})^2 \sum_{\mathbf{q}} \frac{1}{\tilde{\omega} + iD(\omega)q^2} \right)^{-1}, \end{aligned} \quad (32)$$

where d is the spatial dimensionality, $\Delta G_{\mathbf{p}} = G^{\text{R}}(\epsilon_+, \mathbf{p}) - G^{\text{A}}(\epsilon_-, \mathbf{p})$, $\Delta\Sigma_{\text{imp}}^{\text{RA}}(\omega) = \Sigma_{\text{imp}}^{\text{R}}(\epsilon_+) - \Sigma_{\text{imp}}^{\text{A}}(\epsilon_-)$, and average velocity $\langle v \rangle$, which can be well approximated just by the Fermi velocity, is given by the following expression

$$\langle v \rangle = \frac{\sum_{\mathbf{p}} |\mathbf{v}_{\mathbf{p}}| \Delta G_{\mathbf{p}}}{\sum_{\mathbf{p}} \Delta G_{\mathbf{p}}}, \quad (33)$$

where $\mathbf{v}_{\mathbf{p}} = \partial\epsilon(\mathbf{p})/\partial\mathbf{p}$. Equation (32) should be solved jointly with following the self-consistent DMFT + Σ procedure (5)–(10), (28). In fact, this equation is a transcendental one and can be easily solved by iterations for each $\tilde{\omega}$ value.

In accordance with the usual applicability limit of the diffusion approximation, summation over q in Eqn (32) should be restricted to [42, 86]

$$q < k_0 = \min \{l^{-1}, p_{\text{F}}\}, \quad (34)$$

where $l = \langle v \rangle / 2\gamma$ is an elastic mean free path, γ is the Born scattering frequency by impurities, and p_{F} is the Fermi momentum. It is well known that in the two-dimensional case Anderson localization occurs at any infinitely weak disorder. However, the localization radius in this case is exponentially large, and the sample size begins to play a significant part. Sample size L can be introduced into the self-consistent theory of localization by cutting off the integration of the diffusion pole at small q [40, 41, 85], i.e. at

$$q \sim k_L = \frac{1}{L}. \quad (35)$$

When $\omega \rightarrow 0$ [and obviously $\tilde{\omega} \rightarrow 0$ on the Fermi surface ($\epsilon = 0$)], in the Anderson insulator phase one gets a localization behavior of the generalized diffusion coeffi-

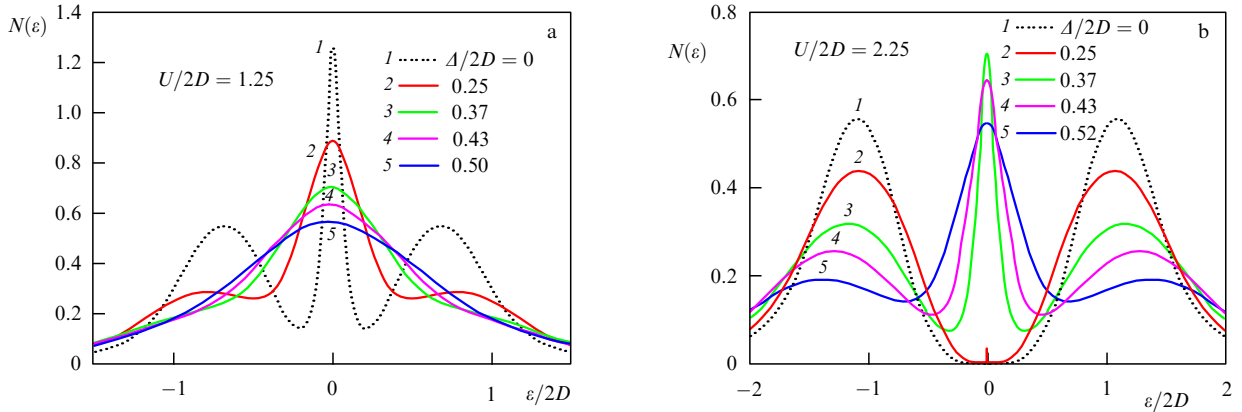


Figure 10. Anderson–Hubbard model density of states at half-filling for various disorder levels Δ [39]: (a) correlated metal with $U = 2.5D$, and (b) Mott insulator with $U = 4.5D$.

cient [40–42, 85]:

$$D(\omega) = -i\tilde{\omega}R_{\text{loc}}^2. \quad (36)$$

After substituting formula (36) into equation (32), one obtains an equation defining localization radius R_{loc} :

$$R_{\text{loc}}^2 = -\frac{\langle v \rangle^2}{d\Delta^4} \left\{ \sum_{\mathbf{p}} (\Delta G_{\mathbf{p}})^2 \sum_{\mathbf{q}} \frac{1}{1 + R_{\text{loc}}^2 q^2} \right\}^{-1}. \quad (37)$$

3.2.1 Three-dimensional systems. Below, we present the most interesting results for the three-dimensional Anderson–Hubbard model at half-filling on a cubic lattice with a model semielliptic bare density of states with the bandwidth $W = 2D$:

$$N_0(\varepsilon) = \frac{2}{\pi D^2} \sqrt{D^2 - \varepsilon^2}. \quad (38)$$

The density of states is always given in units of the number of states per energy interval for a unit cell of the volume a^3 (a is the lattice constant) and for one spin projection. Conductivities are given in natural units of $e^2/\hbar a$. For more detailed numerical results (also accounting for deviations from half-filling), we refer the reader to paper [39].

Evolution of the density of states. Within the standard DMFT approach, the Hubbard model density of states at half-filling has a typical three-peak structure [4, 5, 91, 92] with a narrow quasiparticle band (central peak) at the Fermi level and wide upper and lower Hubbard bands situated at energies $\varepsilon \sim \pm U/2$. As U grows, the quasiparticle band narrows within the metallic phase and disappears at the Mott–Hubbard metal–insulator transition at critical interaction $U_{c2} \approx 1.5W$. With a further increase in U , the insulating gap opens at the Fermi level.

We present in Fig. 10 our results for DMFT + Σ densities of states for a typical strongly correlated metal with $U = 2.5D = 1.25W$, in the absence of disorder and for different values of disorder Δ , including strong enough disorder transforming a correlated metal into a correlated Anderson insulator (see also below the discussion concerning optical conductivity). As one would expect, disorder leads to typical broadening and suppression of the density of states.

More unexpected is the result obtained for $U = 4.5D = 2.25W$, typical for Mott insulators and shown in the right panel of Fig. 10. Here we observe restoration of the central

peak (quasiparticle band) in the DOS with an increase in disorder, transforming the Mott insulator into a correlated metal or into a correlated Anderson insulator. Similar DOS behavior was also reported in Ref. [79].

The physical origin of such quite unexpected central peak restoration is pretty clear. The control parameter of metal–insulator transition in DMFT is the ratio of Hubbard interaction U to bare bandwidth $W = 2D$. With disorder coming into play (in the absence of Hubbard interaction), new effective bandwidth W_{eff} appears and grows with increasing disorder. A semielliptic form of the DOS with well-defined band edges in the self-consistent Born approximation (28) is preserved. This all leads to diminishing the ratio U/W_{eff} , which in turn causes restoration of the quasiparticle band. This issue is discussed in more detail below, when considering the phase diagram of the Anderson–Hubbard model.

In the absence of disorder, a characteristic feature of the Mott–Hubbard metal–insulator transition is hysteresis DOS behavior appearing with a decrease in U starting from the insulating phase [5, 91, 92]. The Mott insulating phase is conserved (metastable) down to rather small U values ‘wedging’ deep in the correlated metal phase. The metallic phase is restored only at about $U_{c1} \approx 1.0W$. Corresponding interval $U_{c1} < U < U_{c2}$ is typically considered a coexistence region of the metallic and Mott insulating phases, where, from a thermodynamic point of view, the metallic phase is more stable [5, 91–93]. Such hysteresis DOS behavior (see Ref. [39]) is also observed in the presence of disorder and will be described below during the discussion of the phase diagram of the Anderson–Hubbard model.

Optical conductivity: Mott–Hubbard and Anderson transitions. Without disorder, our calculations reproduce conventional DMFT results [4, 5], where optical conductivity is characterized by the usual Drude peak at low frequencies and a wide maximum at about $\omega \sim U$, which corresponds to optical transitions to the upper Hubbard band. As U grows, the Drude peak diminishes and disappears at the Mott transition, when only the contribution from transitions through the Mott–Hubbard gap remains valid. The introduction of disorder leads to a qualitative change in the frequency dependence of optical conductivity.

In the left panel of Fig. 11, we depict the real part of optical conductivity of the Anderson–Hubbard model at half-filling for different disorder levels Δ and $U = 2.5D$ typical for correlated metal. Then, transitions to the upper Hubbard

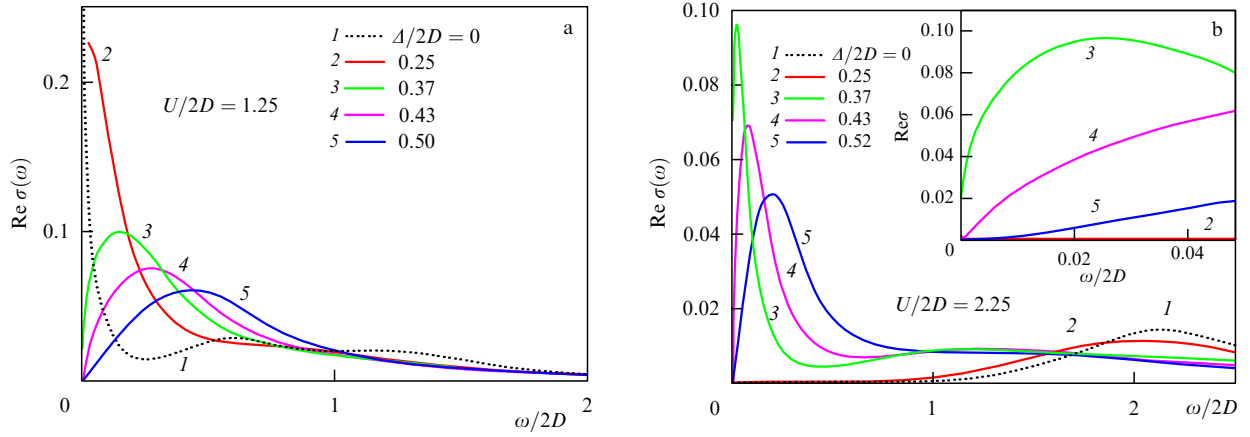


Figure 11. Real part of optical conductivity in the Anderson–Hubbard model at half-filling for different disorder levels Δ [39]. (a) Typical correlated metal with $U = 2.5D$. Curves 1, 2 — metallic phase, curve 3 corresponds to the mobility edge (Anderson transition), and curves 4, 5 — correlated Anderson insulator. (b) Typical Mott insulator with $U = 4.5D$. Curves 1, 2 correspond to the Mott insulator, curve 3 — mobility edge (Anderson transition), and curves 4, 5 — correlated Anderson insulator. Inset to figure b displays magnified low-frequency region.

bands at energies $\omega \sim U$ are almost unobservable. However, it is clearly visible that the metallic Drude peak typically centered at zero frequency is broadened and suppressed by disorder, gradually transforming into a peak at a finite frequency because of Anderson localization effects. The Anderson transition takes place at $\Delta_c \approx 0.74D = 0.37W$ (corresponding to curve 3 in all figures here and also in Fig. 10 for the DOS). Notice that this value depends on the cutoff (34) which is defined up to the coefficient of the order of unity [42, 86]. Naive expectations can bring us to the conclusion that the narrow quasiparticle band at the Fermi level, being formed in a strongly correlated metal, may be localized much more easily than the normal conduction band. However, we see that these expectations are wrong and the band localizes only at rather large disorder, $\Delta_c \sim D$, similar to that for the conduction band with a width of $\sim W$. The latter agrees with the known analysis of localization in the two-band model [94].

In the DMFT + Σ approach, critical disorder Δ_c does not depend on U , as interaction effects enter Eqn (32) only through $\Delta\Sigma^{\text{RA}}(\omega) \rightarrow 0$ as $\omega \rightarrow 0$ (for $T = 0$, $\varepsilon = 0$), and the influence of interaction at $\omega = 0$ disappears. In fact, this is the main shortcoming of the DMFT + Σ approach originating from the neglect of the interference effects between interaction and impurity scattering. Significant role of these interference effects has been known for a long time [71, 72, 75, 76]. On the other hand, the neglect of these effects allows performing the reasonable physical interpolation between two main limits — that of the Anderson transition because of disorder, and Mott–Hubbard transition because of strong correlations. Thus, one can consider this approximation as a reasonable first step to a future complete theory of metal–insulator transitions in strongly correlated disordered systems.

In Fig. 11b, we show the real part of optical conductivity of a Mott–Hubbard insulator with $U = 4.5D$ at different disorder levels Δ . In the inset to this figure we show low-frequency data demonstrating different types of conductivity behavior, especially close to the Anderson transition and within the Mott insulating phase. In the main part of the figure, the contribution to conductivity from transitions to the upper Hubbard band at about $\omega \sim U$ is distinctly seen. Disorder growth results in an origin of finite conductivity for

the frequency range inside the Mott–Hubbard gap, which correlates with the restoration of the quasiparticle band in the DOS within the gap, as shown in Fig. 10b. This conductivity for $\Delta < \Delta_c$ is metallic (finite in the static limit $\omega = 0$), and for $\Delta > \Delta_c$ at low frequencies we get $\text{Re}\sigma(\omega) \sim \omega^2$, which is typical for an Anderson insulator [40–42, 56, 85–87].

The appearance of a peak in $\text{Re}\sigma(\omega)$ at low finite frequencies even in the metallic phase is a bit unusual. This happens because of the importance of localization effects. In the ladder approximation for $\Phi_e^{\text{ORA}}(\omega, \mathbf{q})$, which neglects all localization corrections, we obtain the usual Drude peak at $\omega = 0$ [39], while the inclusion of localization effects shifts the peak in $\text{Re}\sigma(\omega)$ to low (but finite) frequencies. As is well known [1], the metallic state is defined by finite static ($\omega = 0$) conductivity at zero temperature.

Above, we only presented conductivity data obtained when there is an increase in U from values typical to metallic phase to those for Mott insulating phase. As U decreases from values common to the Mott insulating phase, we observe the hysteresis of conductivity in the phase coexistence region defined (in the absence of disorder) by inequality $U_{c1} < U < U_{c2}$. A hysteresis of conductivity also shows itself in the coexistence region in the presence of disorder. Details of this behavior of optical conductivity can be found in Ref. [39].

Phase diagram of Anderson–Hubbard model at half-filling. The phase diagram of the Anderson–Hubbard model at half-filling was studied in Ref. [79], using direct DMFT calculations for the lattice with a finite number of sites with random realizations of energies ε_i in Hamiltonian (26) and subsequent averaging over these realizations to get an averaged DOS and geometrically mean local DOS which allows one to define critical disorder for transition into the Anderson insulator phase. Below, we present our results on the Anderson–Hubbard paramagnetic phase diagram with half-filling, obtained from the DOS and optical conductivity calculations within the DMFT + Σ approach. It should be emphasized that conductivity analysis is the most direct way to distinguish metallic and insulating phases [1].

A (Δ, U) phase diagram calculated at zero temperature in the disorder–correlation plane is shown in Fig. 12a. Anderson transition line $\Delta_c \approx 0.37W = 0.74D$ is defined as a disorder strength for which static conductivity becomes zero at $T = 0$.

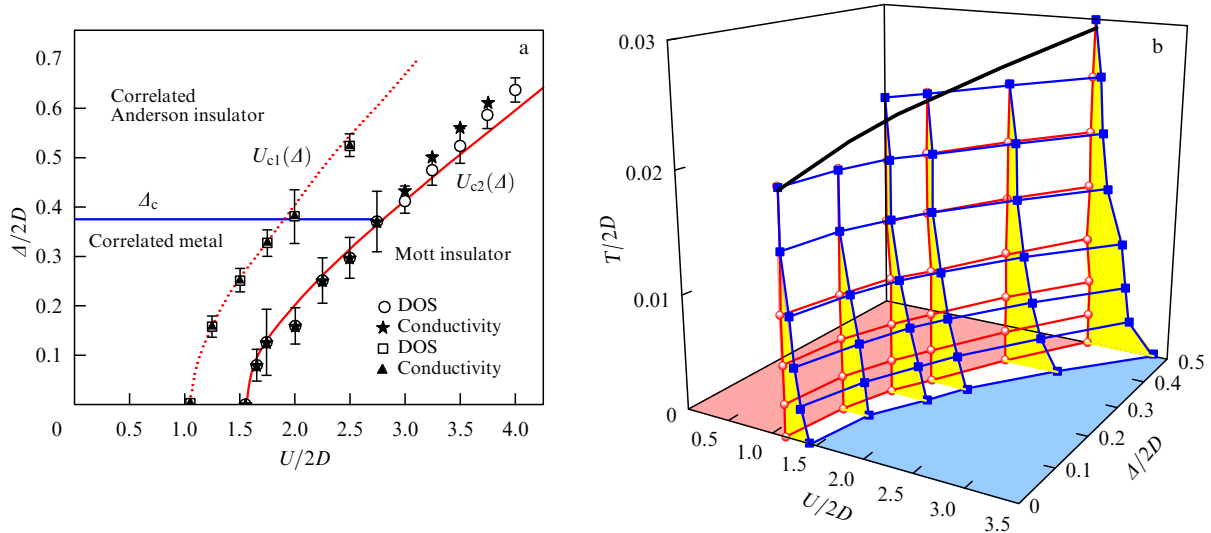


Figure 12. Phase diagram of the paramagnetic Anderson–Hubbard model. (a) Zero-temperature case [39]. Continuous curves $U_{c1,c2}(\Delta)$ are Mott insulating phase boundaries obtained from analytical estimate of Eqn (41); different symbols represent results for these boundaries obtained from calculations from the DOS and optical conductivity. Line of Anderson transition is given by $\Delta_c = 0.37$. (b) Boundaries of Mott insulating phase and phase coexistence region at various temperatures. Points are obtained from DOS calculations. Solid black curve is a linear fit [$T_c/2D = 0.02(1 + \Delta/2D)$] to the T_c points, where the coexistence region disappears.

The Mott–Hubbard transition can be detected from the central (quasiparticle) peak disappearance in the DOS or from optical conductivity behavior based on observations of gap closing in the insulating phase or from static conductivity disappearance in the metallic phase.

We have already noticed that the DMFT + Σ approximation gives a universal (U -independent) strength of critical disorder Δ_c because of the neglect of interference between disorder scattering and Hubbard interaction. This leads to differences between the phase diagram of Fig. 12 and the one obtained in Ref. [79]. At the same time, the influence of disorder scattering on the Mott–Hubbard transition turns out to be highly nontrivial and qualitatively coincides overall with the results of Ref. [79]. The main distinction lies in the conservation of Hubbard bands in our results, even in the limit of high enough disorder, while in Ref. [79] they just disappear. Moreover, the phase coexistence region in Fig. 12 slowly widens with a disorder growth, instead of vanishing at some ‘critical’ point, as in the phase diagram of Ref. [79]. Coexistence region boundaries, which are defined by Mott insulating phase boundaries, obtained with an increase or decrease in U and represented by curves $U_{c1}(\Delta)$ and $U_{c2}(\Delta)$ in Fig. 12, can be obtained from the simple equation

$$\frac{U_{c1,c2}(\Delta)}{W_{\text{eff}}} = \frac{U_{c1,c2}}{W}, \quad (39)$$

where the effective bandwidth in the presence of disorder was calculated at $U = 0$ within the self-consistent Born approximation (28):

$$W_{\text{eff}} = W \sqrt{1 + 16 \frac{\Delta^2}{W^2}}. \quad (40)$$

Thus, the boundaries of the phase coexistence region, which also define the Mott insulating phase boundaries, are given by

$$U_{c1,c2}(\Delta) = U_{c1,c2} \sqrt{1 + 16 \frac{\Delta^2}{W^2}}. \quad (41)$$

Appropriate curves are plotted in Fig. 12 with dotted and solid lines. Phase transition points detected from the disappearance of a quasiparticle peak, as well as points following from qualitative changes in conductivity behavior, are shown in Fig. 12a by different symbols. These symbols demonstrate very good agreement with analytical results, supporting the choice of ratio (39) as a control parameter of Mott transition in the presence of disorder.

In Fig. 12b, we display the temperature dependence of Mott insulating phase boundaries $U_{c2}(\Delta)$ (squares) and the phase coexistence region $U_{c1}(\Delta)$ (circles).⁵ It is well known that in ‘pure’ DMFT without disorder, the coexistence region narrows with temperature growth and vanishes at some critical temperature T_c . In the DMFT + Σ approach, the disorder strengthening at zero temperature widens the coexistence region, and this behavior remains for finite temperatures. It is also seen that disorder growth leads to a practically linear growth (solid black line) in this critical temperature. Noteworthy also is the very weak temperature dependence of the coexistence region boundary $U_{c1}(\Delta)$.

3.2.2 Two-dimensional systems. According to the scaling theory of localization [95], the metallic state in two-dimensional (2D) systems does not exist: electrons are localized already at any infinitely weak disorder. Despite the fact that this prediction for 2D systems was made for noninteracting particles, later it was found that the weak interaction among electrons in the simplest case also favors localization [96]. In the early 1980s, experiments done on different 2D systems [97–99] mostly confirmed these predictions. Later on, however, some theoretical studies [75, 76] pointed out that in general this point of view is incorrect, since in the limits of weak disorder and large enough interaction 2D systems can have finite conductivity at zero temperature. The experimental discovery of metal–insulator transition in 2D weakly disordered systems at low carrier concentration, absent in the single-particle theory, stimulated a new field of theoretical

⁵ These results for different temperatures were calculated by N A Kuleeva.

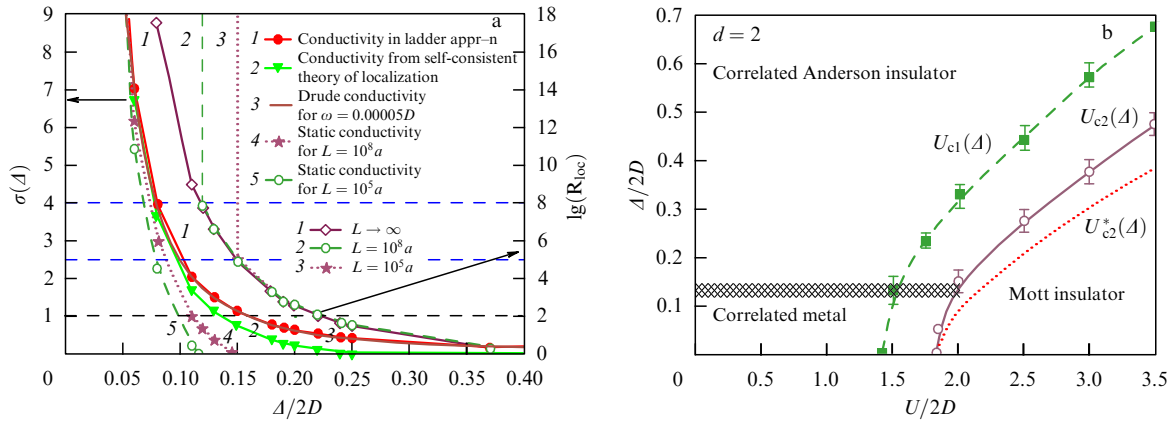


Figure 13. (a) Low finite frequency ($\omega = 0.00005D$) conductivity dependence on disorder strength A at $U/2D = 1$. Circles (curve 1) show the results of ladder approximation, triangles (curve 2) match the self-consistent theory of localization. Curve 3 (practically coinciding with the ladder approximation) is obtained from Drude formula (43). Curves 4 and 5 are the static conductivity of finite samples with sizes $L = 10^8 a$ and $L = 10^5 a$, respectively. On the right scale, localization radius logarithm is plotted versus disorder strength A : infinite-sized sample — curve 1, samples with finite sizes $L = 10^8 a$ and $L = 10^5 a$ — curves 2 and 3, respectively. (b) Phase diagram of the 2D paramagnetic Anderson–Hubbard model at zero temperature. Mott insulator region boundary $U_{c2}(A)$ and phase coexistence region boundary $U_{c1}(A)$ were obtained from density of states behavior. Hatched part exhibits the region of an effective Anderson metal–insulator transition in finite-sized systems. (Taken from Ref. [90].)

studies (see the introduction to this field in review papers [100, 101]).

In the DMFT + Σ approximation, as we shall see, the localization radius defined by Eqn (37) for infinite 2D system ($L \rightarrow \infty$) remains finite (even if exponentially large) for any infinitely weak disorder, signalling the absence of Anderson transition in such a system, similarly to the case of the conventional single-particle theory. However, as we shall demonstrate below, the localization radius in finite-sized systems diverges at some critical disorder which is defined by the characteristic size L of the system. Qualitatively, this critical disorder is determined by the condition that the localization radius of infinitely large system become comparable to characteristic sample size: $R_{\text{loc}}^{L \rightarrow \infty} \sim L$. Thus, Anderson transition in finite two-dimensional systems in fact exists, as does the metallic phase for a disorder strength below some critical value. In the following, by ‘correlated metal’ phase we imply precisely such a phase for finite 2D systems.

Below, we discuss the most relevant results of the DMFT + Σ computations for the 2D Anderson–Hubbard model at half-filling on a square lattice with model rectangular bare density of states with the bandwidth $W = 2D$:

$$N_0(\varepsilon) = \begin{cases} \frac{1}{2D}, & |\varepsilon| \leq D, \\ 0, & |\varepsilon| > D, \end{cases} \quad (42)$$

which qualitatively corresponds precisely to a 2D case.

Density of states and optical conductivity. Calculations demonstrated that the qualitative behavior of the density of states in 2D systems is completely analogous to that discussed above in the three-dimensional case. Some quantitative distinctions are due to the different model of the bare density of states (42), leading in particular to a larger (than in the three-dimensional case) critical Hubbard interaction $U_{c2} \approx 1.83W$, corresponding to Mott metal–insulator transition in the absence of disorder, and $U_{c1} \approx 1.42W$, bounding from below the region of coexistence of metallic and insulating phases. Similar to the three-dimensional model for $U > U_{c2}$ (i.e. for a Mott insulator without disorder), an increase in disorder strength leads to restoration of the

quasiparticle peak in the density of states. However, in this case such a behavior does not signal in general the transition to a correlated metal state—at least for infinitely large systems, we are dealing here with the correlated Anderson insulator.

Optical conductivity behavior in a wide frequency range is also qualitatively quite similar to that in the three-dimensional model. But for the infinite 2D model, zero-frequency conductivity always disappears (in the zero-temperature limit) and, in contrast to the $d = 3$ case [39], even at very weak disorder the peak in optical conductivity lies at a finite frequency. In the ladder approximation which does not contain localization corrections, the usual Drude peak is observed at zero frequency, and conductivity at $\omega = 0$ is finite.

More details concerning the results for the DOS and optical conductivity in the 2D model can be found in Ref. [90].

Localization radius and phase diagram of the 2D Anderson–Hubbard model at half-filling. In Fig. 13a, we illustrate the dependence of conductivity on disorder A at a finite but quite low frequency $\omega = 0.00005D$. Circles mark the results of ladder approximation, and triangles match the self-consistent theory of localization. Curve 3, qualitatively coinciding with the ladder approximation, was obtained from the classical Drude expression

$$\sigma(\omega) = \sigma(0) \frac{\gamma^2}{\gamma^2 + \omega^2}, \quad (43)$$

where static conductivity $\sigma(0) = e^2 N(0) D_0 \approx (e^2/\hbar) \varepsilon_F / (2\pi\gamma)$, $N(0)$ is the density of states at the Fermi level, and D_0 is the Drude diffusion coefficient. The impurity scattering rate was taken as $\gamma = \pi N(0) A^2 \approx (\pi/2D) A^2$. A significant contribution from localization corrections to conductivity at a finite frequency (a noticeable distinction of curve 2 from 1 and 3 curves) appears only when the conductivity reaches values on the order of minimal metallic conductivity $\sigma_0 = e^2/\hbar$ (whereon the conductivity is normalized in the figures). One should note that exactly in this range of disorder, as we shall see below, Anderson metal–insulator transition takes place (the localization radius diverges) in 2D systems of reasonable finite sizes.

Also in Fig. 13a, we demonstrate the dependences of the localization radius logarithm following from expression (37) (right scale) as a function of disorder strength: curve 1 is for an infinite sample, curves 2 and 3 are for finite-sized samples with $L = 10^8 a$ and $L = 10^5 a$, respectively. It is seen that the localization radius grows exponentially as disorder diminishes and remains finite in the infinite 2D system, where Anderson transition is absent. On the contrary, the localization radius for finite systems *diverges* at critical disorder determined by system size, demonstrating the existence of an effective Anderson transition. As can be seen from Fig. 13, the critical disorder is qualitatively defined by the condition that the localization radius of infinite system become comparable to the characteristic sample size $R_{\text{loc}}^{L \rightarrow \infty} \sim L$. It should be noted that the localization radius barely depends on U within our approach (in contrast, for example, to paper [81]), which leads to the independence of critical disorder of correlation strength U in 2D finite-sized systems. An analogous situation is also realized in three-dimensional systems [39]. In general, it is, of course, a drawback to our approximations.

Also in Fig. 13a, we plot the dependence of static conductivity on disorder strength in finite samples with sizes $L = 10^8 a$ and $L = 10^5 a$ (curves 4 and 5, respectively). In finite-sized systems with weak disorder, static conductivity is not zero (metal) and gradually falls with an increase in disorder strength. It becomes zero at critical disorder, where the localization radius also diverges in the sample of corresponding size. The static conductivity of finite-sized samples within our approximation barely depends on correlation strength U . A significant difference between static conductivity and conductivity at low finite frequency, observed in Fig. 13, is related to the above-mentioned exponential smallness of the frequency range with the localization behavior of conductivity.

Let us consider now the phase diagram of the 2D paramagnetic Anderson–Hubbard model at half-filling, obtained from DMFT + Σ calculated densities of states and from the analysis of localization radius behavior in finite-sized 2D systems. Such a phase diagram drawn in coordinates disorder (Δ)—correlation strength (U) is shown in the right part of Fig. 16.

The hatched stripe corresponds to the region of effective ‘metal’–Anderson insulator transition. The boundaries of this region are determined by divergence of localization radius in finite samples with characteristic sizes $L = 10^5 a$ (upper boundary) and $L = 10^8 a$ (lower boundary) (see Fig. 13a). It should be emphasized that a further increase in the system size, e.g. tenfold, up to $L = 10^9 a$, leads only to a quite insignificant drop in critical disorder. In other words, it slightly shifts down the lower boundary of the hatched stripe (Fig. 13b) — characteristic region of an effective Anderson transition in finite-sized systems.

Curve $U_{c2}(\Delta)$ computed from the density of states behavior defines the boundary of the Mott transition. The transition criteria are the disappearance of the central quasiparticle peak in the density of states $N(\varepsilon)$ together with gap opening on the Fermi level. Similarly to the three-dimensional model, a decrease in U starting from the insulating phase leads to the Mott transition at $U = U_{c1}(\Delta) < U_{c2}(\Delta)$ and a phase coexistence (hysteresis) region is observed in the phase diagram between curves $U_{c1}(\Delta)$ and $U_{c2}(\Delta)$ (Fig. 13b). In analogy with the three-dimensional case, we can guess that the ratio $U_{c1,c2}(\Delta)/W_{\text{eff}}(\Delta)$ between Hubbard interaction and effective bandwidth controls the

Mott metal–insulator transition and is a universal constant which does not depend on disorder, and obtain qualitative dependence $U_{c2}^*(\Delta)$ for the 2D model, which is fitted by the dotted curve in Fig. 13b. It is seen that, in contrast to the $d = 3$ case [39], the $U_{c2}(\Delta)$ dependence obtained from straightforward calculations of densities of states significantly differs from the qualitative $U_{c2}^*(\Delta)$ dependence. Apparently, it is related to the important change in the density-of-states lineshape (at $U = 0$) as disorder Δ grows, which is absent for the semielliptic band in the $d = 3$ case.

3.3 Singularities of electron dispersion in strongly correlated systems in DMFT and DMFT + Σ approaches

3.3.1 Cusps (‘kinks’) in electronic spectra. The electronic properties of crystalline solids are determined by single-particle and collective excitations of electron subsystem and their interactions with each other. These excitations are characterized by energy E and quasimomentum \mathbf{k} , which are related to each other via *dispersion* (spectrum) $E_{\mathbf{k}}$. Interaction between single-particle and collective modes can result in noticeable bends (cusps) of dispersion $E_{\mathbf{k}}$ — so-called ‘kinks’. The lineshape and energy position of these features characterize interactions in the many-body system. For example, kinks in the electronic dispersions experimentally found by ARPES in copper oxides, with energies 40–70 meV below the Fermi level, are evidence of electron–phonon [102–108] or electron–magnon (spin-fluctuation) interactions [109, 110].

At the same time, ARPES experiments detect kinks in electron dispersion for a number of different systems at essentially higher energies (up to 800 meV) [111–113]. The physical nature of these kinks remains unknown. Among other attempts to find an explanation for these electronic spectra anomalies, a novel purely electronic mechanism of kink formation was proposed by Byczuk et al. [114]. This mechanism is applicable to strongly correlated metals, where the spectral function contains well-developed Hubbard subbands, together with a central quasiparticle peak as, for example, in transition metal oxides. The energy location of these kinks apparently determines the range of applicability of the conventional Landau Fermi-liquid theory.

As is well known [115], interaction generally results in a finite lifetime of excitations in the system, so that $E_{\mathbf{k}}$ becomes a complex function. For electron systems with Coulomb interaction, the Landau Fermi-liquid theory proves the existence of weakly damped fermionic quasiparticles for low enough temperatures and in the narrow energy interval around the Fermi surface [115]. Beyond the Fermi-liquid mode, the concept of quasiparticles with well-defined dispersion is not, strictly speaking, applicable, since the quasiparticle lifetime is too short. However, ARPES experiments in recent years have convincingly shown the existence of essentially \mathbf{k} -dependent (though with rather broad maxima) single-particle spectral function quite far from the Fermi level, despite the fact that one cannot speak about well-defined quasiparticles at these energies. In this case, we understand as particle dispersion precisely this \mathbf{k} -dependence of spectral function maxima, which replaces the usual notion of a quasiparticle spectrum.

3.3.2 Kinks of purely electronic nature. Let us consider in more detail a new mechanism of kink formation in the electronic dispersion of strongly correlated systems, which does not assume an interaction of electrons with phonons or other excitations [114]. In order to understand the nature of this

mechanism, we shall examine at the beginning a weakly correlated system described by standard Fermi-liquid theory. Because of the large enough quasiparticle lifetime close to the Fermi level and the weakness of correlations, in the first approximation interaction leads to a simple renormalization of initial dispersion of (noninteracting) quasiparticles $\epsilon_{\mathbf{k}}$, which is replaced by $E_{\mathbf{k}} = Z_{\text{FL}}\epsilon_{\mathbf{k}}$, where Z_{FL} is the Fermi-liquid electron mass renormalization coefficient. This changes the slope of dispersion in the vicinity of the Fermi level, in contrast to a bare one. However, if we consider an electron with energy far away from the Fermi level, for weak interaction one can expect that its dispersion barely changes: $E_{\mathbf{k}} \approx \epsilon_{\mathbf{k}}$, though the damping here can already be pretty large. In this sense, one can say that electron–electron interaction by itself can result in the formation of bends (kinks) in the generalized dispersion (of the spectral function), and the position of such a kink on the energy scale is defined namely as energy, where a simple Fermi-liquid picture becomes inapplicable. However, in weakly correlated metals $Z_{\text{FL}} \lesssim 1$, so that the slope of $E_{\mathbf{k}}$ will change insignificantly, making such kinks hard to observe.

This picture may be distinctly different from that in strongly correlated systems where Z_{FL} can be much less than unity, thus making kinks more pronounced. Strong correlation interactions give rise to strong spectral weight redistribution within the single-particle spectral function due to the formation of Hubbard subbands. Moreover, as is well known, in strongly correlated metals there is also a quasiparticle peak which appears in proximity to the Fermi level, between Hubbard subbands. Below, it will be shown that ‘usual’ Fermi-liquid quasiparticles exist in such systems only in a very narrow vicinity of the Fermi level, while beyond the Fermi-liquid mode (but still ‘inside’ the quasiparticle peak) there exists some intermediate mode with dispersion $E_{\mathbf{k}} \approx Z_{\text{CP}}\epsilon_{\mathbf{k}}$, where renormalization factor Z_{CP} is determined by the central peak spectral weight and its value essentially differs from Z_{FL} . At these intermediate energies, which are much smaller than the interaction energy, electrons or holes strongly interact, and their dispersion differs from both the Fermi-liquid one and the one for noninteracting quasiparticles. In this energy range, we can speak about an ‘intermediately’ correlated situation, where $Z_{\text{FL}} < Z_{\text{CP}} < 1$. Consequently, at some energies $\pm\omega_*$ inside the quasiparticle peak, a transition from renormalization coefficient Z_{FL} to Z_{CP} takes place. That leads to an emergence of kinks in electronic dispersion, and the energy positions of these kinks are directly related to energy boundaries of the domain of applicability of the usual Fermi-liquid theory. Let us emphasize that this mechanism gives rise to kink formation without any additional interactions with phonons or other collective modes. The only necessary condition for such kink formation is the presence of strong electron–electron correlations in the system.

For a microscopic description of electronic kinks, let us consider the Hubbard model which will be analyzed in the framework of standard DMFT, using the numerical renormalization group (NRG) to solve the effective Anderson single-impurity problem. For simplicity, we consider the single-band Hubbard model at half-filling. The strongly correlated mode in the Hubbard model occurs when the interaction strength becomes on the order of bare bandwidth: $U \approx W$. Consider as an example the computed results given in Fig. 14. It is clearly visible that dispersion moves from the Fermi-liquid mode (line 1 in Fig. 14) to intermediate mode

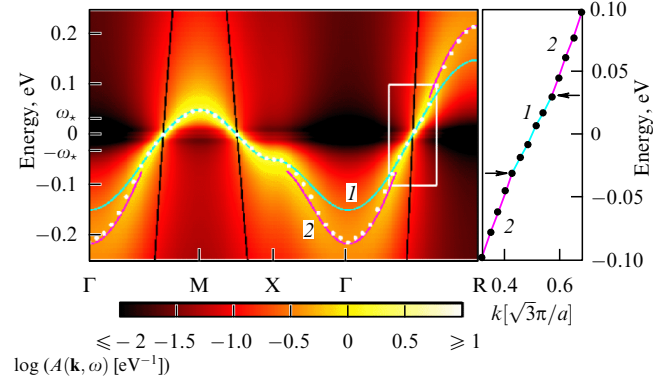


Figure 14. Cusps (kinks) in electronic dispersion $E_{\mathbf{k}}$ for strongly correlated systems. The logarithm of the DMFT spectral function $A(\mathbf{k}, \omega)$ is indicated in color gradations on the contour plot for the Hubbard model on a cubic lattice. The Hubbard interaction is $U = 3.5$ eV, bandwidth $W \approx 3.64$ eV, band filling $n = 1$, calculated value of Fermi-liquid renormalization $Z_{\text{FL}} = 0.086$, and temperature $T = 5$ K. Close to the Fermi level, the maxima of $A(\mathbf{k}, \omega)$ (white dots) correspond to renormalized dispersion $E_{\mathbf{k}} = Z_{\text{FL}}\epsilon_{\mathbf{k}}$ (line 1). For energies $|\omega| > \omega_*$ spectral function $A(\mathbf{k}, \omega)$ keeps its shape but with different renormalization $E_{\mathbf{k}} = Z_{\text{CP}}\epsilon_{\mathbf{k}} - c \text{sgn}(E_{\mathbf{k}})$ (line 2). Values of $\omega_* = 0.03$ eV, $Z_{\text{CP}} = 0.135$, and $c = 0.01$ eV are calculated in Ref. [114] from the values of Z_{FL} and $\epsilon_{\mathbf{k}}$ corresponding to the black line. The inset on the right shows in detail part of dispersion in the Γ -R direction, marked out with a white rectangle; kinks (cusps in dispersion) at energies $\pm\omega_*$ are pointed by arrows. Black lines display bare (noninteracting) quasiparticle spectra.

described above (line 2 in Fig. 14) with the formation of well-defined cusps in dispersion (kinks) at energies $\pm\omega_* = \pm 0.03$ eV. In some of the high-symmetry directions (e.g. around the X-point; see Fig. 14), the dispersion has quite a small slope in proximity to the Fermi level, making the kinks less pronounced.

Let us have a look at this situation from the point of view of single-particle Green function behavior. From general considerations it is clear that any cusps of dispersion caused by interaction appear because of the corresponding behavior of the self-energy or, more precisely, that of $\text{Re} \Sigma_{\mathbf{k}}(\omega)$. In the majority of real physical systems, \mathbf{k} -dependence of self-energy, apparently, is less important than ω -dependence and, thus, omitting \mathbf{k} -dependence of self-energy, $\Sigma_{\mathbf{k}}(\omega) = \Sigma(\omega)$, is, more or less, a good approximation. In the framework of DMFT, this statement is exact. The self-consistent expression for the self-energy of the Hubbard model within DMFT can be written out as

$$\Sigma(\omega) = \omega + \mu - \frac{1}{G(\omega)} - \Delta(G(\omega)), \quad (44)$$

where $G(\omega) = (1/N) \sum_{\mathbf{k}} G(\mathbf{k}, \omega)$ is the local (averaged over \mathbf{k}) Green function, and $\Delta(G)$ is the frequency-dependent hybridization function expressed via $G(\omega)$.⁶ The hybridization function describes quantum-mechanical coupling between an electron at a given site and other sites of the system.

In Fig. 15a, we plotted the frequency dependence of the spectral function (DOS) $A(\omega) = -\text{Im} G(\omega)/\pi$ calculated for the same model parameters as in Fig. 14 and demonstrating a typical three-peak structure. Corresponding real parts of the

⁶ In DMFT, $\Delta(G)$ is defined by $G(\omega) = G_0(\omega + \mu - \Sigma(\omega))$, i.e. $G_0(\Delta(G) + 1/G) = G$, where $G_0(\omega)$ is a noninteracting local Green function.

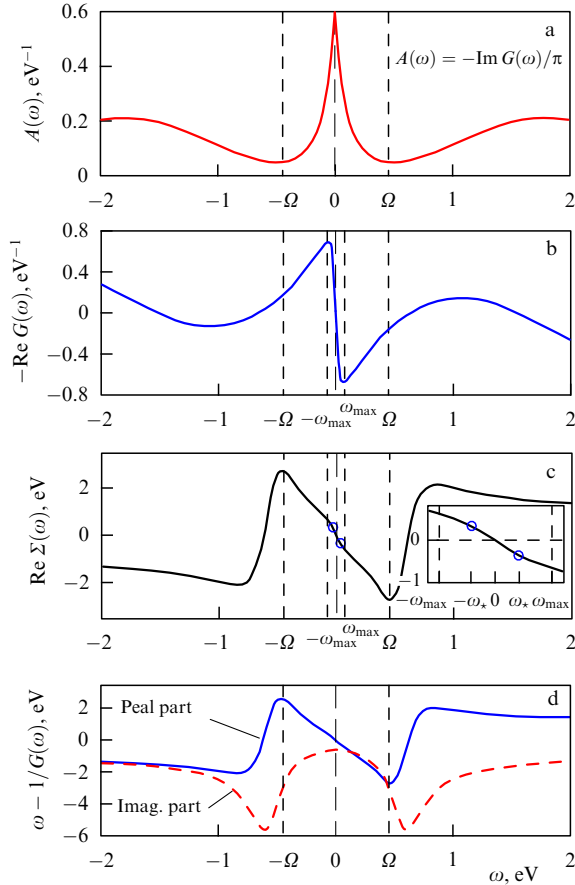


Figure 15. Green function characteristics for strongly correlated systems with parameters given in the caption to Fig. 14. (a) Three-peak structure of spectral function $A(\omega) = -\text{Im} G(\omega)/\pi$ with minima at energies $\pm\Omega = 0.45$ eV. (b) Real part of Green function with relative minima and maxima at energies $\pm\omega_{\text{max}}$ located ‘inside’ the quasiparticle peak. (c) Real part of self-energy with cusps at energies $\pm\omega_*$ (circles) situated at the points of maximal curvature of $\text{Re} G(\omega)$ ($\omega_* = 0.4\omega_{\text{max}} = 0.03$ eV). (d) Real part of $\omega - 1/G(\omega)$ (solid line) contributing to self-energy, which is linear, in general, in the energy interval $|\omega| < \Omega$. Change in energy dependence of $-\text{Re} G(\omega)$ at energies $\pm\omega_*$ defines the location of kinks (cusps) in electronic dispersion.

local Green function $G(\omega)$ and self-energy $\Sigma(\omega)$ are shown in Fig. 15b and Fig. 15c, respectively.

Kinks in $\text{Re} \Sigma(\omega)$ are directly related to the three-peak structure of integrated spectral function (DOS) $A(\omega)$ (its minima are located at energies $\pm\Omega$) and define some new, quite small energy scale. To this end, $\text{Re}[G(\omega)]$ should have maxima and minima on the energy interval $\pm\omega_{\text{max}}$, i.e. inside the central peak (Fig. 15b). In turn, this directly leads to kink formation in $\text{Re} \Sigma(\omega)$. Self-energy $\Sigma(\omega)$ comprises two contributions: $\omega + \mu - 1/G(\omega)$, and $-\Delta(G(\omega))$. Expression $\text{Re}[\omega + \mu - 1/G(\omega)]$ is linear within a quite large energy range $|\omega| < \Omega$ (Fig. 15d), while the quantity $-\text{Re}[\Delta(G(\omega))]$ is proportional to $-\text{Re}[G(\omega)]$, at least in the first order of corresponding momenta expansion, only on the small energy interval $|\omega| < \omega_{\text{max}}$. The sum of these two contributions gives rise to cusps in the real part of self-energy at energies $\pm\omega_*$, where $\omega_* = (\sqrt{2} - 1)\omega_{\text{max}}$. At these energies, $\text{Re}[G(\omega)]$ has maximal curvature (these points are marked by circles in Fig. 15c). Thus, the Fermi-liquid mode, where the slope of the real part of self-energy at the Fermi level is described by $\partial \text{Re} \Sigma(\omega)/\partial \omega = 1 - 1/Z_{\text{FL}}$, exists only

within a narrow part of the central peak, namely on the energy interval $|\omega| < \omega_*$. At higher (intermediate) energies, the slope of $\text{Re} \Sigma(\omega)$ will be given by the expression $\partial \text{Re} \Sigma(\omega)/\partial \omega = 1 - 1/Z_{\text{CP}}$. As a result, effective dispersion $E_{\mathbf{k}}$ will demonstrate kinks at energies $\pm\omega_*$.

This analysis also helps to understand why outside Fermi-liquid region $E_{\mathbf{k}}$ exhibits another value of renormalization of noninteracting electronic dispersion, given by Z_{CP} with small offset c . This behavior is determined by the magnitude of the main contribution $\omega + \mu - 1/G(\omega)$ to self-energy for energies $\omega_* < |\omega| < \Omega$, i.e. within the central peak of the DOS. Quantities ω_* , Z_{CP} , and c can be expressed via Z_{FL} and characteristics of the noninteracting electron density of states. One can derive the expression for $\omega_* = Z_{\text{FL}}(\sqrt{2} - 1)D$, where D is the half-width of the bare band (see details in paper [114]). If correlations are weak so that $Z_{\text{FL}} \lesssim 1$, the kink positions in $E_{\mathbf{k}}$ practically coincide with the edges of the bare electron band, which makes them almost unobservable. On the other hand, kink energy $\omega_*/D \propto Z_{\text{FL}}$ in the strongly correlated mode ($Z_{\text{FL}} \ll 1$) approaches the Fermi level inside the central peak whose width diminishes as $\Omega/D \propto \sqrt{Z_{\text{FL}}}$ with an increase in correlation strength [118].

These purely electronic kinks were first revealed in LDA + DMFT calculations for the SrVO₃ system [116]. The definition of energy scale ω_* contains only parameters of the initial band structure, which can be obtained (for realistic systems) via band structure calculations, together with Fermi-liquid mass renormalization $Z_{\text{FL}} = 1/(1 - \partial \text{Re} \Sigma(0)/\partial \omega) \equiv m/m^*$, which can be experimentally determined from specific heat or spin susceptibility measurements. Notably, in Ref. [117] it was shown that kinks of an electronic nature can cause corresponding cusps in the linear (in temperature) term of electronic specific heat of strongly correlated metals, which was, apparently, observed in the LiV₂O₄ heavy-fermion system.

3.3.3 Role of electron–phonon interaction. The material in the previous section inevitably brings us to the question about the relationship and mutual influence of kinks of an electronic nature and the ‘usual’ kinks in the electronic dispersion, induced by electron–phonon interaction. This is related to a more general problem of interference between strong electronic correlations and electron–phonon interactions. In fact, the history of such investigations is relatively long, and one of the most popular models of electron–phonon interaction in strongly correlated systems is the Hubbard–Holstein model. The Hubbard model describes local Coulomb interaction on a lattice [8–13]. On the other hand, the Holstein model describes the linear interaction of conduction electrons with *local* (Einstein) phonon modes [119]. Studies of the Hubbard–Holstein model were performed in the framework of conventional DMFT [5], in particular with the use of the numerical renormalization group (NRG) [24] as an ‘impurity solver’. Reducing the Hubbard–Holstein model to the Anderson–Holstein impurity problem was first performed by Hewson and Mayer [120]. These authors showed that by using NRG one can calculate the total electron–phonon contribution to self-energy, thus achieving a nonperturbative solution to the Hubbard–Holstein model, not only with respect to Hubbard interaction, but also with respect to electron–phonon interaction. It is worthy of note that the general structure of self-consistent DMFT equations in this approach is preserved.

Until recently, however, there had been no studies of strongly correlated electrons interacting with Debye pho-

nons, which is quite surprising in view of the rather wide discussion of the physics of kinks in electronic dispersion observed in ARPES experiments in high- T_c superconducting oxides [104]. The origin of these kinks is typically attributed to electron–phonon interaction [105]. The problem of kink formation in electronic dispersion caused by electron–phonon interaction in strongly correlated systems was briefly discussed in the framework of the Hubbard–Holstein model in papers [121, 122]. In this section, we overview DMFT + Σ results for the Hubbard model, adding interaction with Debye phonons under the assumption of the validity of the Migdal theorem (adiabatic approximation). This approximation is reasonable for electron–phonon coupling constant $\lambda < E_F/\omega_D \sim 10$, where E_F is the Fermi energy, and ω_D is the Debye frequency.

To consider electron–phonon interaction in a strongly correlated system, we introduce self-energy $\Sigma_{\mathbf{k}}(\varepsilon) = \Sigma_{\text{ph}}(\varepsilon, \mathbf{k})$ appearing in the usual Fröhlich model. According to the Migdal theorem, we can restrict ourselves in the adiabatic approximation to the simplest first-order contribution to $\Sigma_{\text{ph}}(\varepsilon, \mathbf{k})$. The main advantage of the adiabatic approximation is the possibility of neglecting any vertex corrections from electron–phonon interaction, which are small in regard to adiabatic parameter $\omega_D/E_F \ll 1$ [123].

In fact, $\Sigma_{\text{ph}}(\varepsilon, \mathbf{k})$ in this approximation exhibits only weak momentum dependence, which can be neglected, and we have to account only for the essential frequency dependence. Direct calculations (see, e.g., monograph [42]) in the case of the Debye phonon spectra $\omega_0(\mathbf{k}) = u|\mathbf{k}|$ for $|\mathbf{k}| < \omega_D/u$, where u is the speed of sound, give

$$\Sigma_{\text{ph}}(\varepsilon) = \frac{-ig^2}{4\omega_c^2} \int_{-\infty}^{+\infty} \frac{d\omega}{2\pi} \times \left\{ \omega_D^2 + \omega^2 \ln \left| \frac{\omega_D^2 - \omega^2}{\omega^2} \right| + i\pi\omega^2\theta(\omega_D^2 - \omega^2) \right\} I(\varepsilon + \omega), \quad (45)$$

where g is the usual electron–phonon interaction constant, and

$$I(\varepsilon) = \int_{-D}^{+D} d\xi \frac{N_0(\xi)}{E_\varepsilon - \xi},$$

$E_\varepsilon = \varepsilon - \Sigma(\varepsilon) - \Sigma_{\text{ph}}(\varepsilon)$, and $\omega_c = p_F u$ is the characteristic frequency of order the Debye one. In the case of semielliptic bare DOS $N_0(\varepsilon)$ with half-width D , one obtains $I(\varepsilon) = (2/D^2)(E_\varepsilon - \sqrt{E_\varepsilon^2 - D^2})$. It is convenient to introduce a dimensionless electron–phonon coupling constant which for this model can be written as [42]

$$\lambda = g^2 N_0(\varepsilon_F) \frac{\omega_D^2}{4\omega_c^2}. \quad (46)$$

To simplify calculations, we neglect renormalization of phonons because of electron–phonon interaction [42], assuming from here on that the phonon spectrum is fixed by experiment.

3.3.4 Electronic and phonon kinks within the DMFT + Σ approach. Let us focus on the most interesting DMFT + Σ results obtained in this model, referring the reader for details to Refs [124, 125]. Here, we present results addressing the interaction of electrons with Debye phonons (the results for Einstein phonons are analogous [125]).

A comparison of DMFT and DMFT + Σ_{ph} densities of states, with the latter involving electron–phonon interaction, for strong ($U/2D = 1.25$) and weak ($U/2D = 0.625$) Hubbard interactions is drawn in the upper and lower panels on the left side of Fig. 16. The dimensionless constant λ (46) exploited in these calculations was chosen to be $\lambda = 0.8$, and the Debye frequency $\omega_D = 0.125D$. In both cases, we observe some spectral weight transfer caused by electron–phonon interaction. At $U/2D = 1.25$ (Fig. 16a), we see a well-developed three-peak structure typical for strongly correlated metals. On the energy interval $\pm\omega_D$ around the Fermi level (which is measured up to zero energy in all figures) there is practically no difference in the shape of the quasiparticle peaks in the DOS obtained within DMFT and DMFT + Σ_{ph} approaches. But beyond this interval, the DMFT + Σ_{ph} quasiparticle peak becomes significantly wider because of the partial transfer of spectral weight from Hubbard bands. This broadening of the quasiparticle peak in DMFT + Σ_{ph} leads to a delay in the metal–insulator transition, as we shall see later.

In the case of $U/2D = 0.625$ (see Fig. 16b), no clearly distinguishable Hubbard bands are formed, and we observe

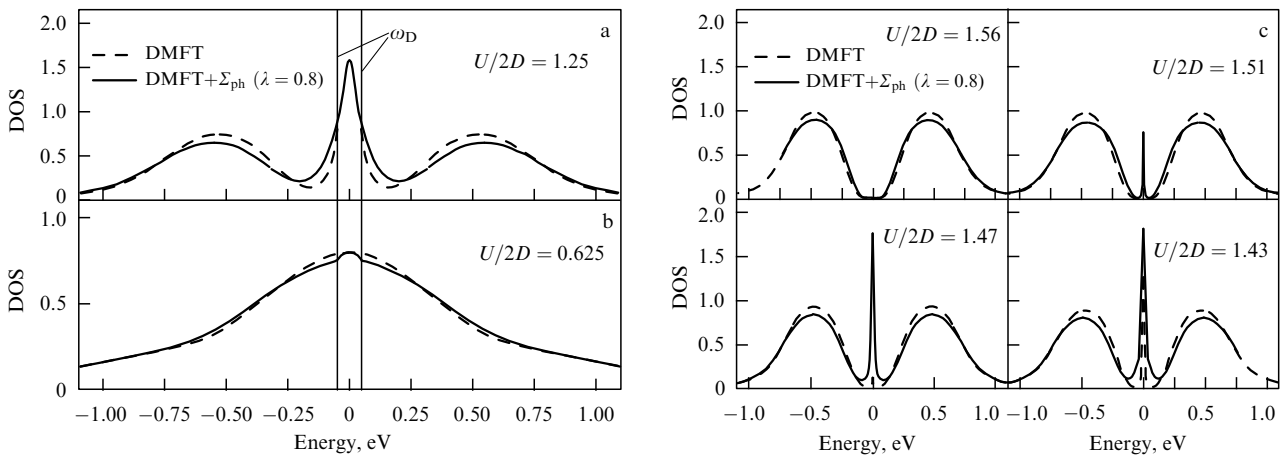


Figure 16. Comparison of conventional DMFT (dashed lines) and DMFT + Σ_{ph} (solid lines) densities of states. On the left side – for strong (upper panel, $U/2D = 1.25$) and weak (lower panel, $U/2D = 0.625$) Hubbard interactions. On the right side — evolution of densities of states in proximity to the metal–insulator transition. Dimensionless electron–phonon coupling constant is $\lambda = 0.8$ [124, 125].

only some side wings in the DOS. Redistribution of spectral weight in Fig. 16b is not very dramatic, despite a qualitative difference with the $U/2D = 1.25$ case (see Fig. 16a). The main distinction between DMFT and DMFT + Σ_{ph} results occurs here on the interval $\pm\omega_D$, where the formation of a ‘cap’ in the DOS is evidenced, due to electron–phonon interaction. The corresponding spectral weight ‘goes’ over to the energies around $\pm U$, where Hubbard bands start to form.

In Fig. 16c, we compare the behavior of densities of states in DMFT without phonons and in DMFT + Σ_{ph} for different values of the $U/2D$ parameter near the Mott–Hubbard metal–insulator transition. At $U/2D = 1.56$, both standard DMFT and DMFT + Σ_{ph} yield an insulating solution. However, there are some distinctions between these solutions. In DMFT + Σ_{ph} , the Hubbard bands are lower and wider than in DMFT, since additional (electron–phonon) interaction is included. With a decrease in U at $U/2D = 1.51$ and 1.47, we reveal that DMFT + Σ_{ph} results correspond to the metallic state (with a narrow quasiparticle peak at the Fermi level), while DMFT without phonons still furnishes the insulating solution. Only in proximity to $U/2D = 1.43$ do both DMFT and DMFT + Σ_{ph} results for DOS correspond to the metallic state. Thus, with an increase in U the finite strength of electron–phonon interaction slightly delays the Mott–Hubbard transition from the metallic to the insulating phase. This result is analogous to the one obtained in the Hubbard–Holstein model for weak electron–phonon coupling [126–128].

Therefore, moderate electron–phonon interaction brings to rather insignificant changes in the electron density of states both in correlated metal and in the Mott insulating state, only slightly delaying transition from metal to insulator with a growth in U .

Now we turn to the source of sharp slope changes of electron dispersion (kinks). It is well known that, in general, kinks are formed because of the interaction of electrons with bosonic modes. In electron–phonon interaction, the typical energy of the kink is around the Debye (or Einstein) frequency. We have shown in Section 3.3.1 that in strongly correlated metal, kinks of a purely electronic nature can arise [114]. The energy of such a kink for a semielliptical

bare DOS is $\omega^* = Z_{\text{FL}}(\sqrt{2} - 1)D$, where D is the half-width of the bare band, and $Z_{\text{FL}} = (1 - \partial \text{Re} \Sigma / \partial \varepsilon|_{\varepsilon=E_F})^{-1}$ is the Fermi-liquid renormalization factor. Roughly speaking, ω^* is defined by the half-width of the quasiparticle peak in the DOS.

A kink of an electronic nature is quite smooth, and its observation is rather difficult. DMFT + Σ_{ph} calculations give evidence that electronic kinks are hardly detectable against the background of phonon kinks, and the fine tuning of model parameters is necessary to pick them out. First of all, it is necessary to guarantee that $\omega_D \ll \omega^*$ (in other cases, smooth electronic kinks will be practically indiscernible against kinks from electron–phonon interaction). For $U/2D = 1$ and $U = 3.5$ eV, we have $\omega^* \sim 0.1D$, while the Debye frequency can be taken to be quite small, e.g. $\omega_D \sim 0.01D$. In order to make the phonon kink pronounced enough at such a relatively low Debye frequency, one needs to increase the electron–phonon coupling constant to $\lambda = 2.0$.

To demonstrate the possibility of the coexistence of both types of kinks in the spectra, let us consider the energy dispersion for a simple cubic lattice with nearest neighbors hopping only. It is most convenient to discuss the high-symmetry direction $\Gamma - (\pi, \pi, \pi)$ of the Brillouin zone [114]. In Fig. 17a, we show electronic dispersion along this direction close to the Fermi level. The line with the diamonds is the electronic spectrum of standard DMFT without phonons. Lines with circles present DMFT + Σ_{ph} results. Electronic and phonon kinks are marked by arrows. Generally, kinks in electronic dispersion due to electron–phonon interaction dominate for most typical model parameters, making purely electronic kink observation predicted in paper [114] quite difficult.

In conclusion, we give the picture of phonon kink evolution in the electronic spectrum depending on the strength of Hubbard interaction U . With an increase in the $U/2D$ ratio, Fermi velocity goes down and the kink position on the momentum axis shifts farther away from p_F , while the kink energy remains about ω_D . This behavior follows from direct DMFT + Σ_{ph} calculations [124, 125] and is shown in the right panel of Fig. 17. In the case of interaction with Einstein phonons, the results are quite analogous [125].

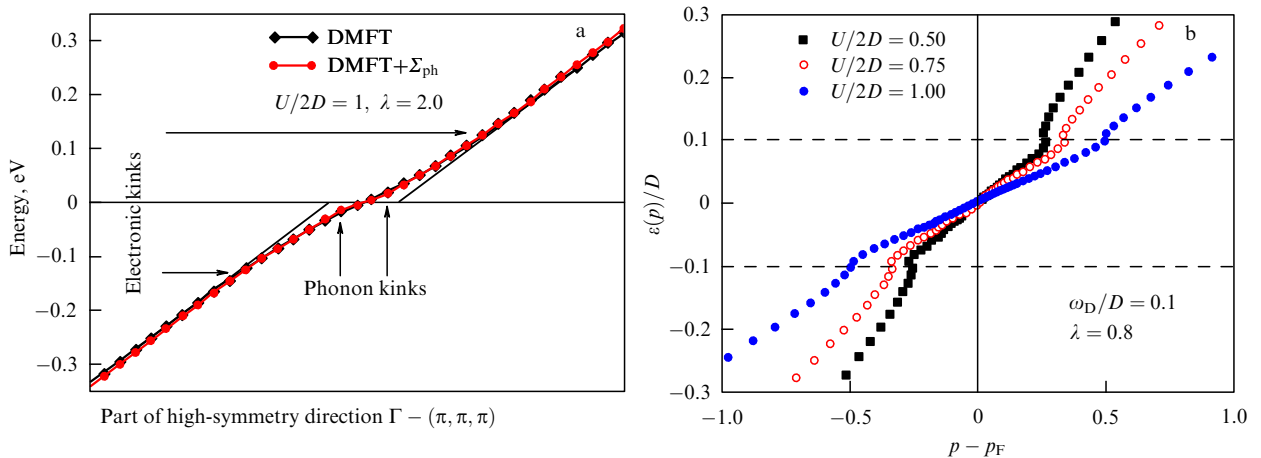


Figure 17. (a) Quasiparticle dispersion with kinks around the Fermi level, studied along $\Gamma - (\pi, \pi, \pi)$ high-symmetry direction in the Brillouin zone and obtained from ‘bare’ energy dispersion for the case of a simple cubic lattice with nearest neighbors hopping only: DMFT (curve with diamonds), and DMFT + Σ_{ph} (curve with circles) ($\lambda = 2$, $\omega_D = 0.01D$). (b) DMFT + Σ_{ph} phonon kink evolution for different strengths of Hubbard interaction $U/2D = 0.5, 0.75, 1.0$; $\lambda = 0.8$, and $\omega_D = 0.1D$ [124].

4. Electronic structure of real strongly correlated systems: LDA + DMFT and LDA + DMFT + Σ

At present, the most advanced *ab initio* (i.e. ideally without any fitting parameters) computational framework of electronic spectra of *realistic* strongly correlated systems is the LDA + DMFT method [2, 25]. The LDA band structure calculated by this method is used to obtain a ‘noninteracting’ starting Hamiltonian, while strong electron correlations are accounted afterwards within DMFT. In fact, the LDA + DMFT computational scheme combines two scientific areas: ‘realistic’ band structure calculations and traditional model approaches, which were essentially separated from each other before. Without DMFT, in just LDA there is no way to describe strongly correlated systems, while without LDA calculations, many-body methods cannot be material-specific. Below, we briefly discuss the basics of LDA + DMFT approach and its subsequent generalization to LDA + DMFT + Σ methods.

4.1 Density functional theory (DFT).

Local density approximation (LDA)

In the Born–Oppenheimer adiabatic approximation [129], neglecting relativistic effects, electronic properties in solid-state physics are described by the Hamiltonian

$$\begin{aligned} \hat{H} = & \sum_{\sigma} \int d^3r \hat{\Psi}^+(\mathbf{r}, \sigma) \left[-\frac{\hbar^2}{2m_e} \Delta + V_{\text{ion}}(\mathbf{r}) \right] \hat{\Psi}(\mathbf{r}, \sigma) \\ & + \frac{1}{2} \sum_{\sigma\sigma'} \int d^3r d^3r' \hat{\Psi}^+(\mathbf{r}, \sigma) \hat{\Psi}^+(\mathbf{r}', \sigma') V_{\text{ee}}(\mathbf{r} - \mathbf{r}') \\ & \times \hat{\Psi}(\mathbf{r}', \sigma') \hat{\Psi}(\mathbf{r}, \sigma). \end{aligned} \quad (47)$$

Here, $\hat{\Psi}^+(\mathbf{r}, \sigma)$ and $\hat{\Psi}(\mathbf{r}, \sigma)$ are the respective creation and annihilation operators of an electron with coordinate \mathbf{r} and spin σ , Δ is the Laplace operator, m_e is the electron mass, e is the electron charge, and

$$V_{\text{ion}}(\mathbf{r}) = -e^2 \sum_i \frac{Z_i}{|\mathbf{r} - \mathbf{R}_i|}, \quad V_{\text{ee}}(\mathbf{r} - \mathbf{r}') = \frac{e^2}{2} \sum_{\mathbf{r} \neq \mathbf{r}'} \frac{1}{|\mathbf{r} - \mathbf{r}'|} \quad (48)$$

denote a single-particle potential created by all ions i with charge eZ_i located at given positions \mathbf{R}_i , and electron–electron interaction.

Although the ‘first principle’ Hamiltonian (47) is easy to write down, it is impossible to solve the corresponding quantum-mechanical problem exactly. This is the reason to make substantial physical approximations. In particular, density functional theory (DFT) is based on the Hohenberg–Kohn theorem [130] (see also the review [131]), which asserts that ground-state energy is the unique functional of electron charge density, which is minimum for the equilibrium electron density in the ground state:

$$E[\rho] = E_{\text{kin}}[\rho] + E_{\text{ion}}[\rho] + E_{\text{Hartree}}[\rho] + E_{\text{xc}}[\rho], \quad (49)$$

where the Hartree energy $E_{\text{Hartree}}[\rho] = (1/2) \int d^3r' d^3r \times V_{\text{ee}}(\mathbf{r} - \mathbf{r}') \rho(\mathbf{r}') \rho(\mathbf{r})$ and the potential energy of ions $E_{\text{ion}}[\rho] = \int d^3r V_{\text{ion}}(\mathbf{r}) \rho(\mathbf{r})$ can be directly expressed via electron charge density. The term $E_{\text{kin}}[\rho]$ denotes the kinetic energy of electrons, and $E_{\text{xc}}[\rho]$ is an unknown, in general,

exchange-correlation term containing electron–electron interaction energy unaccounted for in the Hartree term. In fact, all complexities of the many-body problem are transferred into the computation of $E_{\text{xc}}[\rho]$.

In practice, instead of minimization of $E[\rho]$ over ρ , minimization is usually performed over some set of orthonormal basis functions φ_i related to ρ through the expression

$$\rho(\mathbf{r}) = \sum_{i=1}^N |\varphi_i(\mathbf{r})|^2. \quad (50)$$

Introducing arbitrary Lagrange parameters ε_i and requiring the fulfillment of the equality

$$\frac{\delta}{\delta \varphi_i(\mathbf{r})} \left\{ E[\rho] + \varepsilon_i \left[1 - \int d^3r' |\varphi_i(\mathbf{r}')|^2 \right] \right\} = 0, \quad (51)$$

one gets Kohn–Shem equations [132, 133]

$$\begin{aligned} \left[-\frac{\hbar^2}{2m_e} \Delta + V_{\text{ion}}(\mathbf{r}) + \int d^3r' V_{\text{ee}}(\mathbf{r} - \mathbf{r}') \rho(\mathbf{r}') + \frac{\delta E_{\text{xc}}[\rho]}{\delta \rho(\mathbf{r})} \right] \\ \times \varphi_i(\mathbf{r}) = \varepsilon_i \varphi_i(\mathbf{r}). \end{aligned} \quad (52)$$

Formally, this equation coincides with the stationary single-particle Schrödinger equation. Electron kinetic energy corresponding to charge density of the ground state is now given by the expression

$$E_{\text{kin}}[\rho_{\text{min}}] = - \sum_{i=1}^N \left\langle \varphi_i \left| \frac{\hbar^2 \Delta}{2m_e} \right| \varphi_i \right\rangle, \quad (53)$$

where φ_i are the self-consistent (spin-degenerate) solutions of equations (50) and (52), corresponding to the smallest single-particle energy ε_i [134].

The most common way to calculate $E_{\text{xc}}[\rho]$ is to use the *local density approximation* (LDA). It approximates the functional $E_{\text{xc}}[\rho]$ by the local charge density functional

$$E_{\text{xc}}[\rho] \rightarrow \int d^3r \rho(\mathbf{r}) \varepsilon_{\text{xc}}^{\text{LDA}}(\rho(\mathbf{r})). \quad (54)$$

The explicit expression for $\varepsilon_{\text{xc}}^{\text{LDA}}(\rho(\mathbf{r}))$ can be found in the framework of different models, e.g. from a numerical analysis of the ‘jellium’ model (electron gas against a positive ionic homogeneous background) [135].

In fact, LDA approximation corresponds to the replacement of the Hamiltonian (47) by the expression

$$\begin{aligned} \hat{H}_{\text{LDA}} = & \sum_{\sigma} \int d^3r \hat{\Psi}^+(\mathbf{r}, \sigma) \left[-\frac{\hbar^2}{2m_e} \Delta + V_{\text{ion}}(\mathbf{r}) \right. \\ & \left. + \int d^3r' \rho(\mathbf{r}') V_{\text{ee}}(\mathbf{r} - \mathbf{r}') + \frac{\delta E_{\text{xc}}^{\text{LDA}}[\rho]}{\delta \rho(\mathbf{r})} \right] \hat{\Psi}(\mathbf{r}, \sigma). \end{aligned} \quad (55)$$

In practical calculations, electron field operators are expanded in terms of a some set of atomic-like functions (basis set) Φ_{ilm} (i denotes lattice site, l is the orbital quantum number, and m is the magnetic quantum number). In this representation, one has

$$\hat{\Psi}^+(\mathbf{r}, \sigma) = \sum_{ilm} \hat{c}_{ilm}^{\dagger} \Phi_{ilm}(\mathbf{r}), \quad (56)$$

and the Hamiltonian (55) is rewritten as

$$\hat{H}_{\text{LDA}} = \sum_{ilm, j'l'm', \sigma} (\delta_{ilm, j'l'm'} \varepsilon_{ilm} \hat{n}_{ilm}^{\sigma} + t_{ilm, j'l'm'} \hat{c}_{ilm}^{\sigma \dagger} \hat{c}_{j'l'm'}^{\sigma}). \quad (57)$$

Here $\hat{n}_{ilm}^{\sigma} = \hat{c}_{ilm}^{\sigma \dagger} \hat{c}_{ilm}^{\sigma}$ is the electron density operator on a given orbital, while matrix elements

$$t_{ilm, j'l'm'} = \left\langle \Phi_{ilm} \left| -\frac{\hbar^2 \Delta}{2m_e} + V_{\text{ion}}(\mathbf{r}) + \int d^3 r' \rho(\mathbf{r}') V_{\text{ee}}(\mathbf{r} - \mathbf{r}') + \frac{\delta E_{\text{xc}}^{\text{LDA}}[\rho]}{\delta \rho(\mathbf{r})} \right| \Phi_{j'l'm'} \right\rangle \quad (58)$$

in case of $ilm \neq j'l'm'$ define effective hopping integrals, and single-particle eigenenergies ε_{ilm} are given by corresponding diagonal expressions in case of identical indices. At this point purely analytical work ends and numerical calculations follow within the chosen basis set, e.g. linearized muffin-tin orbitals (LMTO). Specific expressions for matrix elements (58) within the LMTO basis are presented in Refs [136, 137].

4.2 LDA + DMFT computational scheme

For strongly correlated materials, the onsite Coulomb interaction between d- and f-electrons is of primary importance, since this contribution to interaction energy is the largest one. The largest nonlocal contribution follows from the density–density type interaction involving nearest neighbors, where the main contribution comes from the Hartree term (see Refs [138, 139] and [140]), which was already taken into account in the LDA. Moreover, some part of the exchange–correlation interactions are taken into account in the LDA via effective single-electron potential $\delta E_{\text{xc}}^{\text{LDA}}[\rho]/\delta \rho(\mathbf{r})$.

In order to take into consideration strong local Coulomb interaction, one should supplement Hamiltonian (57) with approximate local Coulomb matrix comprising the most important parameters only [25]: onsite intraband Coulomb repulsion U , exchange interaction J , and interorbital Coulomb repulsion U' acting on different electronic orbitals of the same site i_d , where an atom with a partially filled d -shell resides (l —orbital quantum number, m —magnetic quantum number, and σ —spin index):

$$\begin{aligned} \hat{H} = & \hat{H}_{\text{LDA}} + U \sum_m \sum_{i=i_d, l=l_d} \hat{n}_{ilm \uparrow} \hat{n}_{ilm \downarrow} \\ & + \sum_{i=i_d, l=l_d} \sum_{m \neq m'} \sum_{\sigma \sigma'} (U' - \delta_{\sigma \sigma'} J) \hat{n}_{ilm \sigma} \hat{n}_{ilm' \sigma'} \\ & - \sum_{i=i_d, l=l_d} \sum_{m \sigma} \Delta \varepsilon_d \hat{n}_{ilm \sigma}. \end{aligned} \quad (59)$$

Here, for simplicity, only density–density type interactions are left, and so-called Kanamori parametrization is applied, when for the same orbitals ($m = m'$) the direct Coulomb interaction is taken as U , while for different orbitals ($m \neq m'$) this interaction is replaced by U' . Because of the rotational invariance of the single-atom problem, one has $U' = U - 2J$, and the exchange interaction parameter does not depend on the orbital index and is equal to J .

Moreover, the last term involving the quantity $\Delta \varepsilon_d$ was added to formula (59) (the so-called double-counting correction), which should correct for double counting of interaction contributions, as some part of local Coulomb interaction has

already been included in \hat{H}_{LDA} . The general microscopic expression for $\Delta \varepsilon_d$ via U and ρ is unknown. However, there are several qualitative recipes to determine the value of $\Delta \varepsilon_d$, which are employed in different modern LDA + DMFT calculations (a detailed discussion can be found in Refs [141, 142]). The simplest physical assumption lies in the fact that the Coulomb interaction energy can be written down within the DFT as

$$E_{\text{DFT}} = \frac{1}{2} \bar{U} n_d (n_d - 1), \quad (60)$$

where n_d is the total number of electrons in the d -shell, and \bar{U} is the average Coulomb interaction (here, we assume averaging over all orbital pairs $m\sigma, m'\sigma'$ at a given site). Thus, $\Delta \varepsilon_d$ is taken as

$$\Delta \varepsilon_d = \frac{\partial E_{\text{DFT}}}{\partial n_d} = \bar{U} \left(n_d - \frac{1}{2} \right). \quad (61)$$

The interaction parameters U , J , and U' can be obtained from the averaged Coulomb interaction \bar{U} and Hund exchange parameter J . The averaged interaction \bar{U} is related to the U and U' Coulomb parameters via the following relation:

$$\bar{U} = \frac{U + (N_{\text{orb}} - 1) U' + (N_{\text{orb}} - 1)(U' - J)}{2N_{\text{orb}} - 1}, \quad (62)$$

where N_{orb} is the number of interacting orbitals. Since U and U' are not independent parameters, \bar{U} and J are sufficient for determining U [29–31, 143].

Different methods have been developed for microscopic calculations of averaged Coulomb interaction, such as constrained LDA (CLDA) [144] or constrained RPA (CRPA) [145, 146]. Generalizations to calculating the Hund exchange parameter also exist. Unfortunately, there are rather large discrepancies between the values of parameters obtained with these methods. Particularly, the quantity \bar{U} appears to be strongly dependent on the basis set used (e.g. in the problem of screening the long-range part of the Coulomb interaction). It is clear that the introduction of all these essentially model parameters takes us quite far away from the ‘first principle’ ideal, though it is the best one can do at the moment to calculate the electronic band structure of solids comprising transition metal atoms, where electron–electron interactions play the crucial role. In that sense, it is probably more correct to speak about ‘modeling’ of the electronic structure of such systems.

Matrix elements of the ‘noninteracting’ Hamiltonian $H_{\text{LDA}}^0(\mathbf{k})$ in the reciprocal space can be calculated numerically at every point of the Brillouin zone, then the integrals over the Brillouin zone are usually calculated with the tetrahedron method [147]. In relatively simple band dispersions, where the analytical expression for $H_{\text{LDA}}^0(\mathbf{k})$ dependence on \mathbf{k} can be written explicitly, the hopping integrals can be found from LDA by projecting on corresponding Wannier functions [148–151]. Matrix elements of this Hamiltonian, i.e. single-particle LDA energies without local Coulomb interaction, can be written in the following way:

$$\begin{aligned} (H_{\text{LDA}}^0(\mathbf{k}))_{qlm, q'l'm'} = & (H_{\text{LDA}}(\mathbf{k}))_{qlm, q'l'm'} \\ & - \delta_{qlm, q'l'm'} \delta_{ql, q_d l_d} \Delta \varepsilon_d n_d, \end{aligned} \quad (63)$$

where q is the atomic index in the unit cell.

The essence of the next step is to use in the DMFT or DMFT+ Σ loop (see Section 2.1) the local lattice Green function (5) determined by the momentum-integrated Dyson's equation of the form

$$G_{qlm,q'l'm'}(\omega) = \frac{1}{V_B} \int d\mathbf{k} [\omega \delta_{qlm,q'l'm'} - (H_{\text{LDA}}^0(\mathbf{k}))_{qlm,q'l'm'} + \delta_{ql,q'a'l'a} \Sigma_{qlm,q'l'm'}(\omega)]^{-1}, \quad (64)$$

where $[\dots]^{-1}$ denotes the inverse matrix with indices $n(=qlm)$, $n'(=q'l'm')$, while the integration is performed over the Brillouin zone of the volume V_B .

A significant simplification of computations can be achieved for the case of cubic lattice symmetry, where the crystal field strongly splits d-orbitals into threefold degenerate t_{2g} states and twofold degenerate e_g states nonmixed with the former. In this special case, both the Green function and the self-energy become diagonal with respect to orbital and spin indices, thus reducing the problem, in fact, to single-band. Then, the calculation of the local Green function of the lattice problem can be performed as energy integration with the use of unperturbed densities of states, which allows avoiding tedious integration over the Brillouin zone in expression (64) and writing

$$G(\omega) = G^0(\omega - \Sigma(\omega)) = \int d\epsilon \frac{N^0(\epsilon)}{\omega - \Sigma(\omega) - \epsilon}. \quad (65)$$

In this case, double-counting correction $\Delta\epsilon_d$ reduces to an immaterial shift of the chemical potential, and its particular mathematical form is irrelevant altogether.

4.3 Examples of LDA + DMFT calculations

4.3.1 Cubic perovskites CaVO_3 and SrVO_3 . In this section, we consider examples of some LDA + DMFT calculations of electronic band structure of realistic compounds with strong enough electronic correlations. Transition metal oxides are an ideal testing area to study electronic correlations in solids. Among these materials, cubic perovskites have the simplest crystal structure and, therefore, can be viewed as a starting point for understanding the electronic properties of more complex systems. Usually, 3d states in such materials form comparatively narrow bands with the width $W \sim 2-3$ eV, leading to strong electron-electron Coulomb correlations.

The modern stage of experimental investigations of spectral and transport properties of strongly correlated 3d¹ transition metal oxides started from the work of Fujimori et al. [152]. The authors, apparently for the first time, discovered a strongly pronounced lower Hubbard band in photoemission spectra, which could not be explained by standard methods of band structure calculations. In many earlier studies [153–156] devoted to the properties of the series of $\text{Sr}_{1-x}\text{Ca}_x\text{VO}_3$ compounds with different values of x , rather controversial results were reported. Whereas the thermodynamic characteristics (the Sommerfeld coefficient, electrical resistance, and magnetic susceptibility) appeared to be more or less x -independent, spectroscopic measurement data changed rather strongly as a system transformed from $x=0$ (SrVO_3) to $x=1$ (CaVO_3). These data indicated a transition from a strongly correlated metal (SrVO_3) to a practically ideal insulator (CaVO_3), with the concentration range $x \rightarrow 1$ in $\text{Sr}_{1-x}\text{Ca}_x\text{VO}_3$ being the boundary of the Mott-Hubbard transition.

An analysis of this problem was performed using high penetration depth photoemission experiments by Maiti et al. [157], and similar experiments with high-resolution photoemission by Sekiyama et al. [158]. In particular, it was shown in the last study that: (1) the surface preparation technique is very important (the cleavage method is preferable), and (2) the energy of an X-ray incident beam should be high enough to provide the penetration depth of several unit cells. At the same time, high instrumental resolution should be guaranteed (about 100 meV in the work [158]). Such an improvement in photoemission spectroscopy methods led to the observation of almost identical spectra for $\text{Sr}(\text{Ca})\text{VO}_3$ [157, 158], demonstrating agreement of spectroscopic and thermodynamic measurements. The results of these experiments also agree with earlier 1s X-ray absorption spectra (XAS) obtained by Inoue et al. [159], which differ only for energies slightly above the Fermi level, in contrast, say, to bremsstrahlung isochromat spectroscopy (BIS) data [156]. In the framework of a single-band Hubbard model with a neglect of orbital structure of vanadium 3d shell, Rozenberg et al. [160] modelled $\text{Sr}_{1-x}\text{Ca}_x\text{VO}_3$ spectra obtained by high penetration depth photoemission spectroscopy [157] using adjustable parameters. Later on, it was demonstrated [158] that the data from Ref. [157] contained quite a significant surface contribution.

Below, we present results of LDA + DMFT(QMC) calculations performed without any adjustable parameters, both for the spectral function and density of electronic states in cubic SrVO_3 and in orthorhombic CaVO_3 perovskites. According to these, both systems in their ground states are strongly correlated metals, which are quite far away from the metal-insulator transition boundary. Despite the significantly smaller V–O–V bond angle in CaVO_3 , the photoemission spectra of both systems are very similar and their quasiparticle peaks are almost identical. The results obtained agreed very well with modern high-resolution bulk sensitive photoemission data mentioned above. In the spectral function of SrVO_3 , obtained from LDA + DMFT(QMC) calculations, kinks of a purely electronic nature at about 200 meV were observed, and later these kinks were found experimentally.

Results of LDA + DMFT calculations. First of all, from the LDA-calculated band structure we extract single-electron Hamiltonian \hat{H}_{LDA}^0 with the subtracted averaged Coulomb interaction (to avoid its double counting) [25]. Supplementing \hat{H}_{LDA}^0 with local Coulomb interaction between electrons, we obtain Hamiltonian (59) for the material of interest. Since the CaVO_3 symmetry is close to cubic, it is possible to simplify the calculations and use integration over band with the LDA density of states $N^0(\epsilon)$, instead of integration over the Brillouin zone. In Hamiltonian (59), local intraorbital and interorbital repulsions and exchange interactions are taken into account explicitly as U , U' , and J . The strengths of these interactions for SrVO_3 were calculated by the constrained LDA method [144] with e_g states included in the screening [161]. The obtained strength of average Coulomb interaction is $\bar{U} = 3.55$ eV ($\bar{U} = U'$ for t_{2g} orbitals [26, 143]) and $J = 1.0$ eV. Intraorbital Coulomb repulsion U is fixed by rotational invariance: $U = U' + 2J = 5.55$ eV. \bar{U} was not calculated for CaVO_3 , since the standard procedure of calculating Coulomb interaction parameters between two t_{2g} electrons screened by e_g states is not applicable to the distorted crystal structure, where the e_g and t_{2g} orbitals are not separated by symmetry. On the other hand, it is known

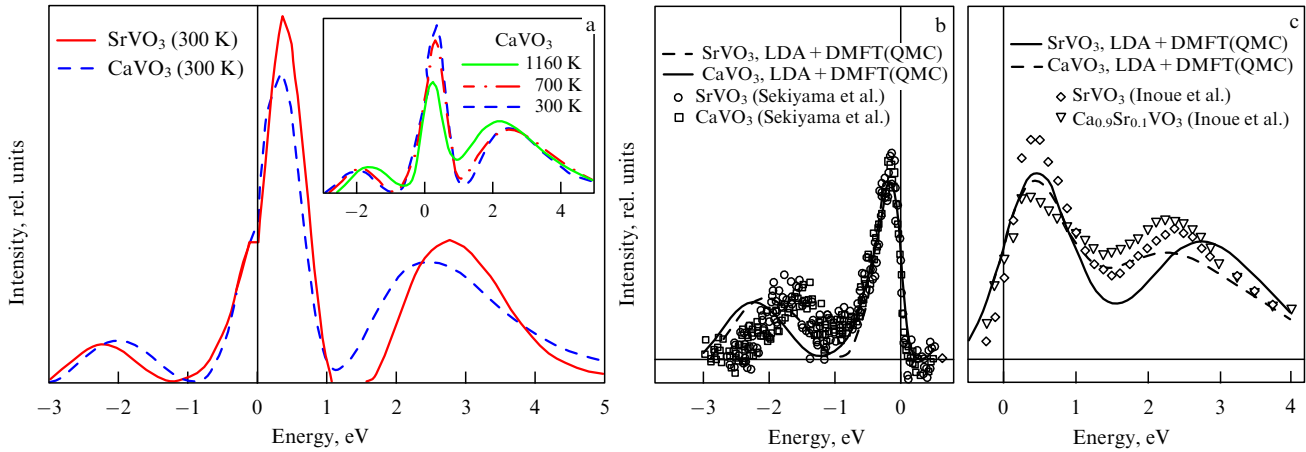


Figure 18. (a) LDA + DMFT(QMC) spectra for SrVO₃ (solid line) and CaVO₃ (dashed line) at $T = 300$ K (inset: temperature influence on CaVO₃ spectrum lineshape). (b, c) Comparison of calculated (without adjustable parameters) LDA + DMFT(QMC) spectra for SrVO₃ (solid line) and CaVO₃ (dashed line) with high-resolution bulk sensitive photoemission data (SrVO₃—circles, and CaVO₃—squares) [158] (b) and 1s-XAS spectra: (SrVO₃—diamonds, and Ca_{0.9}Sr_{0.1}VO₃—triangles) [159] (c). Horizontal line indicates experimental background.

that changes in *local* Coulomb interaction are usually much smaller than changes in density of states, which, as shown above, are weakly dependent on V–O–V bond angle. This means that \bar{U} for CaVO₃ should be practically the same as for SrVO₃. Correspondingly, the values of $\bar{U} = 3.55$ eV and $J = 1.0$ eV were used for both SrVO₃ and CaVO₃. These values agree with other band structure calculations for vanadium compounds [161] and with the experimental data [162].

Further computations with Hamiltonian (59) were performed in the framework of DMFT by the quantum Monte Carlo (QMC) method [18–22] as an impurity solver. In QMC, the Green function was obtained for the imaginary time (or at Matsubara frequencies) and then continued to the real time (frequency) by the maximum entropy method [163]. In LDA + DMFT(QMC) spectra calculated for SrVO₃ and CaVO₃ and shown in Fig. 18a, we observe manifestations of correlation effects, such as formation of lower Hubbard bands near -2.0 eV and upper Hubbard bands at about 2.5 eV with well-developed quasiparticle peaks on the Fermi level. Thus, both SrVO₃ and CaVO₃ constitute strongly correlated metals. The difference in bare bandwidths (about 4%) is only responsible for a small additional spectral weight transfer from the quasiparticle peak to Hubbard bands and for slight changes in Hubbard band positions. Obviously, both systems are not close to the Mott–Hubbard metal–insulator transition. Many-body densities of states for both systems (see Fig. 18) are rather alike but not identical. Indeed, SrVO₃ is a bit less correlated than CaVO₃, in agreement with the difference between their LDA bandwidths. The inset to Fig. 18a gives evidence that temperature influence on the spectrum is small for $T \lesssim 700$ K.

In Fig. 18b, LDA + DMFT(QMC) spectra (calculated at $T = 300$ K, then multiplied by the Fermi function at an experimental temperature of 20 K and broadened with a Gaussian 0.1 eV wide to mimic experimental resolution [158]) are compared with experimental photoemission data after subtraction of oxygen and surface contributions. Notably, the height and the width of these spectra are almost the same in SrVO₃ and CaVO₃ (with a bit of difference above the Fermi level). On the other hand, the positions of lower Hubbard bands differ quite markedly. This variance might occur

because of subtraction of the (estimated) oxygen contribution which can delete part of the 3d spectral weight below -2 eV, or due to uncertainties in \bar{U} calculations.

In Fig. 18c we draw a comparison of calculated results with XAS data. Finite lifetime effects for holes are taken into account by broadening the theoretical spectra with a Lorentzian 0.2 eV wide [164], then multiplication by the inverse Fermi function (at $T = 80$ K), and further broadening with a Gaussian exhibiting an experimental resolution of 0.36 eV. The general agreement of weights and positions of the quasiparticle band and upper Hubbard t_{2g} band is good, including tendencies associated with the transition from SrVO₃ to CaVO₃ (Ca_{0.9}Sr_{0.1}VO₃ in the experiment). For CaVO₃, the quasiparticle spectral peak weight is a bit less than in the experiment. In contrast to single-band Hubbard model calculations, LDA + DMFT approach accounts for peculiarities of the concrete systems and reproduces the strong asymmetry of the spectra close to the Fermi energy, including relative weights and bandwidths. These results (see Fig. 18) allow a different interpretation of XAS data than in Ref. [159], where the maximum at 2.5 eV was associated with the e_g band and not with the upper Hubbard t_{2g} band. Small differences between quasiparticle peaks (see Fig. 18) lead to various values of effective masses: $m^*/m_0 = 2.1$ for SrVO₃, and $m^*/m_0 = 2.4$ for CaVO₃. These theoretical predictions agree with $m^*/m_0 = 2–3$ for SrVO₃ and CaVO₃ obtained from de Haas–van Alphen experiments and available thermodynamic data [153–155, 165]. Notice that the effective mass for CaVO₃, determined from optical experiments, is slightly larger: $m^*/m_0 = 3.9$ [162].

4.3.2 Kinks in the SrVO₃ spectral function. Let us consider in more details LDA + DMFT(QMC) results obtained for spectral function $A(\mathbf{k}, \omega)$ of SrVO₃ in Ref. [116]. Owing to ideal cubic lattice symmetry, the matrix of self-energy $\Sigma(\omega)$ is diagonal, and all diagonal elements are the same for all t_{2g} orbitals. The spectral function is defined by the imaginary part of Green function $\text{Im} G(\mathbf{k}, \omega)$, i.e. in fact by self-energy $\Sigma(\omega)$ on the real axis. This self-energy was calculated by numerical solution of Dyson’s equation for the known interacting and bare Green functions, as described in the Appendix to Ref. [151].

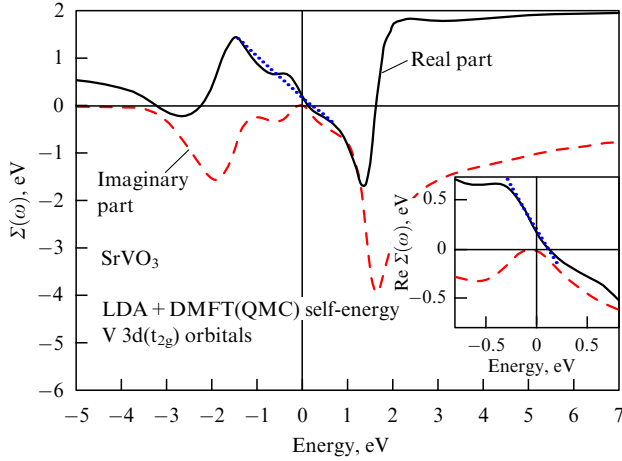


Figure 19. Real (black solid line) and imaginary (grey dashed line) parts of self-energy $\Sigma(\omega)$ obtained from the LDA + DMFT(QMC) calculations for V 3d (t_{2g}) orbitals in SrVO₃ [116]. In the inset to the figure, the self-energy in the vicinity of the Fermi level is shown in more detail. Dotted straight lines give the slope of $\text{Re } \Sigma(\omega)$ far away and close to the Fermi level.

In Fig. 19, this self-energy $\Sigma(\omega)$ is plotted as a function of real frequencies. It is essentially asymmetric with respect to the Fermi level, as could be assumed from the asymmetry of the LDA density of states and band filling equal to 1/6. At energies $\omega \sim \pm 1.5$ eV, the real part of self-energy has extrema, corresponding to the transition region from the quasiparticle peak to the lower and upper Hubbard bands. Two extrema in the imaginary part of the self-energy, coinciding with $\text{Re } \Sigma(\omega)$ zeros,⁷ determine the energy positions of the lower and upper Hubbard bands (see Fig. 18a).

The asymmetric quasiparticle peak in the density of states is situated in the energy range from -0.8 to 1.4 eV (Fig. 18a). It is evident that imaginary part of self-energy, $\text{Im } \Sigma(\omega)$, is sufficiently low at these energies, while its real part can be roughly approximated with the dashed straight line drawn in Fig. 19. The slope of this line determines quasiparticle mass renormalization $Z = m^*/m = 1 - \partial \text{Re } \Sigma(\omega) / \partial \omega|_{\omega=0} = 1.9$. Such a Z value agrees with that obtained from primary QMC data at Matsubara frequencies: $m^*/m = 1 - \text{Im } \Sigma(\omega_0) / \omega_0 \approx 2$, where ω_0 is the ‘zeroth’ Matsubara frequency. This value of renormalization is in agreement with the value of $m^*/m = 2.2$ from the studies [166, 167], as well as with the experimental estimate from ARPES data [168].

In the inset to Fig. 19 it is seen that Fermi-liquid behavior of self-energy [$\text{Im } \Sigma(\omega) \sim -\omega^2$, together with $\text{Re } \Sigma(\omega) \sim -\omega$] is evidenced only on the interval from -0.2 to 0.15 eV. The slope of $\text{Re } \Sigma(\omega)$ in immediate proximity to the Fermi level is steeper than in the wider energy interval (see dashed straight line in Fig. 19). Thus, the Fermi-liquid mass renormalization value is larger than $m^*/m = 1.9$ and is equal to $m_{\text{low } E}^*/m = 3$ (dotted straight line in the inset to Fig. 19). At the edges of the Fermi-liquid mode, sharp bends in $\text{Re } \Sigma(\omega)$ at energies $\omega = \pm 0.25$ eV are seen. As the border of the Fermi-liquid mode we can consider energies whereat the imaginary part of self-energy starts to differ from the

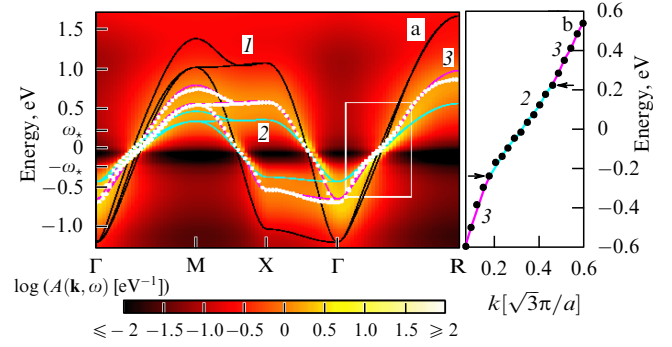


Figure 20. (a) Kinks in the dispersion relation $E_{n\mathbf{k}}$ (white dots) for SrVO₃ obtained from LDA + DMFT calculations. Lines 1—LDA band structure $\epsilon_{n\mathbf{k}}$; lines 2—LDA bands renormalized with the Fermi-liquid mass renormalization factor; lines 3—band structure within the intermediate mode. (b) Kinks are marked with arrows, which correspond to the area within the white rectangle in figure a.

square-law dependence $\text{Im } \Sigma(\omega) \sim -\omega^2$, which, in turn, leads to real part of self-energy deviating from the linear dependence $\text{Re } \Sigma(\omega) \sim -\omega$ following from the Kramers–Kronig relation. Deviation from the square behavior of $\text{Im } \Sigma$ at energies on the order of $\omega = \pm 0.25$ eV immediately gives rise to appearing cusps in $\text{Re } \Sigma(\omega)$.

If the self-energy on the real axis is known, one can compute the spectral function $A(\mathbf{k}, \omega)$ and the quasiparticle dispersion determined by the momentum dependence of its maxima. In Fig. 20, we display the map of the spectral density obtained for SrVO₃ in Ref. [116]. In this multiband system (with degenerate bands), further analysis is similar to that for the single-band case of Section 3.3.2. White dots denote $E_{n\mathbf{k}}$ dispersion curves obtained from LDA + DMFT calculations for SrVO₃. In the narrow vicinity of the Fermi level, they coincide with the LDA band structure $\epsilon_{n\mathbf{k}}$ (lines 1) renormalized with Fermi-liquid factor $Z_{\text{FL}} = 0.35$, so that $E_{n\mathbf{k}} = Z_{\text{FL}} \epsilon_{n\mathbf{k}}$ (lines 2). Outside the Fermi-liquid region, dispersion curves correspond to the LDA band structure with a different renormalization factor: $E_{n\mathbf{k}} = Z_{\text{CP}} \epsilon_{n\mathbf{k}} + c_{\pm}$ (lines 3), where $Z_{\text{CP}} = 0.64$, $c_{+} = 0.086$ eV, and $c_{-} = 0.13$ eV. Along high-symmetry Γ –M and Γ –R directions in the Brillouin zone, the transition between these two modes leads to the formation of kinks in the effective dispersions at energies $\omega_{\star} = 0.22$ eV and $-\omega_{\star} = -0.24$ eV. These kinks are marked with arrows in Fig. 20b, which corresponds to the area surrounded by the white rectangle in the main part of the figure. On the contour plot of spectral function $A(\mathbf{k}, \omega)$, it is seen that the spectral function in the energy region sufficiently far away from the Fermi level keeps an explicit \mathbf{k} -dependence, despite a pretty large damping value, replacing the traditional band structure picture for systems with strong electron–electron correlations.

Kinks of an electronic nature were discovered in this system in ARPES experiments [168] in the Γ –M direction at energies on the order of 0.25 eV, which agrees quite well with the above-given results of LDA + DMFT(QMC) calculations.

4.4 Electronic structure of copper oxides in the pseudogap state: LDA + DMFT + Σ

The pseudogap state— as already pointed out above— is one of the main anomalies in the normal (nonsuperconducting) state of high- T_c cuprates, and it is thought that

⁷ Here, we recall that the real part of Green function is connected with the imaginary part of self-energy via the Kramers–Kronig relation [115].

clarification of its physical nature is the key point to understanding the high-temperature superconductivity mechanism [55, 56, 169]. The most powerful tool to investigate this state in recent years has been angular-resolved photoemission spectroscopy (ARPES). During the last ten years there has been remarkable progress in this area related to significant growth of ARPES resolution, both in energy and in momentum spaces [170–173]. The Fermi surface shape, quasiparticle dispersion and damping, and even self-energy profile can be directly restored from ARPES data [170–173]. These allowed studying in detail formation of the pseudogap, shadow bands, quite unusual phenomena of Fermi arc formation, and interlayer hybridization effects (bilayer splitting) in double-layer systems [170–173], as well as determining qualitative distinctions between electron- and hole-doped cuprates [170–173]. The purpose of the theory is to explain all these peculiarities, and this problem is much more complicated by the presence of rather strong electronic correlations, typical for these systems and making doubtful the standard band theory and Fermi-liquid approach.

In this section, we shall demonstrate that an account of AFM short-range order fluctuations is, in principle, enough for describing a number of ARPES experiments on real systems. To this end, we make use of the LDA + DMFT + Σ hybrid computational scheme [174–179]. On the one hand, this scheme inherits all the advantages of LDA + DMFT approach [25–31], i.e. the combination of single-electron first-principle density functional theory in the local density approximation (DFT/LDA) [132, 133, 180, 181] with dynamical mean-field theory for strongly correlated electrons [3–5, 7, 14]. On the other hand, such a hybrid scheme allows considering nonlocal correlations by the introduction of momentum-dependent self-energy, while the usual self-consistent set of DMFT equations is preserved [35–37]. To solve effectively the single-impurity problem of DMFT in the works described below, we employed the numerical renormalization group (NRG) method [23, 24].

Such a computational scheme works very well in describing the electronic properties of high- T_c cuprates in the normal (underdoped) state. First, all material-specific model parameters of a physically relevant Cu-3d_{x²-y²} orbital can be obtained from LDA calculations. Second, stoichiometric (nondoped) cuprates are antiferromagnetic Mott insulators with $U \gg W$ (U is the local Coulomb interaction, and W is the conduction bandwidth), so that correlation effects in them are very important. At finite doping level (at least up to optimal doping), cuprates are typical strongly correlated metals, and the DMFT stage of the computational scheme allows one to account for strong electronic correlations. Finally, to study the ‘antiferromagnetic scenario’ of pseudogap formation, we introduce into the standard LDA + DMFT scenario the \mathbf{k} -dependent self-energy $\Sigma_{\mathbf{k}}$ describing nonlocal correlations induced by (quasi)static Heisenberg spin fluctuations of AFM short-range order [58–60].

In the framework of the LDA + DMFT + Σ approach, we performed calculations for a series of high-temperature superconductors: hole-doped Bi₂Sr₂CaCu₂O_{8- δ} (Bi2212) [174] and La_{2- x} Sr _{x} CuO₄ (LSCO) [175], and also electron-doped Nd_{2- x} Ce _{x} CuO₄ (NCCO) [176, 177] and Pr_{2- x} Ce _{x} CuO₄ (PCCO) [178]. LDA + DMFT + Σ calculated results for Fermi surfaces and spectral functions can be compared with ARPES data for quasiparticle bands and experimental Fermi surface maps.

The crystal structures of Bi2212 [174], NCCO [176, 177], and PCCO [178] have tetragonal symmetry with the space group $I4/mmm$, while LSCO has a distorted orthorhombic structure $Bmab$ [175]. Crystallographic data employed in LDA + DMFT + Σ calculations are presented in more detail in Refs [174–179].

It is well known that the physical properties of cuprates are determined in many respects by the quasi-two-dimensionality of their electronic properties. From this point of view, the main interest is focused on electronic states in the CuO₂ plane, where we are dealing with partially filled antibonding Cu-3d_{x²-y²} orbitals with dispersion crossing the Fermi level. In the tight-binding approximation, this dispersion has the following form

$$\begin{aligned} \varepsilon(\mathbf{k}) = & -2t(\cos k_x a + \cos k_y a) - 4t' \cos k_x a \cos k_y a \\ & - 2t''(\cos 2k_x a + \cos 2k_y a) \\ & - 2t'''(\cos k_x a \cos 2k_y a + \cos 2k_x a \cos k_y a). \end{aligned} \quad (66)$$

Here, t , t' , t'' , t''' are Cu–Cu transfer integrals in the first four coordination spheres in the CuO₂ plane, and a is the lattice constant. The values of these effective transfer integrals calculated in the framework of the linearized muffin-tin orbitals (LMTO) method [136, 137] and subsequent use of Wannier functions obtained within the N -th-order LMTO (NMTO) method of Refs [148–150] are listed in Table 1. In what follows, we shall exploit the LDA-calculated effective antibonding Cu-3d_{x²-y²} band as a ‘bare’ one in LDA + DMFT + Σ computations.

In double-layer systems, e.g. in Bi2212, hopping between two neighboring planes is also important. In the tight-binding approximation, an expression for the corresponding interlayer dispersion derived in Ref. [182] has the form

$$t_{\perp}(\mathbf{k}) = \frac{t_{\perp}}{4} (\cos k_x a - \cos k_y a)^2. \quad (67)$$

The values of t_{\perp} are given in Table 1. Consideration of interlayer hopping and ‘bilayer splitting’ effects requires a certain generalization of LDA + DMFT + Σ computational scheme [174].

To perform DMFT calculations, one should also calculate the strength of onsite Coulomb interaction. The values of this interaction U for the effective Cu-3d_{x²-y²} orbital, obtained within the constrained LDA method [144], are also given in Table 1.

To account for AFM spin fluctuations, we employed the two-dimensional model of the pseudogap state [58–60], generalized for DMFT + Σ calculations [35, 37]. Additional external \mathbf{k} -dependent self-energy $\Sigma_{\mathbf{k}}$ [35, 37] describes non-

Table 1. Calculated model energy parameters (in eV) and experimental correlation length ξ .

Compound	t	t'	t''	t'''	t_{\perp}	U	A	ξ
Bi2212	-0.627	0.133	0.061	-0.015	0.083	1.51	0.21	10 a
NCCO	-0.44	0.153	0.063	-0.010	—	1.10	0.36	50 a
PCCO	-0.438	0.156	0.098	—	—	1.10	0.275	50 a
LSCO	-0.476	0.077	-0.025	-0.015	—	1.10	0.21	10 a

Note. First four Cu–Cu transfer integrals in the CuO₂ plane are t , t' , t'' , and t''' ; effective interlayer transfer integral is t_{\perp} ; local Coulomb interaction is U , and pseudogap amplitude is A .

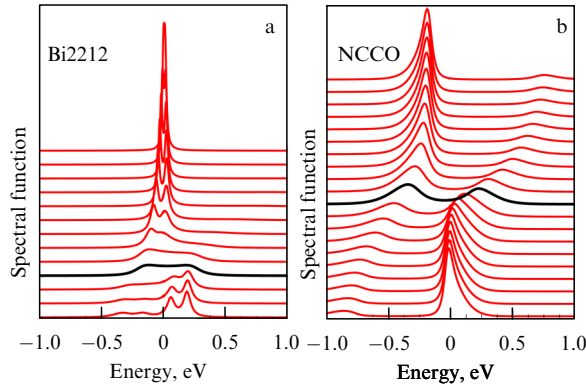


Figure 21. LDA + DMFT + Σ spectral functions for Bi2212 (a) and NCCO (b) along the bare Fermi surface in $1/8$ of the Brillouin zone. The dark lines correspond to the hot spots [176, 177].

local correlations caused by (quasi)static⁸ AFM spin fluctuations.

To specify $\Sigma_{\mathbf{k}}$, it is necessary to know two important parameters: the pseudogap amplitude Δ giving the energy scale of fluctuating SDW, and the correlation length ξ . The values of Δ were calculated as described in Refs [35, 37, 174]. The values of the correlation length were taken in accordance with those produced in neutron scattering experiments for NCCO [183, 184] and LSCO [185]. The values of Δ and ξ used for all systems under consideration are also listed in Table 1. To solve effectively the Anderson single-impurity problem in DMFT, we applied the numerical renormalization group method ([23, 24]). The temperature in DMFT(NRG) calculations was chosen equal to 0.011 eV, and electron or hole concentration (doping level) amounted to 15%.

LDA + DMFT + Σ calculations produced a clear picture of hot spots behavior in the spectral function and on maps of the Fermi surfaces for electron-doped systems [176–178], while for hole-doped systems only Fermi arcs arose [174, 175].

Figure 21 gives LDA + DMFT + Σ results for spectral functions calculated along $1/8$ of the bare Fermi surface, from the nodal point on the diagonal of the Brillouin zone (upper curve) to the antinodal point at the boundary of the zone (lower curve). Results for Bi2212 are shown in the left panel of the figure, and for NCCO in the right panel. For both systems, quasiparticles are well defined in the nodal direction—a sharp peak of the spectral function situated practically on the Fermi level is clearly seen. As one moves to the antinodal point, quasiparticle damping grows, reaching a maximum at the hot spot (dark curve), and the peak of spectral density moves away from the Fermi level. This behavior is in complete agreement with the results of Refs [186, 187] (for a comparison with experiment, see Refs [176, 177]). From the LDA + DMFT + Σ results given in Fig. 21, it is directly seen that antinodal states in Bi2212 are formed by the low-energy edge of the pseudogap,⁹ while in NCCO by the high-energy edge. For Bi2212, we also observe bilayer

⁸ The quasistatic approximation for AFM fluctuations necessarily restricts this approach to rather high temperatures (and energies not very close to the Fermi level) [58–60]. Thus, we cannot in fact judge, for instance, the nature of low-temperature (low-energy) damping, which is determined entirely by dynamical (inelastic) scattering processes.

⁹ It is especially distinctly visible for the case of smaller correlation length $\xi = 5a$ considered in Ref. [174].

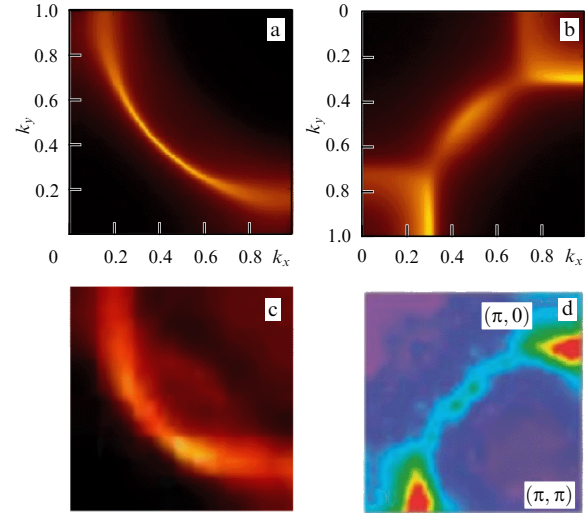


Figure 22. LDA + DMFT + Σ Fermi surface maps obtained in Refs [176, 177] for Bi2212 (a) and NCCO (b) compounds in a fourth of the Brillouin zone (k_x, k_y are given in units of π/a). Experimental Fermi surfaces for Bi2212 (c) [188] and NCCO (d) [186].

splitting of the quasiparticle peak, which is related to the presence of two CuO_2 planes in the unit cell.

The hot spots for NCCO are located closer to the Brillouin zone diagonal [176, 177]. This can be seen from the dark lines in Fig. 21, which correspond to the hot spots. Moreover, the correlation length in NCCO is much larger than in Bi2212. Thus, quasiparticles again are rather well defined for NCCO (in contrast to Bi2212) in the antinodal direction. For Bi2212, on the contrary, scattering near the Brillouin zone boundaries is strong everywhere, and instead of hot spots we observe quite strong ‘destruction’ of the Fermi surface close to these boundaries. Qualitatively the same picture is also observed in LSCO.

LDA + DMFT + Σ Fermi surface maps in the quarter of the Brillouin zone for Bi2212 are presented in Fig. 22a, and for NCCO in Fig. 22b. In Bi2212, we observe strong destruction of the Fermi surface by scattering on pseudogap fluctuations in proximity to the Brillouin zone boundaries.¹⁰ In NCCO, in contrast, the Fermi surface is almost completely restored close to the Brillouin zone boundaries. On the other hand, the Fermi arc around the nodal direction in Bi2212 is pronounced rather clearly, while in NCCO it is noticeably smeared. This is another consequence of the fact that hot spots in NCCO are located closer to the Brillouin zone diagonal. A bit larger value of the pseudogap amplitude Δ also favors the stronger smearing of Fermi arcs in NCCO. Noteworthy also is the appearance of the shadow Fermi surface which is much more intensive in NCCO.

Qualitatively the same Fermi surfaces were discovered experimentally in real Bi [188] and Nd [186] systems (see Fig. 22c, d). Thus, the distinction of Fermi surface maps for these systems is related mainly to the distinction of the band structure parameters for these materials. In particular, LDA Fermi surfaces of NCCO are more bent, and hot spots appear to be rather far from the Brillouin zone boundaries; consequently, the Fermi surface in the vicinity of these

¹⁰ Analogous behavior in entire accordance with ARPES results is also realized in another hole-doped system—LSCO. The LDA + DMFT + Σ calculations for this system were performed in Ref. [175].

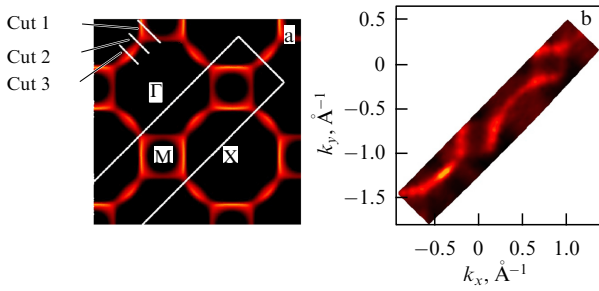


Figure 23. Fermi surface map for PCCO. (a) Results of LDA + DMFT + Σ calculations. The white rectangle in panel (a) shows the part of reciprocal space where ARPES measurements (panel b) were done. The lower left corner coincides with the X-point ($\pi/a, 0$) of the Brillouin zone [178].

boundaries barely feels scattering by AFM fluctuations. In Bi2212, the LDA Fermi surface comes in rather close to the Brillouin zone boundaries in proximity to the $(\pi/a, 0)$ point, so that hot spots are also close to this point. Thus, they are more ‘smeared’ in Bi2212 by strong pseudogap scattering near the $(\pi/a, 0)$ point and are almost not observed. Hot spots in NCCO are more vivid also because of the much larger correlation length of fluctuations.

No less clear results were obtained in LDA + DMFT + Σ calculations and ARPES experiments for PCCO in Ref. [178]. Figure 23 displays a PCCO Fermi surface map (panel (a) — LDA + DMFT + Σ results, and panel (b) — experimental ARPES data). The Fermi surface is clearly distinguishable here only near first Brillouin zone boundaries and around the $(\pi/a/2, \pi/a/2)$ point (Fermi arc). Again, as in NCCO, we observe destruction of the Fermi surface in hot spots located at the intersection of the Fermi surface and its AFM shadow ‘replica’. This destruction of the Fermi surface is due to the strong electron scattering by AFM spin (pseudogap) fluctuations. The shadow Fermi surface becomes observable, as happens in the case of AFM doubling of the lattice period. However, since there is no long-range order in the underdoped region in which we are interested, this shadow Fermi surface is strongly eroded. The PCCO Fermi surface is very similar to that observed in $\text{Nd}_{2-x}\text{Ce}_x\text{CuO}_4$ (NCCO) compound, which belongs to the same family of superconductors [176, 177, 186].

Let us compare (see Fig. 24) theoretical (upper panel) and experimental (lower panel) quasiparticle dispersions along the most characteristic cuts of the Fermi surface shown in Fig. 23. Theoretical data are multiplied by the Fermi function at a temperature of 30 K and convoluted (in energy) with a Gaussian distribution to simulate the experimental resolution.

Cut 1 crosses the quasiparticle and shadow Fermi surfaces near the Brillouin zone boundary. Correspondingly, it is possible to detect here a fork-like structure formed by a suppressed shadow band and much better defined by a quasiparticle band. This structure corresponds to the origin of formation of the Fermi surface cylinder around the $(\pi/a, 0)$ point. Cut 2 passes exactly through the hot spot. Here, we see a strong suppression of the quasiparticle band near the Fermi level. Finally, cut 3 crosses the Fermi arc and we can see a fairly well-defined quasiparticle band. However, the low-intensity shadow band is also present. In the case of the presence of long-range AFM order and a full doubling of the period, the Fermi surface and its shadow form a closed ‘pocket’ of the Fermi surface around the $(\pi/2a, \pi/2a)$ point,

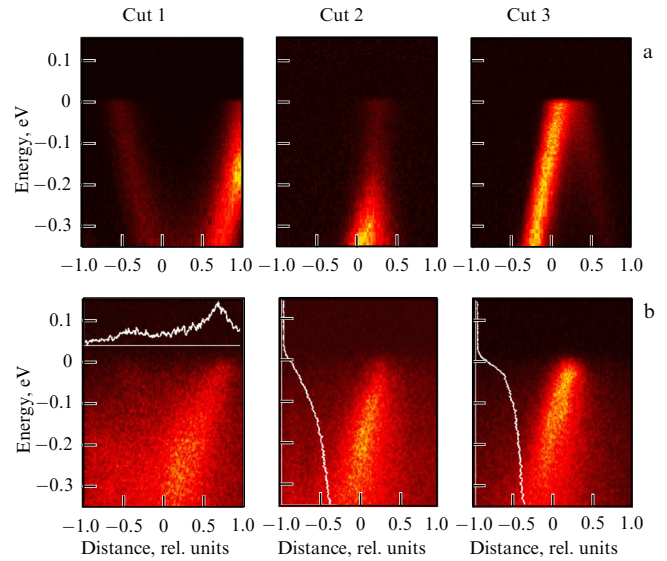


Figure 24. Momentum–energy distributions of intensity for characteristic cuts of the Brillouin zone plotted in Fig. 23 (upper panels — theoretical data, lower panels — experimental photoemission intensities). For cut 1, we show the momentum distribution curve (MDC) integrated over the energy window 60 meV in width around the Fermi level. Analogous MDC for cut 2 (through the hot spot) shows ARPES intensity suppression compared with MDC for cut 3 which is located quite far away from the hot spot [176, 177].

while in the present case a part of the pocket formed by the shadow band is strongly smeared. One can see a good agreement between calculated and experimental data. As already noted, two-particle properties within the LDA + DMFT + Σ framework can also be calculated [38], which allowed investigating the optical conductivity of Bi and Nd cuprates [176, 177], and also demonstrating significant differences in the effects of pseudogap fluctuations. In particular, we observe in the optical conductivity of NCCO, in qualitative agreement with experiment [189], a characteristic pseudogap dip and a smooth maximum due to absorption through the pseudogap at frequencies $\sim 2\Delta$. However, the characteristic pseudogap structure in optical conductivity of Bi2212 hardly occurs, either in theory or in experiment [190], which is related to sufficiently small values of Δ and the fluctuation correlation length in this system.

Let us summarize some of our conclusions. For all the systems studied, LDA + DMFT + Σ calculations give evidence that Fermi-liquid behavior persists only rather far away from hot spots (nodal direction), and destruction of the Fermi surface is observed near the hot spots. This destruction is due to strong scattering of correlated electrons on short-range order AFM (pseudogap) fluctuations. A comparison of ARPES data and LDA + DMFT + Σ calculated results points to the existence of quite distinct hot spots in the behavior of both the spectral density and maps of the Fermi surface in electron-doped systems, in contrast to hole-doped systems, where we only observe a strong destruction of the Fermi surface near the Brillouin zone boundaries and Fermi arcs around its diagonals.

There are several reasons for this distinction: (1) hot spots in electron-doped systems are located closer to the center of the Brillouin zone; (2) the correlation length of AFM fluctuations in electron-doped systems is longer, and (3) the width of the pseudogap in electron-doped systems is also

larger than in hole-doped ones. The experimental and theoretical results discussed above clearly confirm the AFM scenario of the formation of a pseudogap in both hole-doped [174, 175] and electron-doped [176–178] cuprates.

5. Conclusions

In this review, we discussed the DMFT + Σ generalization of the standard dynamical mean-field theory (DMFT), which allows us to include nonlocal correlations or additional (relative to the Hubbard one) interactions (theoretically of any type), while remaining within the single-impurity picture of DMFT and retaining the same set of self-consistent DMFT equations. The basic approximation of this method relies on the neglect of interference contributions from DMFT diagrams and additional interactions included in the analysis. Precisely this (strictly speaking not completely controllable) approximation allows preserving the overall structure of DMFT equations, which permits solving DMFT + Σ equations with the well-developed methods used in the standard DMFT. It should be emphasized that the self-consistent account of additional interactions at every step of the DMFT loop leads to a rather complicated procedure equivalent to the summation of infinite classes of diagrams.

The proposed approach proved to be versatile enough to be applied to a number of problems in systems with strong electron correlations—from a semiphenomenological account of nonlocal short-range order pseudogap fluctuations to the self-consistent framework for the metal–insulator transition in the disordered Anderson–Hubbard model and account of the electron–phonon interaction effects in the electronic spectra of strongly correlated systems. A salient feature of the DMFT + Σ approach is the possibility of studying, along with one-particle characteristics, the two-particle properties, i.e., in principle, any kind of response functions (optical conductivity, magnetic susceptibility, charge screening, etc.). The universality of the method allows one to hope for its successful application to solving a number of future problems.

Discussing all the problems of interest, one should keep in mind that similar in many respects physical results can also be obtained with more sophisticated approaches, using these or other methods of direct numerical simulation. For example, similar results for the formation of the pseudogap in the single-particle characteristics of the two-dimensional Hubbard model were obtained in the cluster generalizations of DMFT [32, 33]. However, these methods exhibit specific limitations (e.g. on cluster size) and are still not widely used to calculate the two-particle properties, such as the general response functions, notably, the optical conductivity. The DMFT + Σ approach has obvious advantages here, associated with saving computational resources: it requires a significantly lower cost of computational time, and its advantage in calculating the two-particle response functions is quite obvious. This opens up additional opportunities for the systematic comparison of various types of nonlocal fluctuations or additional interactions and their influence on the electronic properties of strongly correlated systems, providing an intuitively clear path to the analysis of experimental and theoretical results obtained via more complicated methods.

The rather simple generalization of our computational scheme enabled us also to formulate the generalized LDA + DMFT + Σ approach allowing us to perform calcula-

tions of all the effects discussed above for real compounds of transition metal elements with strong electronic correlations. One can expect that these calculations will be useful in analyzing and explaining new experimental findings.

Acknowledgments. The authors thank Th Pruschke for his significant contribution to the development of the DMFT + Σ approach in its initial stages, as well as for providing us with the very efficient NRG code that was used in most computations. We are also grateful to S V Borisenko and other members of the Dresden ARPES group with whom ARPES studies of PCCO were performed. Studies of Sr(Ca)VO₃, LSCO, and NCCO compounds were performed in the framework of a joint project with Osaka University (group led by Prof. S Suga and Prof. A Sekiyama).

This work was partially supported by RFBR grant No. 11-02-00147 and performed within the framework of the Programs ‘Quantum Physics of Condensed Matter’ (UB RAS 09-P-2-1009) of the Presidium of RAS, and ‘Strongly Correlated Electrons in Solids’ of the Physical Sciences Division of RAS (UB RAS 09-T-2-1011).

References

1. Mott N F *Metal-Insulator Transitions* 2nd ed. (London: Taylor & Francis, 1990) [Translated into Russian (Moscow: Nauka, 1979)]
2. Izyumov Yu A, Anisimov V I *Elektronnaya Struktura Soedinenii s Sil'nymi Korrelyatsiyami* (Electronic Structure of Strongly Correlated Materials) (Moscow–Izhevsk: RKhD, 2008) [Translated into English: Anisimov V, Izyumov Yu *Electronic Structure of Strongly Correlated Materials* (Heidelberg: Springer, 2010)]
3. Vollhardt D, in *Correlated Electron Systems* (Ed. V J Emery) (Singapore: World Scientific, 1993) p. 57
4. Pruschke Th, Jarrell M, Freericks J K *Adv. Phys.* **44** 187 (1995)
5. Georges A et al. *Rev. Mod. Phys.* **68** 13 (1996)
6. Vollhardt D *AIP Conf. Proc.* **1297** 339 (2010)
7. Kotliar G, Vollhardt D *Phys. Today* **57** (3) 53 (2004)
8. Hubbard J *Proc. R. Soc. London A* **276** 238 (1963)
9. Hubbard J *Proc. R. Soc. London A* **277** 237 (1964)
10. Hubbard J *Proc. R. Soc. London A* **281** 401 (1964)
11. Hubbard J *Proc. R. Soc. London A* **285** 542 (1965)
12. Hubbard J *Proc. R. Soc. London A* **296** 82 (1967)
13. Hubbard J *Proc. R. Soc. London A* **296** 100 (1967)
14. Metzner W, Vollhardt D *Phys. Rev. Lett.* **62** 324 (1989)
15. Anderson P W *Phys. Rev.* **124** 41 (1961)
16. Pruschke Th, Grewe N *Z. Phys. B* **74** 439 (1989)
17. Pruschke Th, Cox D L, Jarrell M *Phys. Rev. B* **47** 3553 (1993)
18. Hirsch J E, Fye R M *Phys. Rev. Lett.* **56** 2521 (1986)
19. Jarrell M *Phys. Rev. Lett.* **69** 168 (1992)
20. Rozenberg M J, Zhang X Y, Kotliar G *Phys. Rev. Lett.* **69** 1236 (1992)
21. Georges A, Krauth W *Phys. Rev. Lett.* **69** 1240 (1992)
22. Jarrell M, in *Numerical Methods for Lattice Quantum Many-Body Problems* (Ed. D J Scalapino) (Reading, Mass.: Addison-Wesley, 1997)
23. Wilson K G *Rev. Mod. Phys.* **47** 773 (1975)
24. Bulla R, Costi T A, Pruschke Th *Rev. Mod. Phys.* **80** 395 (2008)
25. Anisimov V I et al. *J. Phys. Condens. Matter* **9** 7359 (1997)
26. Lichtenstein A I, Katsnelson M I *Phys. Rev. B* **57** 6884 (1998)
27. Nekrasov I A et al. *Eur. Phys. J. B* **18** 55 (2000)
28. Held K et al. *Ψ_k Newsletter* (56) 65 (2003)
29. Held K et al. *Int. J. Mod. Phys. B* **15** 2611 (2001)
30. Held K et al., in *Quantum Simulations of Complex Many-Body Systems: From Theory to Algorithms* (Eds J Grotendorst, D Marx, A Muramatsu) (Julich: John von Neumann Institute for Computing, 2002) p. 175
31. Lichtenstein A I, Katsnelson M I, Kotliar G, in *Electron Correlations and Materials Properties 2* Vol. 2 (Eds A Gonis, N Kioussis, M Cifan) (New York: Kluwer Acad./Plenum Publ., 2003) p. 428
32. Maier Th et al. *Rev. Mod. Phys.* **77** 1027 (2005)

33. Kotliar G et al. *Phys. Rev. Lett.* **87** 186401 (2001)
34. Capone M et al. *Phys. Rev. B* **69** 195105 (2004)
35. Sadovskii M V et al. *Phys. Rev. B* **72** 155105 (2005)
36. Kuchinskii E Z, Nekrasov I A, Sadovskii M V *Pis'ma Zh. Eksp. Teor. Fiz.* **82** 217 (2005) [*JETP Lett.* **82** 198 (2005)]
37. Kuchinskii E Z, Nekrasov I A, Sadovskii M V *Fiz. Nizkikh Temp.* **32** 528 (2006) [*Low Temp. Phys.* **32** 398 (2006)]
38. Kuchinskii E Z, Nekrasov I A, Sadovskii M V *Phys. Rev. B* **75** 115102 (2007)
39. Kuchinskii E Z, Nekrasov I A, Sadovskii M V *Zh. Eksp. Teor. Fiz.* **133** 670 (2008) [*JETP* **106** 581 (2008)]
40. Vollhardt D, Wölfle P *Phys. Rev. B* **22** 4666 (1980)
41. Vollhardt D, Wölfle P *Phys. Rev. Lett.* **48** 699 (1982)
42. Sadovskii M V *Diagrammatika* (Diagrammatics) 2nd ed. (Moscow – Izhevsk: Inst. Komp'yut. Issled., 2010); *Diagrammatics* (Singapore: World Scientific, 2006)
43. Kotliar G et al. *Phys. Rev. Lett.* **87** 186401 (2001)
44. Biroli G, Kotliar G *Phys. Rev. B* **65** 155112 (2002)
45. Lichtenstein A I, Katsnelson M I *Phys. Rev. B* **62** R9283 (2000)
46. Hettler M H et al. *Phys. Rev. B* **58** R7475 (1998)
47. Hettler M H et al. *Phys. Rev. B* **61** 12739 (2000)
48. Maier Th et al. *Phys. Rev. Lett.* **85** 1524 (2000)
49. Maier Th et al. *Eur. Phys. J. B* **13** 613 (2000)
50. Huscroft C et al. *Phys. Rev. Lett.* **86** 139 (2001)
51. Kusunose H *J. Phys. Soc. Jpn.* **75** 054713 (2006)
52. Toschi A, Katanin A A, Held K *Phys. Rev. B* **75** 045118 (2007)
53. Rubtsov A N, Katsnelson M I, Lichtenstein A I *Phys. Rev. B* **77** 033101 (2008)
54. Rubtsov A N, Katsnelson M I, Lichtenstein A I, Georges A *Phys. Rev. B* **79** 045133 (2009)
55. Timusk T, Statt B *Rep. Prog. Phys.* **62** 61 (1999)
56. Sadovskii M V *Usp. Fiz. Nauk* **171** 539 (2001) [*Phys. Usp.* **44** 515 (2001)]
57. Pines D, cond-mat/0404151
58. Schmalian J, Pines D, Stojković B *Phys. Rev. Lett.* **80** 3839 (1998)
59. Schmalian J, Pines D, Stojković B *Phys. Rev. B* **60** 667 (1999)
60. Kuchinskii E Z, Sadovskii M V *Zh. Eksp. Teor. Fiz.* **115** 1765 (1999) [*JETP* **88** 968 (1999)]
61. Sadovskii M V *Zh. Eksp. Teor. Fiz.* **77** 2070 (1979) [*Sov. Phys. JETP* **50** 989 (1979)]
62. Sadovskii M V *Zh. Eksp. Teor. Fiz.* **66** 1720 (1974) [*Sov. Phys. JETP* **39** 845 (1974)]
63. Sadovskii M V, Timofeev A A *J. Moscow Phys. Soc.* **1** 391 (1991)
64. Sadovskii M V, Strigina N A *Zh. Eksp. Teor. Fiz.* **122** 610 (2002) [*JETP* **95** 526 (2002)]
65. Vilk Y M, Tremblay A-M S *J. Physique I* **7** 1309 (1997)
66. Ding H et al. *Nature* **382** 51 (1996)
67. Kuchinskii E Z, Sadovskii M V *Zh. Eksp. Teor. Fiz.* **130** 477 (2006) [*JETP* **103** 415 (2006)]
68. Armitage N P et al. *Phys. Rev. Lett.* **87** 147003 (2001)
69. Basov D N, Timusk T *Rev. Mod. Phys.* **77** 721 (2005)
70. Hwang J, Timusk T, Gu G D *J. Phys. Condens. Matter* **19** 125208 (2007)
71. Lee P A, Ramakrishnan T V *Rev. Mod. Phys.* **57** 287 (1985)
72. Belitz D, Kirkpatrick T R *Rev. Mod. Phys.* **66** 261 (1994)
73. Mott N F *Proc. Phys. Soc. A* **62** 416 (1949)
74. Anderson P W *Phys. Rev.* **109** 1492 (1958)
75. Finkel'shtein A M *Zh. Eksp. Teor. Fiz.* **84** 168 (1983) [*Sov. Phys. JETP* **57** 97 (1983)]
76. Castellani C P et al. *Phys. Rev. B* **30** 527 (1984)
77. Dobrosavljević V, Kotliar G *Phys. Rev. Lett.* **78** 3943 (1997)
78. Dobrosavljević V, Pastor A A, Nikolić B K *Europhys. Lett.* **62** 76 (2003)
79. Byczuk K, Hofstetter W, Vollhardt D *Phys. Rev. Lett.* **94** 056404 (2005)
80. Henseler P, Kroha J, Shapiro B *Phys. Rev. B* **77** 075101 (2008)
81. Henseler P, Kroha J, Shapiro B *Phys. Rev. B* **78** 235116 (2008)
82. Pezzoli M E, Becca F *Phys. Rev. B* **81** 075106 (2010)
83. Ulmke M, Janiš V, Vollhardt D *Phys. Rev. B* **51** 10411 (1995)
84. Vlaming R, Vollhardt D *Phys. Rev. B* **45** 4637 (1992)
85. Wölfle P, Vollhardt D, in *Anderson Localization* (Springer Series in Solid State Sciences, Vol. 39, Eds Y Nagaoka, H Fukuyama) (Berlin: Springer, 1982) p. 26
86. Sadovskii M V, in *Soviet Scientific Reviews – Physics Reviews* Vol. 7 (Ed I M Khalatnikov) (New York: Harwood Acad. Publ., 1986) p. 1
87. Wölfle P, Vollhardt D, in *Electronic Phase Transitions* (Modern Problems in Condensed Matter Sciences, Vol. 32, Eds W Hanke, Yu V Kopaev) (Amsterdam: North-Holland, 1992) p. 1
88. Kuchinskii E Z et al. *Zh. Eksp. Teor. Fiz.* **107** 2027 (1995) [*JETP* **80** 1122 (1995)]
89. Kuchinskii E Z, Érkabaev M A *Fiz. Tverd. Tela* **39** 412 (1997) [*Phys. Solid State* **39** 357 (1997)]
90. Kuchinskii E Z et al. *Zh. Eksp. Teor. Fiz.* **137** 368 (2010) [*JETP* **110** 325 (2010)]
91. Bulla R *Phys. Rev. Lett.* **83** 136 (1999)
92. Bulla R, Costi T A, Vollhardt D *Phys. Rev. B* **64** 045103 (2001)
93. Blümler N “Mott – Hubbard metal – insulator transition and optical conductivity”, Thesis (München: Univ. Augsburg, 2002)
94. Erkaev M A, Sadovskii M V *J. Moscow Phys. Soc.* **2** 233 (1992)
95. Abrahams E et al. *Phys. Rev. Lett.* **42** 673 (1979)
96. Altshuler B L, Aronov A G, Lee P A *Phys. Rev. Lett.* **44** 1288 (1980)
97. Dolan G J, Osheroff D D *Phys. Rev. Lett.* **43** 721 (1979)
98. Bishop D J, Tsui D C, Dynes R C *Phys. Rev. Lett.* **44** 1153 (1980)
99. Uren M J, Davies R A, Pepper M J *Phys. C* **13** L985 (1980)
100. Kravchenko S V, Sarachik M P *Rep. Prog. Phys.* **67** 1 (2004)
101. Abrahams E, Kravchenko S V, Sarachik M P *Rev. Mod. Phys.* **73** 251 (2001)
102. Valla T et al. *Phys. Rev. Lett.* **83** 2085 (1999)
103. Hengsberger M et al. *Phys. Rev. Lett.* **83** 592 (1999)
104. Lanzara A et al. *Nature* **412** 510 (2001)
105. Shen Z-X et al. *Philos. Mag. B* **82** 1349 (2002)
106. Rotenberg E, Schaefer J, Kevan S D *Phys. Rev. Lett.* **84** 2925 (2000)
107. Higashiguchi M et al. *J. Electron Spectrosc. Relat. Phenom.* **144–147** 639 (2005)
108. Sun Z et al. *Phys. Rev. Lett.* **97** 056401 (2006)
109. He H et al. *Phys. Rev. Lett.* **86** 1610 (2001)
110. Hwang J, Timusk T, Gu G D *Nature* **427** 714 (2004)
111. Ronning F et al. *Phys. Rev. B* **67** 165101 (2003)
112. Yoshida T et al. *Phys. Rev. Lett.* **95** 146404 (2005)
113. Graf J et al. *Phys. Rev. Lett.* **98** 067004 (2007)
114. Byczuk K et al. *Nature Phys.* **3** 168 (2007)
115. Abrikosov A A, Gorkov L P, Dzyaloshinski I E *Metody Kvantovoi Teorii Polya v Statisticheskoi Fizike* (Methods of Quantum Field Theory in Statistical Physics) (Moscow: Fizmatgiz, 1963) [Translation into English (New York: Dover Publ., 1975)]
116. Nekrasov I A et al. *Phys. Rev. B* **73** 155112 (2006)
117. Toshi A et al. *Phys. Rev. Lett.* **102** 076402 (2009)
118. Bulla R, Pruschke Th, Hewson A C *Physica B* **259–261** 721 (1999)
119. Holstein T *Ann. Physics* **8** 325 (1959)
120. Hewson A C, Mayer D J *Phys. Condens. Matter* **17** 5413 (2002)
121. Koller W, Hewson A C, Edwards D M *Phys. Rev. Lett.* **95** 256401 (2006)
122. Hague J P J *Phys. Condens. Matter* **15** 2535 (2003)
123. Migdal A B *Zh. Eksp. Teor. Fiz.* **34** 1438 (1958) [*Sov. Phys. JETP* **7** 999 (1958)]
124. Kuchinskii E Z, Nekrasov I A, Sadovskii M V *Phys. Rev. B* **80** 115124 (2009)
125. Sadovskii M V, Kuchinskii E Z, Nekrasov I A *J. Phys. Chem. Solids* **72** 366 (2011)
126. Koller W, Meyer D, Hewson A C *Phys. Rev. B* **70** 155103 (2004)
127. Jeon G S et al. *Phys. Rev. B* **70** 125114 (2004)
128. Koller W et al. *Europhys. Lett.* **66** 559 (2004)
129. Born M, Oppenheimer R *Ann. Physik* **389** 457 (1927)
130. Hohenberg P, Kohn W *Phys. Rev.* **136** B864 (1964)
131. Jones R O, Gunnarsson O *Rev. Mod. Phys.* **61** 689 (1989)
132. Kohn W, Sham L J *Phys. Rev.* **140** A1133 (1965)
133. Sham L J, Kohn W *Phys. Rev.* **145** 561 (1966)
134. Janak J F *Phys. Rev. B* **18** 7165 (1978)
135. Ceperley D M, Alder B J *Phys. Rev. Lett.* **45** 566 (1980)
136. Andersen O K *Phys. Rev. B* **12** 3060 (1975)
137. Andersen O K, Jepsen O *Phys. Rev. Lett.* **53** 2571 (1984)
138. Müller-Hartmann E Z *Phys. B* **74** 507 (1989)
139. Müller-Hartmann E Z *Phys. B* **76** 211 (1989)
140. Wahle J et al. *Phys. Rev. B* **58** 12749 (1998)
141. Held K *Adv. Phys.* **56** 829 (2007)
142. Karolak M et al. *J. Electron Spectrosc. Relat. Phenom.* **181** 11 (2010)

143. Zöfl M B et al. *Phys. Rev. B* **61** 12810 (2000)
144. Gunnarsson O et al. *Phys. Rev. B* **39** 1708 (1989)
145. Aryasetiawan F et al. *Phys. Rev. B* **70** 195104 (2004)
146. Miyake T, Aryasetiawan F *Phys. Rev. B* **77** 085122 (2008)
147. Lambin Ph, Vigneron J P *Phys. Rev. B* **29** 3430 (1984)
148. Andersen O K, Saha-Dasgupta T *Phys. Rev. B* **62** R16219 (2000)
149. Andersen O K et al. Ψ_k *Newsletter* (45) 86 (2001)
150. Andersen O K, Saha-Dasgupta T, Ezhov S *Bull. Mater. Sci.* **26** 19 (2003)
151. Anisimov V I et al. *Phys. Rev. B* **71** 125119 (2005)
152. Fujimori A et al. *Phys. Rev. Lett.* **69** 1796 (1992)
153. Aiura Y et al. *Phys. Rev. B* **47** 6732 (1993)
154. Inoue I H et al. *Phys. Rev. Lett.* **74** 2539 (1995)
155. Inoue I H et al. *Phys. Rev. B* **58** 4372 (1998)
156. Morikawa K et al. *Phys. Rev. B* **52** 13711 (1995)
157. Maiti K et al. *Europhys. Lett.* **55** 246 (2001)
158. Sekiyama A et al. *Phys. Rev. Lett.* **93** 156402 (2004)
159. Inoue I H et al. *Physica C* **235–240** 1007 (1994)
160. Rozenberg M J et al. *Phys. Rev. Lett.* **76** 4781 (1996)
161. Solovyev I, Hamada N, Terakura K *Phys. Rev. B* **53** 7158 (1996)
162. Makino H et al. *Phys. Rev. B* **58** 4384 (1998)
163. Jarrell M, Gubernatis J E *Phys. Rep.* **269** 133 (1996)
164. Krause M O, Oliver J H J. *Phys. Chem. Ref. Data* **8** 329 (1979)
165. Inoue I H et al. *Phys. Rev. Lett.* **88** 236403 (2002)
166. Pavarini E et al. *Phys. Rev. Lett.* **92** 176403 (2004)
167. Pavarini E et al. *New J. Phys.* **7** 188 (2005)
168. Yoshida T et al. *Phys. Rev. Lett.* **95** 146404 (2005)
169. Sadovskii M V, in *Strings, Branes, Lattices, Networks, Pseudogaps and Dust* (Moscow: Scientific World, 2007) p. 357 [Translated into English, cond-mat/0408489]
170. Damascelli A, Hussain Z, Shen Z-X *Rev. Mod. Phys.* **75** 473 (2003)
171. Campuzano J C, Norman M R, Randeria M, in *Physics of Superconductors* Vol. 2 (Eds K H Bennemann, J B Ketterson) (Berlin: Springer, 2004) p. 167
172. Fink J et al. *Lecture Notes Phys.* **715** 295 (2007)
173. Zhou X J et al., in *Handbook of High-Temperature Superconductivity: Theory and Experiment* (Ed. J R Schrieffer) (Berlin: Springer, 2007) p. 87
174. Kuchinskii E Z et al. *Zh. Eksp. Teor. Fiz.* **131** 908 (2007) [*JETP* **104** 792 (2007)]
175. Nekrasov I A et al. *Zh. Eksp. Teor. Fiz.* **137** 1133 (2010) [*JETP* **110** 989 (2010)]
176. Nekrasov I A et al. *J. Phys. Chem. Solids* **69** 3269 (2008)
177. Kokorina E E et al. *Zh. Eksp. Teor. Fiz.* **134** 968 (2008) [*JETP* **107** 828 (2008)]
178. Nekrasov I A et al. *Phys. Rev. B* **80** 140510(R) (2009)
179. Nekrasov I A, Kuchinskii E Z, Sadovskii M V *J. Phys. Chem. Solids* **72** 371 (2011)
180. Hedin L, Lundqvist B I *J. Phys. C* **4** 2064 (1971)
181. von Barth U, Hedin L *J. Phys. C* **5** 1629 (1972)
182. Andersen O K et al. *J. Phys. Chem. Solids* **56** 1573 (1995)
183. Zobjkalo I A et al. *Solid State Commun.* **80** 921 (1991)
184. Motoyama E M et al. *Nature* **445** 186 (2007)
185. Hücker M et al. *Phys. Rev. B* **71** 094510 (2005)
186. Armitage N P et al. *Phys. Rev. Lett.* **88** 257001 (2002)
187. Kaminski A et al. *Phys. Rev. B* **71** 014517 (2005)
188. Borisenko S V et al. *Phys. Rev. Lett.* **84** 4453 (2000)
189. Onose Y et al. *Phys. Rev. Lett.* **87** 217001 (2001)
190. Quijada M A et al. *Phys. Rev. B* **60** 14917 (1999)